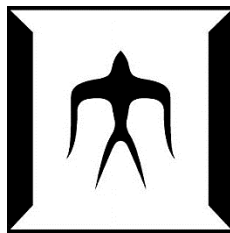


Study on the Influence of the Inlet Swirling Flow in a Double and Triple Elbow Using Phased Array UVP



Doctoral Dissertation by:

San Shwin

for the degree of

Doctor of Engineering

Academic advisor: Assoc. Prof. Hiroshige KIKURA

Department of Nuclear Engineering, Graduate School of Science and Engineering

Tokyo Institute of Technology

December 2018

Abstract

This study presents investigation of flow structure and velocity fluctuation downstream of a compact pipe layout, which make with double and triple elbow. Ultrasonic Velocity Profiler (UVP), Phased Array UVP and PIV systems are used to measure the velocity field downstream of the elbow. The velocity profiles from the experiments were imposed in CFD numerical simulation to visualize the complete flow structure through the pipe. CFD code ANSYS Fluent 16.2 is used for the numerical simulation. In CFD simulation, the turbulent RNG k - ϵ model is adopted to visualize asymmetric turbulent flow downstream of the double bent pipe. The main objective is to understand the fluid flow structure in a compact piping system. In addition, our laboratory is using Ultrasonic Doppler method for the non-destructive measurement. The aim is to improve the performance of the measurement system and to apply in the flow measurement and flow visualization system in the power plant.

In the experiment condition, the water flows at Reynolds number $Re = 1 \times 10^4$ and the water temperature is in the room temperature 25°C . In case of inlet swirling flow condition, a rotary type swirling generator was used to generate homogenous swirling flow, and the swirl number was set up $S = 1$. Phased Array UVP is applied for the flow visualization downstream of the double and triple elbow in the condition of swirling inlet flow and without inlet swirling flow. Phased Array UVP can provide a two-dimensional velocity vector of the fluid. The measurement positions are located at $x/D = 0$, $x/D = 0.6$, $x/D = 1$ and $x/D = 1.5$ downstream of elbow. In two-dimensional velocity of without inlet swirling flow, the flow separation occurs at the edge of inner elbow, and the reattachment point is located at $x/D = 1.5$. Therefore, the reverse flow region is narrow in swirling inlet condition. In the condition of without inlet swirling flow, the axial velocity fluctuation is higher than with inlet swirling flow, but radial velocity fluctuation is lower than inlet swirling flow.

Contents

Nomenclature	iv
List of Figures	vii
List of Tables.....	x
1. Introduction.....	1
1.1 Background	3
1.2 Swirling flow in a compact pipe layout.....	5
1.3 Review of Previous Study	6
1.4 Thesis Objective and Outline	9
References	13
2. Numerical Investigation of Turbulent Flow in a Single Elbow Using Inlet Velocity Profile	19
2.1 Introduction	21
2.2 One-dimensional velocity profile measurement.....	24
2.2.1 Ultrasonic Velocity Profiler (UVP-Duo).....	25
2.2.2 Velocity Profile Measurement in a Straight Pipe Using UVP-Duo	26
2.2.3 Experimental apparatus.....	27
2.3 Numerical Simulation Approach	28
2.3.1 Basic Theory.....	28
2.3.2 Mesh Characteristics	29
2.3.3 Turbulent Model and Wall Functions	29
2.3.4 Boundary Conditions	31
2.3.5 Pressure-Base Solver Setting.....	32
2.4 Results and discussion.....	34
2.4.1 One-dimensional velocity profile measurement results	34
2.4.2 Numerical simulation results.....	34

2.5	Conclusions	35
	References.....	37
3.	Turbulent Flow Measurement Downstream of Double Elbow Using Phased Array UVP and PIV.....	51
3.1	Introduction.....	53
3.2	Two-dimensional Velocity by Phased Array UVP	54
3.3	Near-field effect by Phased Array sensor	59
3.4	Experimental setup.....	60
3.5	PIV measurement setup	60
3.5	Results and discussions	61
3.6	Conclusions.....	63
	References.....	64
4.	Influence of Inlet Swirling Flow on Flow Structure and Velocity Fluctuation.....	75
4.1	Introduction.....	77
4.2	Experimental setup.....	80
4.2.1	The Swirling Generator	81
4.2.2	Experimental Procedures.....	82
4.3	Results and discussion.....	83
4.3.1	One-dimensional velocity analysis	83
4.3.2	Two-dimensional velocity with and without inlet swirling flow	85
4.3.3	Comparison of Velocity Fluctuation with and without Inlet swirling flow	86
4.4	Conclusions.....	87
	References.....	88
5.	Experimental and Numerical Investigation of Swirling flow Downstream of Triple Elbow Pipe Layout	103
5.1	Introduction	105
5.2	Experimental Apparatus and Measurement Procedures	106

5.3 Numerical Simulation Approach	108
5.4 Experimental results and discussion.....	108
5.4.1 One-dimensional velocity profiles	108
5.4.2 Two-dimensional velocity fields	109
5.5 Numerical results and discussion.....	110
5.5.1 Two-dimensional velocity fields	110
5.6 Conclusions	111
References	112
6. Conclusions	123
List of Publications	129
Acknowledgements.....	131

Nomenclature

Latin characters

<i>a</i>	Single element width	[mm]
<i>A</i>	Surface area	[m ²]
<i>c</i>	Speed of sound	[m/s]
<i>d</i>	Inter element spacing	[mm]
<i>De</i>	Dean number	[-]
<i>D</i>	Diameter	[m]
<i>f</i>	Basic frequency of phased array sensor	[Hz]
<i>k</i>	Correction factor	[-]
<i>l</i>	piezoelectric element length	[mm]
<i>L</i>	Near-field length	[mm]
<i>m</i>	Mass	[kg]
<i>ṁ</i>	Mass flow rate	[kg/s]
<i>n</i>	Number of cycle	[-]
<i>p</i>	Pressure	[Pa]
<i>Q</i>	Volumetric flow rate	[m ³ /s]
<i>Re</i>	Reynolds number	[-]
<i>r</i>	Radius	[m]
<i>S</i>	Swirling intensity	[Hz]
<i>T</i>	Temperature	[K] or [°C]
<i>t</i>	Time	[s]
<i>U</i>	Axial mean velocity	[m/s]
<i>V</i>	Particle velocity	[m/s]
<i>w</i>	piezoelectric element width	[mm]
<i>x</i>	Axial coordinate	[m]

Greek characters

∞	Angles between the transmitter and receiver	[degree]
β	Angles between the transmitter and receiver	[degree]
δ	Angles between the transmitter and receiver	[degree]
θ	Phased steering angles	[degree]
k	Turbulent Kinetic Energy	[m ² /s ²]
ε	Turbulent Dissipation Rate	[m ² /s ³]
μ	Dynamic viscosity	[kg/ms]
ν	Fluid kinematic viscosity	[m ² /s]
γ	Curvature ratio of elbow	[-]
ρ	Density	[kg/m ³]
Δt	Time delay of ultrasound pulse	[s]

Subscripts

0	Basic frequency of ultrasonic sensor (f_0)
c	Curvature radius
ch	Channel number
oscillation	Near field oscillation
di	Doppler shift frequency
max	Maximum
min	Minimum
p	Particle
rms	Root mean square
s	Steering

Abbreviations

CFD	Computational Fluid Dynamics
LDV	Laser Doppler Velocimetry
PIV	Particle Image Velocimetry
UVP	Ultrasonic Velocity Profiler

List of Figures

Figure 1.1. Failure in a high-pressure extraction line at Fort Calhoun (USA) in 1997...	15
Figure 1.2. Rupture at an 8-inch elbow of a moisture separator reheater of Millstone Unit 2 (USA) in 1997.....	15
Figure 1.3. An 18-inch elbow in a condensate line ruptured catastrophically (USA) in 1986.....	16
Figure 1.4. Schematic view of Japan Sodium-cooled Fast Reactor (JSFR).....	16
Figure 1.5. Schematic view of triple elbow pipe layout by Mizutani <i>et al.</i>	17
Figure 1.6. Tangential injection method swirling generator by Mizutani <i>et al.</i>	17
Figure 2.1. The principle of one-dimensional velocity profile measurement.....	40
Figure 2.2. Hard-ware system of UVP-Duo.....	40
Figure 2.3. Single element ultrasound transducer.....	41
Figure 2.4. Schematic view of straight pipe flow measurement set up.....	41
Figure 2.5. Picture of straight pipe flow measurement set up.....	42
Figure 2.6. Velocity Profiles at 10D using UVP-Duo.....	42
Figure 2.7. Velocity Profiles at 18D using UVP-Duo.....	43
Figure 2.8. Velocity Profiles at 24D using UVP-Duo.....	43
Figure 2.9. Velocity Profiles at 30D using UVP-Duo.....	44
Figure 2.10. Velocity Profiles in the developed region at Re 30000.....	44
Figure 2.11. Geometry of a simulated single elbow.....	45
Figure 2.12. Mesh quality of the cross-sectional plane.....	45
Figure 2.13. Turbulent Kinetic Energy and Velocity Contour at Re 10,000.....	46
Figure 2.14. Turbulent Kinetic Energy and Velocity Contour at Re 20,000.....	46
Figure 2.15. Turbulent Kinetic Energy and Velocity Contour at Re 30,000.....	46
Figure 2.16. Axial velocity field downstream of a single elbow.....	47
Figure 2.17. Tangential velocity field downstream of a single elbow in cross-section plane at $x/D = 0$	48
Figure 2.18. Tangential velocity field downstream of a single elbow in cross-section plane at $x/D = 0.5$	48

Figure 2.19. Tangential velocity field downstream of a single elbow in cross-section plane at $x/D = 1$	49
Figure 2.20. Figure 2.20. Tangential velocity field downstream of a single elbow in cross-section plane at $x/D = 1.5$	49
Figure 3.1. Beam steering principle of Phased Array sensor and its schematic diagram.....	66
Figure 3.2. A two-transducer ultrasound system produces a Doppler signal from velocity vector V	66
Figure 3.3. Velocity vector reconstruction.....	67
Figure 3.4. Phased array UVP measurement system.....	67
Figure 3.5. Near-field length of sound pressure.....	68
Figure 3.6. Correction factor of the rectangular sensor.....	68
Figure 3.7. Experimental facilities of a piping system.....	69
Figure 3.8. Detail view of measurement position.....	69
Figure 3.8. Detail view of measurement position.....	70
Figure 3.10. Detail view of PIV test section.....	70
Figure 3.11 Top view picture of the test section.....	71
Figure 3.12 Side view picture of the test section.	71
Figure 3.13 Average velocity vector from PIV measurement.	72
Figure 3.14 Average velocity vector from Phased Array UVP measurement.....	72
Figure 3.15 Phased Array UVP and PIV measurement results in two-dimensional vector.....	73
Figure 3.16 Quantative comaparison between Phased Array UVP and PIV.....	73
Figure 3.17 Veloity fluctuation analysis from Phased Array UVP measurement..	74
Figure 4.1 Experimental apparatus of water circulation system.....	91
Figure 4.2 Swirling generator and double bend pipe from top view..	91
Figure 4.3 Picture of test section for one-dimensional measurement (UVP-Duo)..	92
Figure 4.4 Detail view of test section in second elbow (Phased Array UVP).....	92
Figure 4.5 Detail view of measurement positions (UVP-Duo).....	93
Figure 4.6 1D velocity profile in the first elbow for different Reynolds number.....	94
Figure 4.7 1D velocity profile in the first elbow for different swirl number.....	94

Figure 4.8 1D velocity profile in the second elbow for different Reynolds number...	95
Figure 4.9 1D velocity profile in the second elbow for different swirl number.....	95
Figure 4.10 Time-average axial velocity without inlet swirling flow ($S=0$)..	96
Figure 4.11 Time-average tangential velocity without inlet swirling flow ($S=0$).....	96
Figure 4.12 Time-average axial velocity without inlet swirling flow ($S=1$)..	97
Figure 4.13 Time-average tangential velocity without inlet swirling flow ($S=1$)..	97
Figure 4.14 Two-dimensional time average axial velocity without inlet swirling flow ($S = 0$)..	98
Figure 4.15 Two-dimensional time average tangential velocity with the inlet swirling flow ($S = 1$).....	98
Figure 4.16 Two-dimensional time average axial velocity with the inlet swirling flow ($S = 1$)..	99
Figure 4.17 Two-dimensional time average radial velocity without inlet swirling flow ($S = 0.0$) at $x/D = 1$	99
Figure 4.18 Two-dimensional time average radial velocity with the inlet swirling flow ($S = 0.25$) at $x/D = 1$	100
Figure 4.19 Two-dimensional time average radial velocity without inlet swirling flow ($S = 0.5$) at $x/D = 1$	100
Figure 4.20 Two-dimensional time average radial velocity without inlet swirling flow ($S = 0.75$) at $x/D = 1$	101
Figure 4.21 Comparison of the axial velocity fluctuation between with and without inlet swirling..	101
Figure 4.22 Comparison of the radial velocity fluctuation between with and without inlet swirling.....	102
Figure 5.1 Experimental facilities of a piping system.....	113
Figure 5.2 Detail view of the rotary swiler and pipe layout.....	113
Figure 5.3 Test section downstream of the third elbow.....	114
Figure 5.4 Test section in the third elbow for 1D velocity measurement.....	114
Figure 5.5 Detail view of test section for 1D velocity measurement.....	114
Figure 5.6 Simulation pipe geometry same as pipe layout with experement..	115
Figure 5.7 Detail view of polyhedral mesh quality.....	115

Figure 5.8 1D velocity profile in third elbow for different Reynolds number.....	116
Figure 5.9 1D velocity profile in third elbow for different Swirl number.....	116
Figure 5.10 Inlet swirling flow condition with axial velocitie.....	117
Figure 5.11 Inlet swirling flow condition with radial velocitie.....	117
Figure 5.12 Inlet swirling flow condition with tangential velocitie.....	117
Figure 5.13 Two-dimensional time average axial velocity from experiment.....	118
Figure 5.14 Two-dimensional time average axial velocity from simulation.....	118
Figure 5.15 Cross sectional velocity distribution for 10 mm position.....	119
Figure 5.16 Cross sectional velocity distribution for 30mm position.....	119
Figure 5.17 Cross sectional velocity distribution for 50mm position.....	120
Figure 5.18 Cross sectional velocity distribution for 75mm position.....	120

List of Tables

Table 2.1. Experimental parameters of straight pipe flow measurement.....	39
Table 2.2. Error of volumetric measuring method.....	39
Table 3.1. Experimental condition.....	65
Table 3.2. Experimental parameters of Phased Array measurement.....	65
Table 4.1. Experimental conditions for UVP-Duo.....	90
Table 4.2. Experimental parameters of Phased Array UVP parameters.....	90
Table 5.1. Experimental conditions.....	113
Table 5.2. Numerical conditions.....	113

Chapter 1

Introduction

1.1 Background

Natural flows from the motion of the fluids have been the subject of many scientific studies. Scientists succeeded to answer some of the questions regarding their existence and define the parameters, which govern their dynamics. However, one of the subjects from the area of fluid dynamics, which still constitutes a complicated condition.

More than a century ago, Osborne Reynolds started the study of the flow regime to understand the conditions under which fluid flowing through a pipe would be laminar or turbulent. Laminar flow is the smooth streamlines and highly ordered motion. Turbulent is characterized by velocity fluctuations and highly disordered motion [1-1]. The transition from laminar to turbulent flow does not occur suddenly; it occurs over some region in which the flow fluctuates between laminar and turbulent flows before it becomes fully turbulent. Most flows occurred in practice are turbulent and laminar flow occurs when highly viscous fluids such as oils flow in small pipes or narrow passages [1-2].

The transition from laminar to turbulent flow depends on the geometry, surface roughness, flow velocity, surface temperature, and type of fluid. Reynolds discovered that the flow regime depends mainly on the ratio of inertial forces to viscous forces in the fluid. This ratio is called the Reynolds number.

$$Re = \frac{\text{Inertial forces}}{\text{Viscous forces}} = \frac{\bar{U}D}{\nu} = \frac{\rho\bar{U}D}{\mu} \quad (1.1)$$

Where \bar{U} = average flow velocity (m/s), D = diameter of pipe (m), $\nu = \mu/\rho$ fluid kinematic viscosity (m^2/s), μ = coefficient of the fluid (kg/ms), ρ = the fluid density (kg/m^3).

Reynolds number is a dimensionless quantity. Under most practical conditions, the flow in a circular pipe is laminar for $Re \leq 2300$, turbulent for $Re \geq 4000$, and transition in between. In transitional flow, the flow switches between laminar and turbulent randomly. Therefore, there are three flow regimes in a general fluid flow.

In case of fluid flow pattern, there are several flow patterns and it depends on the geometry of the flow system. For example, if we look around us (such as heat exchanger, compact piping system in the industries or the power plant and river banks), almost nothing is straight and the flow phenomenon is complicated. Therefore, most of the systems of any kind comprise of curved sections and the elbows. If a fluid is moving along a straight pipe that after some point becomes curved the bend or connect with the elbow will cause the fluid particles to change their main direction of motion. There will be an adverse pressure gradient generated from the curvature with an increase in pressure, therefore a decrease in velocity close to the convex wall, and the contrary will occur towards the outer side of the pipe.

The centrifugal force induced from the bend will act stronger on the fluid close to the pipe axis than close to the walls, since the higher velocity fluid is near the pipe axis. This gives rise to a secondary motion superposed on the primary flow, with the fluid in the center of the pipe being swept towards the outer side of the bend and the fluid near the pipe wall will return towards the inside of the bend. This secondary motion is expected to appear as a pair of counter-rotating cells, which bear the name of the British scientist Dean (1927) and are widely known today as Dean vortices [1-3]. The existence of the two symmetrical roll-cells but also introduced the parameter that dynamically defines such flows and is named after him, namely the Dean number. Dean number is related with Reynolds number and the curvature ratio of the bent pipe [1-4]. The equation 1.2 shows Dean number which calculated from Reynolds number and the geometry of pipe.

$$De = Re \sqrt{\frac{R}{R_c}} \quad (1.2)$$

Where R is radius of the pipe and R_c is the curvature radius of the bend pipe.

In real life flow situations, when the fluid flows through a bend pipe or an elbow, there is some further complicated flow structure occurs just downstream of the connected elbow. Tunstall & Harvey (1968) found that in a sharp bend a unique vortex pattern exists for $Re = 4 \times 10^4$, consisting of a single vortex dominating the pipe

cross section, switching its rotational direction from clockwise to counterclockwise [1-5]. The fluid velocity fluctuations appear both at short time scales and at longer time scales. It is called vortex swirling flow. Swirling flows are characterised by the fact that the fluid rotates around an axis that is parallel to the main flow direction. Swirling flows may either occur inadvertently and be considered as a disturbance or may be generated on purpose [1-6]. Applications of swirling flows include cyclone separators, swirling spray dryers, swirling furnaces, vortex tubes used for thermal separation, agitators etc. [1-7].

1.2 Swirling flow in a compact pipe layout

Swirling flows are characterized by the fact that the fluid rotates around an axis that is parallel to the main flow direction. Turbulent swirling flow is encountered in many compact piping systems of industries and power plants. The effects of the swirl combined with effects from curved geometries, which are widely met in practice. The curve pipes can be encountered in many piping system of the industries. Under the swirling flow condition, the large pressure fluctuation and the high-velocity fluctuation happen in the elbows, and these are sources of flow-induced vibration (FIV) [1-9]. FIV can cause the corrosion phenomenon of the pipe wall, and the pipe break accident occurs in a piping system of the industries and the power plants. Failure in a high pressure extraction line at Fort Calhoun (USA) in 1997 as shown in **Figure 1.1**. Rupture at an 8-inch elbow of a moisture separator reheater of Power Plant Millstone Unit 2 (USA) is shown in **Figure 1.2**. An 18 inch elbow in a condensate line ruptured catastrophically in 1986 is shown in **Figure 1.3** According to the pipe break accidents in the history, the accident occurs in the compact pipe layout system cause by FIV and corrosion in the elbow. FIV closely relates with flow structure of fluid and velocity fluctuation. Therefore, the characteristic of flow field and velocity fluctuation are significant issues for the pipeline safety. The studies of swirling turbulent flow in bends is not very extensive, compared to swirling turbulent flow in straight pipes [1-

11]. The flow structure and velocity fluctuation analysis of turbulent swirling flow in a compact pipe layout make with double or triple elbows were rare to find in the previous studies.

In this present study, we focus on the influence of turbulent swirling flow on the flow structure and velocity fluctuation in three types of compact pipe layouts. Here, the influence of the swirling flow on the elbow curvature ratio $R_c/D < 1$ has not been done yet in the previous studies. So in this study, the inlet swirling and without inlet swirling conditions were applied on three compact pipe layouts make with a single elbow, double elbows and triple elbow in the curvature ratio $R_c/D = 0.5$. To observe the flow structure, two-dimensional velocity fields measurements were done using ultrasound technique. Axial, radial and tangential velocity profiles were collected from the axial plane and cross-sectional plane measurements respectively. The measured axial, radial and tangential velocity profiles were applied as the inlet profiles for the validation of the numerical simulation. For computational fluid dynamic (CFD) numerical simulation, ANSYS Fluent (Version 16.2) was used to simulate a pipe flow through the pipe layout same as the experimental setup pipe layout. ANSYS Fluent is an effective simulation tool for the fluid flows. From the simulation results, the fully structure of fluid flow were visualized by two-dimensional velocity fields and velocity contours for the axial plane and cross-sectional plane at any positions of pipe layout.

1.3 Review of Previous Study

In the previous studies, CFD simulation using Open FOAM® on 90-degree-bent elbow was performed to characterize the swirling secondary flow in the downstream of a pipe bend [1-12]. A comparative study was performed to select an appropriate turbulence model for the analysis. One of the first studies that provided the flow through a bend by Al-Rafai *et al.* using the $k - \varepsilon$ model [1-13] and compared with experimental results. They performed experiments and numerical calculations

for a turbulent flow at $Re = 3.4 \times 10^4$ in two types of bend curvature ratio $\gamma = 0.07$ and 0.14 . Laser Doppler Velocimetry (LDV) was utilized in the experiment. The main results consisted of mean and root mean square stream wise velocities. The result showed that the secondary flow is stronger in the bend with the higher curvature ratio γ . In addition, Hilgenstock and Ernst [1-14] tested two common models ($k - \varepsilon$ and renormalization group known as RNG) and provided acceptable results. Kalpakli and Örlü [1-15] studied experimental study for the turbulent flow in a bend pipe with imposed swirl. They studied Dean vortices and swirl motion for swirl intensity $S = 0$ to 1.2 at the downstream region of a bend pipe by using Particle Image Velocimetry (PIV) method. Swirling inlet flow condition is also encountered in the cold-leg piping system in a nuclear reactor. Therefore, Yamano *et al.* [1-16] investigated the effect of swirl flow at the inlet on the 90° double bend pipe both experimentally and numerically, to evaluate the flow-induced vibration for primary cooling pipes in the Japan sodium-cooled fast reactor (JSFR). **Figure 1.4** shows schematic view of JSFR. The experiment was done by PIV method with curvature ratio $R_c/D = 1$. They found that the flow separation region was deflected at the downstream from the bend when the inlet condition on the first bend was swirling flow. Later, Mizutani *et al.* [1-17] investigated the influence of inlet condition upstream the triple elbow as shown in **Figure 1.5**. Particle Image Velocimetry (PIV) was used for the velocity flow mapping, and the tangential injection method was used to generate swirling flow on the inlet. **Figure 1.6** shows tangential injection method swirling generator. The triple elbow with curvature ratio $R_c/D = 1$ was used to be close to an actual condition and to accumulate knowledge towards optimization of a prospective piping layout in the conceptual design of Japan Sodium Fast Reactor (JSFR) [1-18]. Chang and Lee [1-19] also investigated the effects of swirl on the secondary flow field along a bend in Reynolds number $Re = 1.0 - 2.5 \times 10^4$. The measurement system of previous studies, LDV and PIV system were applied to investigate fluid velocity and swirling flow structure. However, these systems have some challenges and it is difficult for the

applications in actual plant process. Therefore, a new measurement technique should be developed to evaluate the velocity field and velocity fluctuation.

Y. Takeda introduced the new measurement technique in 1986 [1-20] for the measurement of velocity profile by Ultrasonic Velocity Profiler (UVP). He developed for optically non-transparent liquid flow measurements such as mercury flow. UVP is non-intrusive measurement method, utilizes a pulsed echo-graphic technique of ultrasound, and can measure an instantaneous velocity profile on a measuring line. Wada and Treenuson applied that UVP technique in one-dimensional the flow rate measurement downstream of double bent pipe by using 4 transducers [1-21, 22]. However, the multi-dimensional measurement of velocity profile should be conducted in order to understand the flow characteristic for the complex pipe system.

In the case of two-dimensional velocity profile measurement (flow mapping), Takeda and Kikura (2002) investigated velocity field of the mercury flow using UVP [1-23]. Flow mapping was accomplished by using multiple transducers, which are arranged in different positions and set to multiple angles. On the other hand, this measurement system becomes larger as the number of transducers is increased. To overcome such problems in conventional UVP (multiple sensors and mechanical movement), A. Fukumoto et al., (2013) has developed a phased array sensor, which has multiple ultrasonic elements to conduct two-dimensional velocity field with multiple measurement lines [1-24]. The developed Phased Array Ultrasonic Profiler (Phased Array UVP) was compact and effective to measure two-dimensional velocity field. Therefore, Phased Array UVP was applied in this study to measure turbulent swirling flow.

In the present study, we measured some turbulent swirling flow in a horizontal straight pipe with the swirling generator. Also, we observed the flow separation and reattachment point just downstream of the double bent pipe with and without swirling effect. The observation of reattachment point is significant for the maintenance of the piping system in the industries and the power plants because it can cause the asymmetric pipe wall thinning and the pipe break accident.

1.4 Thesis Objective and Outline

This thesis presents a study on swirling flow structure and velocity fluctuation analysis in a compact pipe layout flow. Ultrasonic Velocity Profiler (UVP) and Phased Array UVP systems were applied to measure one dimensional velocity profile and two-dimensional velocity fields. The primary objective of this study is to investigate swirling flow structure and to analyze velocity fluctuation downstream of a double and triple elbow. The measurement data were imposed as the inlet boundary condition of Computational Fluid Dynamics (CFD) simulation. From the simulation results, the fully structure of fluid flow were visualized by two-dimensional velocity fields and velocity contours for the axial plane and cross-sectional plane. There are two main aspects of investigation taken into consideration, such as:

1. The characteristic of swirling flow structure in the secondary flow region
2. Velocity distribution and fluctuation of axial, radial and tangential velocities

This thesis is arranged into six chapters based on order of the working process, with the descriptions as follows:

- **Chapter 1 Introduction** – The introduction part introduces the research background and the turbulent swirling flow structure in the bend pipe or the elbow are discussed from the viewpoint of the previous studies and the history of pipe break accident in the piping system of the power plant. The primary objectives of this dissertation and the outline of each chapter are written in the introduction part. The developing process of ultrasound technique is describe to provide the information of the measurement system.
- **Chapter 2 Numerical Investigation of Turbulent Flow in a Single Elbow Using Inlet Velocity Profile** – This chapter presents the fluid velocity measurements in a circular straight pipe using UVP system. The fully develop region can be observed for the turbulent flow at several Reynolds number. The velocity profiles from the measurement results are imposed as the inlet boundary condition for a single elbow simulation using CFD Fluent 16.2. The basic flow theory of turbulent flow in a single elbow pipe is mentioned in this chapter.

The fluid flow structure and turbulent kinetic are analyzed base on the different Reynolds number downstream of a single elbow. From this investigation, the appropriate Reynolds number is choice to use in the next chapter of the turbulent flow measurement and inlet swirling flow measurement.

- **Chapter 3 Turbulent Flow Measurement Downstream of Double Elbow Using Phase Array UVP and PIV** - The investigation of two-dimensional velocity fields was presented in the condition of turbulent flow downstream of double bend pipe , which made by 90° double elbow. Particle Image Velocimetry and Phased Array UVP systems are applied to compare the measurement results. The flow distortion and recirculating flow occur in the measurement region downstream of the double elbow. The reverse secondary flow region and the reattachment point is clearly observed from both measurement results. In the velocity fluctuation analysis, the axial velocity fluctuation apparently occurs at the boundary of the main flow and the recirculating flow. The radial velocity fluctuation occurs at the center of the pipe.
- **Chapter 4 Influence of Inlet Swirling Flow on Flow Structure and Velocity Fluctuation** – This chapter observes influence of inlet swirling flow on the flow structure and velocity fluctuation downstream of double bend pipe layout, which made by 90° double elbow with inlet swirling flow and without inlet swirling flow condition. Phased Array UVP measurement done in the case of with and without inlet swirling flow condition. The inlet swirling flow is confirmed by measuring the cross-section plane 7D downstream of the swirling generator in the condition of swirl intensity $S = 1$. The swirling generator generates the homogeneous swirling flow. The experiment results of one-dimensional normalized axial and tangential velocity with their standard deviations in four positions downstream of the double bend pipe with and without inlet swirling flow. According to one-dimensional velocity profiles, the velocity magnitude of inlet swirling flow is much stronger than

without inlet swirling flow in the secondary flow region. These differences are due to the influence of the inlet swirling flow. In two-dimensional velocity of without inlet swirling flow, the flow separation occurs around $x/D = 0.1$, and the reattachment point is located at $x/D = 1.5$. In case of inlet swirling flow, the flow separation phenomenon is same as the condition of without inlet swirling flow, but the reattachment point is located at $x/D = 1$. Therefore, the reverse flow region is narrow. At $x/D = 1.5$, the fluid becomes the accelerated swirling flow. In the condition of without inlet swirling flow, the axial velocity fluctuation is higher than with inlet swirling flow, but tangential velocity fluctuation is lower than inlet swirling flow.

- **Chapter 5 Experimental and Numerical Investigation of Swirling flow Downstream of Triple Elbow** – This chapter presents the experimental investigation and numerical simulation to observe the flow structure and velocity distribution at the inlet swirling flow condition. The axial, radial and tangential velocities of the swirling flow were measured at $7D$ downstream of the swirling generator by using a phased array sensor. The sensor position was turned into the axial and cross-sectional planes to get the axial, radial and tangential velocities. The velocities were utilized for the boundary inlet conditions of the numerical simulation. The inlet swirling flow velocities from the experimental results were utilized to compare with experimental result and validate CFD numerical simulation. We used the axial, radial and tangential velocity profiles of swirling flow as the inlet boundary conditions and the geometry of the pipe layout was same as the experimental setup. In addition, Phased Array UVP system is applied to measure two-dimensional velocity field downstream of the triple elbow and can confirm the flow separation and reattachment point. The numerical simulation result show that the swirling flow structure is quite similar with the experimental result. Therefore, the validation of the CFD simulation is acceptable. In case of cross-sectional plane visualization, two counter rotation vortex cells were observed at $x/D = 0.2$ and $x/D = 0.6$ positions. When the high velocity axial flow reached the outside wall,

this flow was changed from outside to lateral side of pipe wall in clockwise and counterclockwise directions. In addition, the axial velocity distribution is too different between the intrados and extrados of pipe.

- **Chapter 6 Conclusions** – This chapter summarizes the conclusions obtained from this study.

References

- [1-1] Barkley, Dwight.:Theoretical perspective on the route to turbulence in a pipe. *Journal of Fluid Mechanics* (2016) 803: P1.
- [1-2] Cengel Yunus A.:Fluid Mechanics, fundamentals and applications. 1st editioin (2006).
- [1-3] Dean, W. R.:Note on the motion of fluid in a curved pipe.(1927) *Phil.Mag.* 4, 208–223.
- [1-4] Berger, S. A. & Talbot, L. :Flow in curved pipes. *Annu. Rev. Fluid Mech.* (1983) 15, 461–512.
- [1-5] Tunstall, M. J. & Harvey, J. K.:On the effect of a sharp bend in a fully developed turbulent pipe-flow. *J. Fluid Mech.* (1986) 34, 595–608.
- [1-6] Steenbergen W. and Voskamp J.:The rate of decay of swirl in turbulent pipe flow. *Flow Meas. Instrum.* (1998) 9, 67–78.
- [1-7] Kuroda C. and Ogawa K.:Turbulent swirling pipe flow.In *Encyclopedia of Fluid Mech.,Vol.1* (editor N.P. Cheremisinoff). (1986) pp. 611–637. Gulf, London.
- [1-8] Binnie, A. M.:Experiments on the swirling flow of water in a vertical pipe and a bend.(1962)*Proc. Roy. Soc.*, 270, 452–466.
- [1-9] Chen, S. S.: Flow-induced in-plane instabilities of curved pipe, *Nuclear Engineering and Design*, 23–1, (1972), 29-38.
- [1-10] Ahmed, W.H., Evaluation of the proximity effect on flow-accelerated corrosion. (2010) *Annals of Nuclear Energy*, 37(4), pp.598-605.
- [1-11] Yamano, M., Tanaka, H., Murakami, M., Iwamoto. T., Yuki, Y., Sago, K. and Hayakawa, S. :Unsteady elbow pipe flow to develop a flow-induced vibration evaluation methodology for Japan Sodium-Cooled Fast Reactor.(2011) *J. Nucl. Sci. Technol.*, 48, pp. 677–687.
- [1-12] Vester, A.K., Örlü, R. and Alfredsson, P.H. Turbulent flows in curved pipes: recent ad-vances in experiments and simulations. (2016) *Applied Mechanics Reviews*, 68, 050802(1-25).
- [1-13] Al-Rafai, W. N., Tridimas, Y. D., and Woolley, N. H. A Study of Turbulent Flows in Pipe Bends, (1990) *Proc. Inst. Mech. Eng*, 204, 399–408.

- [1-14] Hilgenstock, A., and Ernst, R., Analysis of Installation Effects by Means of Computational Fluid Dynamics—CFD Versus Experiments? (1996) *Flow Meas. Instrument*, **7**, 161–171.
- [1-15] Kalpakli, A., and Örlü, R. Turbulent Pipe Flow Downstream a 90 degree Pipe Bend With and Without Superimposed Swirl. (2013) *Int. J. Heat Fluid Flow*, **41**, 103–111.
- [1-16] Yamano, H., Tanaka, M. A., Kimura, N., Oshima, H., Kamide, H. & Watanabe, O. (2011) Development of flow-induced vibration evaluation methodology for large diameter piping with elbow in Japan sodium-cooled fast reactor. *Nuclear Engineering and Design*, 241(11), 4464-4475.
- [1-17] Mizutani, J., Ebara, S., & Hashizume, H. Evaluation of the influence of the inlet swirling flow on the flow field in a triple elbow system. (2016) *International Journal of Hydrogen Energy*, **41**, 7233-7238.
- [1-18] Ebara, S., Takamura, H., Hashizume, H., & Yamano, H. Characteristics of flow field and pressure fluctuation in complex turbulent flow in the third elbow of a triple elbow piping with small curvature radius in three-dimensional layout. (2016) *International Journal of Hydrogen Energy*, **41**, 7139-7145.
- [1-19] Chang, T. H., and Lee, H. S., An Experimental Study on Swirling Flow in a 90 Degree Circular Tube by Using Particle Image Velocimetry. (2003) *J. Visualization*, **6**, 343–352.
- [1-20] Takeda, Y., Velocity profile measurement by ultrasound Doppler shift method, *Int. J. Heat Fluid Flow* (1986), 313-318.
- [1-21] Wada, S et al., Measurement of Environmental Flows using Ultrasonic Doppler Method", (2002), Proceedings of annual meeting, Japan Society of Fluid Mechanics, 339-346.
- [1-22] Treenuson, W., Accurate flowrate measurement on the double bent pipe using ultrasonic velocity profile method. *Journal of the Japanese Society for Experimental Mechanics*, 13(2), (2004), 200-211.
- [1-23] Takeda, Y. and Kikura, H., Flow mapping of the mercury flow". *Experiments in Fluids*, Vol.32 (2), (2002), 161-169.
- [1-24] Fukumoto, T et al., A study of phased array ultrasonic velocity profile monitor for flow rate measurement. *21st International Conference on Nuclear Engineering* (2013), V006T16A051-V006T16A051.



Figure 1.1. Failure in a high-pressure extraction line at Fort Calhoun (USA) in 1997.



Figure 1.2. Rupture at an 8-inch elbow of a moisture separator re-heater of Millstone Unit 2 (USA) in 1997.



Figure 1.3. An 18-inch elbow in a condensate line ruptured catastrophically (USA) in 1986.

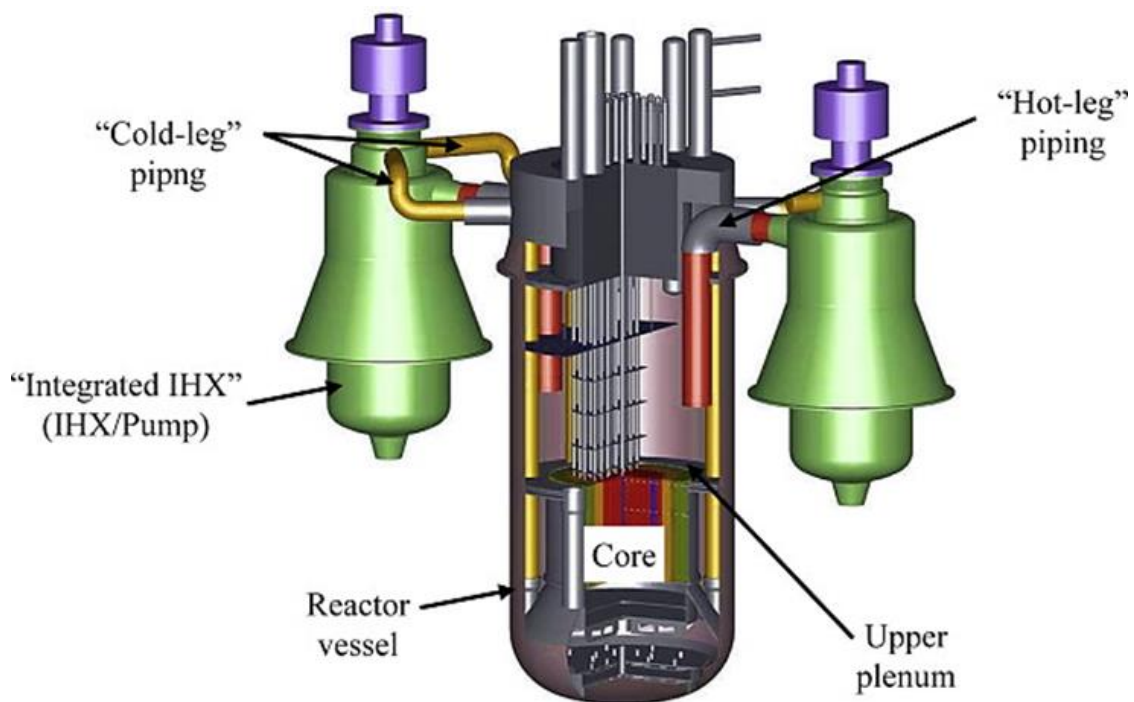


Figure 1.4. Schematic view of Japan Sodium-cooled Fast Reactor (JSFR) [1-16].

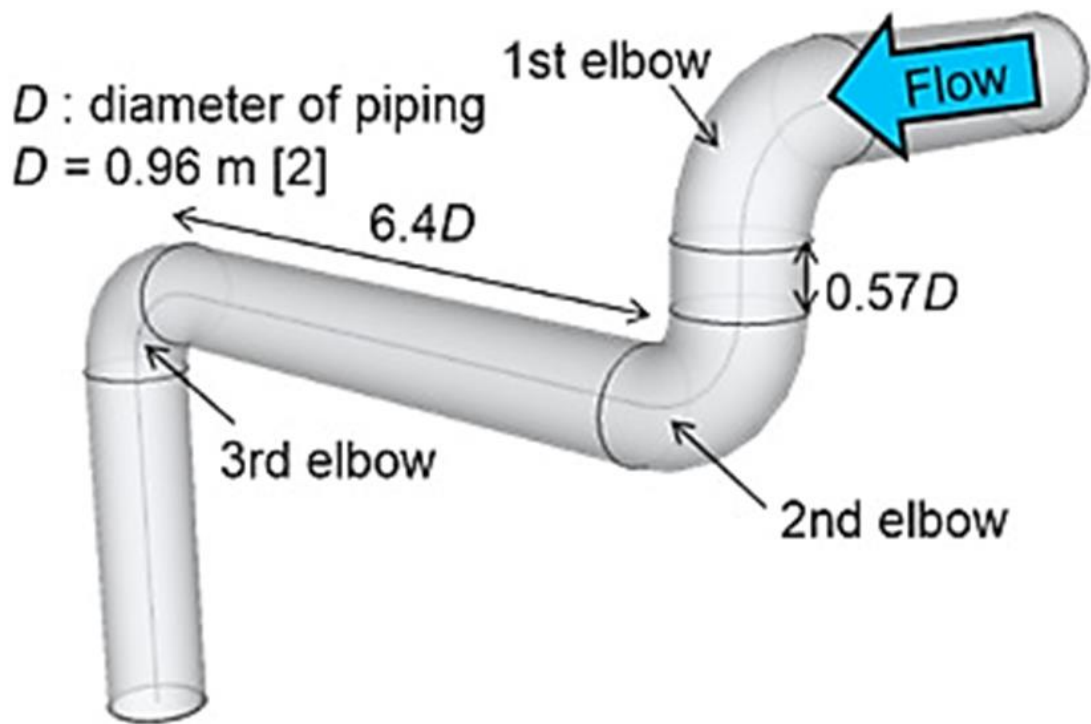


Figure 1.5. Schematic view of triple elbow pipe layout by Mizutani *et al.* [1-17].



Figure 1.6. Tangential injection method swirling generator by Mizutani *et al.* [1-17].

Chapter 2

**Numerical Investigation of
Turbulent Flow in a Single
Elbow Using Inlet Velocity
Profile**

2.1 Introduction

Pipe flow are the most common way to transport liquids and gases in the industrial and the power generation processes. In general, some parts of the piping system are curved due to the necessity to adopt to the geometrical or technical constraints of the system or to redirect the flow. In any pipe system, one would also expect to find bends of various angles and sharpness. Curve pipes or 90° elbows are commonly associated with strong secondary flow and increased pressure losses that are due to an instability set up by the centrifugal forces acting on the fluid as it passes through the bend. Especially, the main cooling system of JSFR consists of two loops hot-leg pipe having 90° elbow with curvature ratio ($\gamma = R/R_c = 1.0$). A compact layout of the primary cooling system is adopted in order to reduce the plant construction cost. Under such a condition in the cooling system, flow-induced vibration (FIV) is concerned from a view point of the structural integrity of pipe. The pressure fluctuation in the elbow is the sources of FIV excitation force. In general, the pressure fluctuation and the velocity fluctuation are closely related. Thus, the information of the flow field and velocity fluctuation under very high Reynolds number ($Re = 4.2 \times 10^7$) is needed in order to grasp the mechanism of FIV. However it is difficult to conduct an experiment at the high Reynolds number. Consequently, we must predict the flow structure up to such a high Reynolds number ($Re = 4.2 \times 10^7$) based on available experimental techniques and numerical simulations.

A number of scientists have been intrigued to investigate the phenomenon, starting with the study by Tunstall and Harvey (1968) at turbulent flows in L sharp 90° bends [2-1]. In their study at a Re-number of 4.0×10^4 in a sharp bend with a relative curvature of ratio ($\gamma = R/R_c = 1.0$), they used the tuft-type flow visualization technique. From observation of the flow, they found an alternating upwards and downwards tangential flow at the inner side of the curvature with low frequency behavior. For the further investigation, Brücker (1998) presented a quasiperiodic time-dependent

behavior of the secondary flow downstream of a bend in different time-scales by using Particle Image Velocimetry (PIV) method [2-2]. Sakakibara *et al.*, (2012) measured velocity distribution in cross sections of a fully developed turbulent pipe flow upstream and downstream of a 90 ° bend by synchronizing two sets of a (PIV) system. Unsteady undulation of Dean vortices formed downstream from the bend was characterized by the azimuthal position of the stagnation point found on the inner and outer sides of the bend [2-3]. Kalpakli *et al.*, (2012) employed PIV to seize the unsteady behavior of the Dean vortices at the exit of a 90 ° pipe bend at a Reynolds number and Dean number of 3.4×10^4 and 1.9×10^4 , respectively [2-4].

In case of numerical simulation, Rütten *et al.*, (2005) performed Large-eddy simulations to investigate the turbulent flows through the 90° pipe bend that feature unsteady flow separation, unstable shear layers, and an oscillation of the Dean vortices [2-5]. Single bends with curvature radii $R/R_c=1$ and $R/R_c=1/6$ are considered at the Reynolds number range ($Re = 5 \times 10^3 - 2.7 \times 10^4$). Hellström (2010) used Time-resolved stereoscopic particle image velocimetry is used to investigate the structure of the very-large-scale motions (VLSMs) in fully developed turbulent pipe flow [2-6]. The motions are visualized by using the snapshot Proper Orthogonal Decomposition (POD). It is shown that the structures can be reconstructed using a small number of the most energetic modes at Reynolds number ($Re=1.25 \times 10^4$).

In addition, the velocity fluctuation and flow phenomenon have also recently attracted the interest of the community in the nuclear sector due to the fatigue. Because the unsteady motion of the vortices can cause in the piping of the cooling system of a nuclear reactor and the impact that the unsteady secondary motion can have on the stability of the surrounded equipment. Therefore, Ono *et al.*, (2010) with the short-elbow and the long-elbow under ($Re = 1.8 \times 10^5$ and 5.4×10^5) conditions [2-7]. The velocity fields in the elbows were measured using a high-speed Particle Image Velocimetry (PIV). The time-series of axial velocity fields and the cross-section velocity fields obtained by the high-speed PIV measurements revealed the unsteady and complex flow structure in the elbow. The flow separation was observed in the short-

elbow. Yuki et al., (2011) investigated flow structure in a three-dimensionally connected dual elbow is visualized using a 1/15-scale experimental apparatus simulating the 1st and 2nd elbows of JSFR cold-leg piping [2-8]. To match the piping geometry with the 1st and 2nd elbows in the cold-leg piping, the two elbows are sterically connected through a circular straight pipe of 0.57D in length. The curvature ratio of the elbow is 1.0 ($=R/D$: where R is the curvature radius). Nevertheless, the mechanism, which triggers such a motion, is not fully understood yet and studies investigating its origin are still ongoing.

In the previous study, PIV measurement system and numerical simulation were applied to investigate fluid velocity and flow structure visualization. However, PIV system has some challenges and it is difficult for the applications in actual plant process. In addition, numerical simulations are only theoretical approach in some case. The theoretical approaches are sometime can be different from the actual problem. Therefore, the correct solution should be developed to evaluate velocity distribution and flow structure for a pipe flow in a compact piping system. In the present study, the combination of experiment and numerical simulation were performed to observe the turbulent intensity and velocity distribution in a single elbow with curvature ratio ($\gamma = R/R_c = 1.0$). Firstly, the fluid velocity measurements in a circular straight pipe are carried out using ultrasound technique. The fully develop region can be observed for the turbulent flow at several Reynolds number. Then, the velocity profiles from the measurement results are imposed as the inlet boundary condition for a single elbow simulation using CFD Fluent 16.2. The primary objectives of this chapter is to find out an appropriate Reynolds number for the experiment by using Phased Array UVP and the further objectives are presented as follows;

- The fluid flow structure and turbulent intensity are analyzed base on the different Reynolds number downstream of a single elbow.
- From this investigation, the appropriate Reynolds number is choice to use in the next chapter of the turbulent flow measurement and inlet swirling flow measurement.

2.2 One-dimensional velocity profile measurement

There are many devices for the fluid flow measurement. The differential flow meters such as an orifice, venture and nozzle have been usually used in the industries and the power plant. The flowmeters are used for the various purpose in all fluid flow measurement. In this study, the ultrasonic flowmeter is discussed to apply the flow measurement system of the power plant. Ultrasonic Velocity Profiler (UVP) is a non-destructive measurement system for an instantaneous velocity profile in liquid flow along the ultrasonic beam axis by detecting the Doppler shift of echoed ultrasound as a function of time. The Doppler shift frequency is directly related to the velocity value [2-9]. Therefore, the UVP system does not require a calibration procedure. The only required condition is that the tasted fluid should contain a sufficient amount of suspended small seeding particles (reflectors), on which the ultrasound echo originates.

The ultrasonic sound signals are transmitted from the transducer with the basic frequency f_0 and pass through into the flow with the incident angle θ_i along the measurement line as shown in **Figure 2.1**. And **Figure 2.2** shows a single transducer with basic frequency 4 MHz which Imasonic produces. When the ultrasonic sound signal hits a small particle in the liquid, part of the signal scatters on the particle and echoes back. The echo reaches the transducer with Doppler shift frequency f_d and after a time delay t . The time delay between transmitted and received signal can be calculated as following equation.

$$t = \frac{2x}{c} \quad (2.1)$$

where x is the distance of scattering particle from transducer and c speed of sound in the liquid.

If the scattering particle is moving with a velocity component into the measurement ultrasonic beam line, Doppler shift of echoed frequency takes place, and received signal frequency becomes Doppler shifted.

$$\frac{v}{c} = \frac{f_d}{2f_0} \quad (2.2)$$

where v is velocity component into transducer beam line and f_d Doppler shift frequency.

This Doppler shift frequency is proportional to the velocity component along the measuring line of the particle V_T . The velocity V_x in the axial direction can be calculated by equation

$$V_x = V_T / \sin \theta_f \quad (2.3)$$

UVP method can measure the flow rate with a single transducer. The flowrate was calculated by the integration of velocity distributions in the direction of y-direction (vertical direction across the centre of the pipe) and z-direction (horizontal direction), two perpendicular directions to x-direction or fluid flow direction.

$$Q = \iint V_x dz dy \quad (2.4)$$

In a straight pipe flow, if the measurement position is fully developed flow, the velocity profile measured from the fluid is symmetric and the flow rate Q can be obtained accurately by integrating only the half of the velocity profile.

The ultrasonic transducer can be placed outside of the pipe wall. Therefore, it can avoid any disturbance to the flow field. In addition, it can be used with opaque fluids such as dirty wastewater, liquid metals or chemical agents, to which optical methods like LDA (Laser Doppler Antimony) or flow visualisation cannot be applied.

2.2.1 Ultrasonic Velocity Profiler (UVP-Duo)

UVP-Duo is one of the UVP systems and it is shown in **Figure 2.1**. UVP-Duo can be used with various liquids over a wide range of flow configurations. It measures a velocity profile along a line both directly and instantaneously. This also enables one to measure multi-dimensional field of fluid flow. In addition, Doppler shift frequency is directly related to the velocity value; therefore, it does not require a calibration procedure. The parameters of the measurement system are designed mainly for water. UVP-Duo can also measure in organic liquids, liquid metals, ferromagnetic

liquid and polymeric fluid To conduct the flow mapping, UVP-Duo include an integrated multiplexer. In this system, the multiplexer and its controller are integrated into the UVP. The sequence and timing of multiplexer channels are controlled from UVP-Duo software. All measurement functions are contained in an UVP-Duo, while software with all its controlling and analysis functions is installed on a computer. UVP-Duo and computer are connected by an Ethernet link [2-9].

2.2.2 Velocity Profile Measurement in a Straight Pipe Using UVP-Duo

The flow rate measurement is important in the fluid mechanic engineering, the industries and the power plant. There are many flowmeters commonly used to measure the flow rate of liquids and gases flowing through the pipes or ducts. Measuring flow rate is usually done by measuring flow velocity and most flowmeters are simply velocity meters used for metering flow. For the obstruction flowmeters such as Orifice, Venturi and Nozzle meters, the measurement device can be used by obstructing the flow. The flow rate through a pipe can be determined by constricting the flow and measuring the decrease in the pressure due to the increase in velocity at the construction site. Differential pressure transducer or manometer can measure the pressure drop between two points along the flow. The electromagnetic flow meters and the ultrasonic flow meters are non-destructive flow meters. This study presents Doppler effect ultrasonic flow meters to apply in the feed flow rate measurement of the power plants. Ultrasonic Velocity Profile (UVP) method, which is able to measure velocity profiles directly can be applied to obtain the profile factor .A major application of the UVP system is the investigation of the flow rate of fluids. In this study, the flow rate is measured experimentally in a straight pipe by using UVP-Duo. Hardware system of UVP-Duo and ultrasound transduce are shown in **Figure 2.2.** and **Figure 2.3.**

2.2.3 Experimental apparatus

The experimental apparatus that consists of a circulation water system, cooling system and the test section **Figure 2.4**. It is designed to emphasize the formation of fully developed turbulent pipe flow. The valve can control the flow rate and the centrifugal pump drives the water to circulate. The pipeline system is almost made of Polyvinyl. For the test section, the straight pipe is made by acrylic and the inner diameter of the pipe is 50 mm. Water box is used to apply the water as the coupling between the transducer and the pipe in order get the same incident angle in the fluid medium by the Snell's law. **Figure 3.9** show the principle of Snell's law. In addition, the water box can reduce the external noise. Before the straight pipe, a flow conditioner is designed to include the tube bundle, mesh plates and a turbulence promoter ring was installed to realize uniform velocity profiles. The flow rate was monitored by an electromagnetic flow meter located upstream of the test section. The basic frequency of the transducer is 4 MHz as shown in **Figure 2.3**. To receive enough echo signal, the reflected particle should have a diameter at least equal to the quarter of the ultrasound beam wavelength. If the particle is smaller, the reflection efficiency becomes lower. The energy of echo is too small to maintain a high signal per noise ratio. In this experiment, the diameter of suspended particle is 80 μm and a specific gravity of 1.02. This particle size can interweave with water, and can reflect ultrasonic wave of 4 MHz. The density of the particle and the particles concentration are very important. A large different in densities between the fluid and particle does not follow the flow. When the concentration of particles is smaller, some points of profile may not be measured during a single ultrasound pulse. These points have zero value because of no reflection, or are set to zero by the algorithm when too weak a reflection is detected. Reynolds number is set from Re 1800 to Re 30000 to investigate the flow regime from laminar to turbulent. The test section is 5D, 10D, 18D, 24D and 30D (diameter of the pipe) from the inlet to define the fully developed region. **Table 2.1** shows the experimental condition.

2.3 Numerical Simulation Approach

Numerical simulation calculation can give fully three-dimensional velocity fields. In these days, computers are well developed, and numerical simulation becomes very popular and useful method to obtain velocity profiles because of its costs compare to the real experimental. Thus, simulation calculation was performed from the experimental condition and the numerical result was investigated two-dimensional velocity field, and turbulent intensity downstream of a single elbow.

2.3.1 Basic Theory

The numerical result was obtained by solving three-dimensional, Reynolds-averaged Navier–Stokes (RANS) equations by the commercial CFD code FLUENT® v.16.2 with RNG k-ε turbulence model. The Navier-Stokes equations are time-dependent and consist of a continuity equation for conservation of mass, three conservation of momentum equations and a conservation of energy equation. There are four independent variables in the equation x , y , and z spatial coordinates, and the time t . And also the six dependent variables such as the pressure p , density ρ , and three components of the velocity vector u , v and w . Together with the equation of state such as the ideal gas law - $p V = n R T$. In practice, these equations are too difficult to solve analytically. In the past, engineers made further approximations and simplifications to the equation set until they had a group of equations that they could solve. Recently, high-speed computers have been used to solve approximations to the equations using a variety of techniques like finite difference, finite volume, finite element, and spectral methods. This area of study is called Computational Fluid Dynamics or CFD.

In the present simulation, the governing equations for incompressible fluid flow is as follow;

$$\frac{\partial \rho}{\partial t} + \nabla \cdot (\rho u) = 0 \quad (2.5)$$

$$\frac{\partial u}{\partial t} + (u \cdot \nabla)u = -\frac{1}{\rho} \nabla p + F + \frac{\mu}{\rho} \nabla^2 u \quad (2.6)$$

where, the equation (1) and (2) are conservations of mass and momentum, respectively; u = velocity vector field, p = pressure, ρ = density, μ = kinematic viscosity, F = external force per unit mass. ($\nabla = \frac{\partial}{\partial x} i + \frac{\partial}{\partial y} j + \frac{\partial}{\partial z} k$ and $\nabla^2 = \frac{\partial^2}{\partial x^2} + \frac{\partial^2}{\partial y^2} + \frac{\partial^2}{\partial z^2}$)

2.3.2 Mesh Characteristics

Applicable mesh arrangement for the pipe elbow flow was already investigated by Tanaka *et al.*, [2-10]. Figures 2 (a) and (b) respectively show mesh arrangements of pipe layout at turbulent flow conditions for several Reynolds number ($Re = 1 \times 10^4$, $Re = 2 \times 10^4$ and $Re = 3 \times 10^4$) based on the experimental pipe layout. The geometric approximation in the mesh is an important parameter that influences the CFD simulations accuracy. A uniform and very smooth mesh, which leads to a more accurate numerical calculation. Thus, selection of the appropriate mesh size is crucial in compromise of the computational time and accurate numerical analysis. Initially, the computational grid is of a tetrahedral type and then the polyhedral mesh was converted in FLUENT calculation to get high performant of orthogonal and skewness values. The face sizing mesh method and inflection layer meshing were applied to precise the mesh quality in the boundary layer of the pipe wall. The minimum cell volume is $1.0 \times 10^{-11} \text{ m}^3$ and the maximum aspect ratio is 13. The total number of elements is 1.8 million. **Figure 2.1** and **Figure 2.2** respectively show mesh arrangements of pipe layout at turbulent flow conditions for several Reynolds number ($Re = 1 \times 10^4$, $Re = 2 \times 10^4$ and $Re = 3 \times 10^4$) based on the experimental pipe layout.

2.3.3 Turbulent Model and Wall Functions

The turbulence model has many kinds of calculations. The outstanding feature of a turbulent flow, in the opposite of a laminar flow, is that the molecules move in a chaotic fashion along complex irregular paths. The strong chaotic motion causes the various layers of the fluid to mix intensely. Because of the increased momentum and

energy exchange between the molecules and solid walls, turbulent flows lead at the same conditions to higher skin friction and heat transfer as compared to laminar flows. Although the chaotic fluctuations of the flow variables are of deterministic nature, the simulation of turbulent flows continues to present a significant problem.

In the consideration of turbulent model that turbulent flows are basically designated by the fluctuations of the velocity fields. Different transported quantities such as momentum, energy, etc. also fluctuate for this fluctuation of velocity field and these fluctuations can be of very high frequency and small scale; they are very difficult and computationally crucial to analyze directly in industrial engineering calculations. The turbulence model needs to be selected based on some considerations, e.g., the physics of the flow, the insight into the capabilities and limitations of turbulence models, the attempt for the specific problem by other researchers, the accuracy needed, the available computational resources, and time.

The k - ϵ (RNG) turbulence model is adopted for the present study as k - for this single-phase flows in a single elbow pipe layout [2-11, 2-12 and 2-13]. In this model, the turbulence kinetic energy (k) and the turbulence dissipation rate (ϵ) are solved to determine the coefficient of turbulent viscosity (μ_t) .

The k-epsilon model has been shown to be useful for free-shear layer flows with relatively small pressure gradients. Similarly, for wall-bounded and internal flows, the model gives good results only in cases where mean pressure gradients are small; accuracy has been shown experimentally to be reduced for flows containing large adverse pressure gradients. One might infer then, that the k -epsilon model would be an inappropriate choice for problems such as inlets and compressors.

The description equations of the turbulent model illustrate as:

Turbulent Kinetic Energy Equation:

$$\frac{\partial(pk)}{\partial t} + \frac{\partial(pku_i)}{\partial x_i} = \frac{\partial}{\partial x_j} \left(\frac{\mu_t}{\sigma_k} \frac{\partial k}{\partial x_j} \right) + 2\mu_t E_{ij} E_{ij} - \rho\epsilon \quad (2.7)$$

$$\frac{\partial(p\varepsilon)}{\partial t} + \frac{\partial(p\varepsilon u_i)}{\partial x_i} = \frac{\partial}{\partial x_j} \left(\frac{\mu_t}{\sigma_\varepsilon} \frac{\partial k}{\partial x_j} \right) + C_{1\varepsilon} \frac{\varepsilon}{k} 2\mu_t E_{ij} E_{ij} - C_{2\varepsilon} \frac{\varepsilon^2}{k} \quad (2.8)$$

where, u_i represents the velocity component in the corresponding direction, E_{ij} represents component of rate of deformation, and μ_t represents eddy viscosity. Equations (3) and (4) also consist of some adjustable constants [2-15] these are as follows

$$C_\mu=0.09 \quad \sigma_\kappa=1.00 \quad \sigma_\kappa=1.00 \quad \sigma_\varepsilon=1.30 \quad C_{1\varepsilon}=1.44 \quad C_{2\varepsilon}=1.92$$

The wall functions are a set of semi empirical functions used to satisfy the physics of the flow in the near wall region. Turbulence is affected in many ways by the presence of the wall through the non-slip condition that must be satisfied at the wall. Non-Equilibrium Wall Functions is set up as a wall function.

2.3.4 Boundary Conditions

The turbulence model has many kinds of calculations. The outstanding feature of a turbulent flow, in the opposite of a laminar flow, is that the molecules move in a chaotic fashion along complex irregular paths.

In case of CFD modelling of turbulent flow all CFD solvers needs turbulence quantities to be specified at inflow boundaries. The turbulent quantities at inlet depends on flow velocity, inlet geometry (area, perimeter and hydraulic diameter) and fluid properties.

There are many ways, which can provide turbulence conditions at inlet. Most of the CFD solvers has one or all of below methods:

- Turbulent kinetic energy (k) and turbulent dissipation (ε)
- Turbulent kinetic energy (k) and specific rate of dissipation (ω)
- Intensity (I) and length scale (l)
- Intensity (I) and viscosity ratio (μ_t/μ)
- Intensity (I) and hydraulic diameter (d)

When providing the turbulence values at inlet, one has to make sure to provide good approximation to avoid solution convergence issues and unphysical turbulence values. Following section gives details about equations used in this simulation.

Turbulence Intensity (I) - Turbulence intensity is defined as ratio of root mean square of the velocity fluctuations u' , to the mean flow velocity u_{avg} . A turbulence intensity of 1% or less is generally considered low and turbulence intensities and greater than 10% are considered high. The turbulence intensity at the core of a fully developed duct flow can be estimated as:

$$I = \frac{u'}{u_{avg}} = 0.16(Re)^{-1/8} \quad (2.9)$$

Turbulent Kinetic Energy (k) - Turbulence kinetic energy is the mean kinetic energy per unit mass associated with eddies in turbulent flow. Physically, the turbulence kinetic energy is characterized by measured root-mean-square (RMS) velocity fluctuations. Turbulence kinetic energy can be calculated (for smooth duct) using following equation:

$$k = \frac{3}{2} (u_{avg} I)^2 \quad (2.10)$$

Turbulent Dissipation Rate (ϵ) -Turbulence dissipation, is the rate at which turbulence kinetic energy is converted into thermal internal energy. It is given by:

$$\epsilon = (C_{\mu})^{3/4} \frac{k^{3/2}}{l} \quad (2.11)$$

The velocity profile from the experiment was imposed as the inlet velocity. The boundary condition of outlet is outflow and no-slip wall condition.

2.3.5 Pressure-Base Solver Setting

ANSYS FLUENT allows you to choose one of the two numerical methods:

- pressure-based solver
- density-based solver

The pressure-based approach was developed for incompressible flows, while the density-based approach was mainly used for compressible flows. In both methods, the velocity field is obtained from the momentum equations. In this study, steady flow pressure-based solver is adopted to calculate velocity field. The momentum and continuity equations and their solution by means of the pressure-based solver are addressed. These special practices are most easily described by considering the steady-state continuity and momentum equations in integral form:

$$\oint \rho \vec{v} \cdot d\vec{A} = 0 \quad (2.12)$$

$$\oint \rho \vec{v} \cdot d\vec{A} = -\oint p I \cdot d\vec{A} + \oint \vec{T} \cdot d\vec{A} + \int_V \vec{F} dV \quad (2.13)$$

where I is the identity matrix, \vec{T} is the stress tensor, and \vec{F} is the force vector.

In case of pressure-velocity coupling, ANSYS FLUENT provides the option to choose among five pressure-velocity coupling algorithms: SIMPLE, SIMPLEC, PISO and Coupled for steady flows. In this simulation, we used PISO algorithm. The Pressure-Implicit with Splitting of Operators (PISO) pressure-velocity coupling scheme, part of the SIMPLE family of algorithms, is based on the higher degree of the approximate relation between the corrections for pressure and velocity. One of the limitations of the SIMPLE and SIMPLEC algorithms is that new velocities and corresponding fluxes do not satisfy the momentum balance after the pressure-correction equation is solved. As a result, the calculation must be repeated until the balance is satisfied.

For the spatial discretization, Green-Gauss Node-Based solution was used as the gradients due to the unstructured meshes at the curvature part of elbow. Interpolation schemes for calculating cell-face pressures used PRESTO! scheme was used Interpolation schemes for calculating cell-face pressures because the fluid flows as turbulent swirling flow. QUICK scheme is applied for other spatial discretization for hexahedral meshes, where unique upstream and downstream faces and cells can be identified. The QUICK scheme will typically be more accurate on structured meshes aligned with the flow direction. ANSYS FLUENT allows the use of the QUICK scheme

for unstructured meshes. The solution is initialized by hybrid initialization and the solution controls for under-relaxation factor is default setting.

2.4 Results and discussion

2.4.1 One-dimensional velocity profile measurement results

The measurement of fully developed turbulent pipe flow is investigated to understand the turbulent flow in pipes and the analysis of fully developed. From **Figure 2.6** to **Figure 2.9** show the measurement velocity profiles at the several Reynolds number. These results show that the measurement sections are not in the fully developed region. In the entrance region, the velocity is changing and velocity profiles are not symmetric. In **Figure 2.10**, the velocity profiles in the developed region are compared to confirm fully developed turbulent flow at Re 30000. From this measurement results, the fully developed turbulent region can be decided and it starts from 24D because the velocity profiles at 24D and 30D are symmetric and same. The velocity does not change from 24D. For the flow rate measurement, the measurement section has been decided to get fully developed flow. The measurement is conducted from laminar to turbulent flow at Re 1800 to Re 30000. The flow rate results from the experiment are compared with the electromagnetic flow meter. The electromagnetic flow meter has error 0.54% according to from the calculation manual. The experimental results have error less 1% Reynolds number 5300 and 30000. **Table 2.2** shows the error of this measurement in volumetric flow rate.

2.4.2 Numerical simulation results

The experimental velocity profiles at Reynolds number 10,000, 20,000 and 30,000 were imposed as the inlet condition of the CFD numerical simulation. Then, the velocity field and turbulent kinematic energy were investigated from the numerical simulation results. **Figure 2.11** shows the geometry of a simulated single elbow pipe. **Figure 2.12** shows the mesh layout at the cross-section of the pipe. The

average size of meshes is 0.1 mm and boundary layers of 5 meshes are placed near the pipe wall. The thickness of the boundary layer at the vicinity of the wall is 0.015 mm, and the thickness becomes gradually larger with the distance from the wall. The number of meshes is 1.8 million. The distribution of the velocity field and turbulent kinetic energy are visualized as the contour plot from

Figure 2.13 to **Figure 2.15** in case of different Reynolds number. The results shows that turbulent kinetic energy is increasing in the low velocity region just downstream of the inner elbow wall (intrados). The high velocity occurs at the outer wall of the elbow end (extrados).

Figure 2.16 shows the axial velocity field downstream region of a single elbow in different Reynolds number. In the secondary region (from $x/D = 0$ to $x/D = 1$), the reverse flow was observed from the reattachment point at $x/D = 1$ to the inner edge of the elbow. The reattachment point is located at near $x/D = 1$ for the flow condition with different Reynolds numbers.

Figure 2.17 shows the tangential velocity field in the cross-section plane downstream region of a single elbow at $x/D = 0$. **Figure 2.18** shows the tangential velocity field in the cross-section plane downstream region of a single elbow at $x/D = 0.5$. **Figure 2.19** shows the tangential velocity field in the cross-section plane downstream region of a single elbow at $x/D = 1$. The tangential flow structure is same in three different Reynolds number case. Therefore, we can use the future investigation by using a single Reynolds number. In the next chapters, we are going to investigate experimentally the flow structure in a compact pipe, which make with the double and triple elbow.

2.5 Conclusions

From the one-dimensional velocity measurement, we confirmed that The fully developed turbulent flow starts from 24D because the velocity profiles at 24D and 30D are symmetric and same. The velocity does not change from 24D. For the flow

rate measurement, the measurement section has been decided to get fully developed flow. The measurement is conducted from laminar to turbulent flow at Re 1800 to Re 30000. The flow rate results from the experiment are compared with the electromagnetic flow meter. The electromagnetic flow meter has error 0.54% according to from the calculation manual. The experimental results have error less 1% Reynolds number 5300 and 30000.

In this chapter, the primary objective is to find out an appropriated Reynolds number to utilized in the experimental condition by using Phased Array UVP. We observed that the axial and tangential flow structure downstream of a single elbow does not change even we used different Reynolds number. The fluid velocity field and turbulent kinetic energy were shown as contour plots. The turbulent kinetic energy is increasing in the low velocity region just downstream of the inner elbow wall (intrados). The high velocity occurs at the outer wall of the elbow end (extrados). From this investigation, the appropriate Reynolds number is choice to use in the next chapter of the turbulent flow measurement and inlet swirling flow measurement.

References

- [2-1] Tunstall, M.J. and Harvey, J.K., On the effect of a sharp bend in a fully developed turbulent pipe-flow. (1968) *Journal of Fluid Mechanics*, 34(3), pp.595-608.
- [2-2] Brücker, C., A time-recording DPIV-study of the swirl switching effect in a 90 ° bend flow. (1998) In *Proceedings of the Eight International Symposium on Flow Visualization, Sorrento, Italy*. D. A. Nield and A. Bejan, Convection in Porous Media, New York: Springer, (2013).
- [2-3] Sakakibara, J. and Machida, N., Measurement of turbulent flow upstream and downstream of a circular pipe bend. (2012) *Physics of fluids*, 24(4), p.041702.
- [2-4] Kalpakli, A., Örlü, R. and Alfredsson, P.H., Dean vortices in turbulent flows: rocking or rolling?. (2012) *Journal of visualization*, 15(1), pp.37-38..
- [2-5] Rütten, F., Schröder, W. and Meinke, M. Large-eddy simulation of low frequency oscillations of the Dean vortices in turbulent pipe bend flows. (2005) *Physics of Fluids*, 17(3), p.035107. Y. Su and J. H. Davidson, Modeling Approaches to Natural Convection in Porous Media, New York: Springer, (2015).
- [2-6] Hellström, L.H., Sinha, A. and Smits, A.J., Visualizing the very-large-scale motions in turbulent pipe flow. (2011) *Physics of Fluids*, 23(1), p.011703..
- [2-7] Ono, A., Kimura, N., Kamide, H. and Tobita, A., Influence of elbow curvature on flow structure at elbow outlet under high Reynolds number condition. (2011) *Nuclear Engineering and Design*, 241(11), pp.4409-4419.
- [2-8] Yuki, K., Hasegawa, S., Sato, T., Hashizume, H., Aizawa, K. and Yamano, H., Matched refractive-index PIV visualization of complex flow structure in a three-dimensionally connected dual elbow. (2011) *Nuclear Engineering and Design*, 241(11), pp.4544-4550.
- [2-9] UVP monitor Model UVP- Duo user's guide.
- [2-10] Tanaka, M.A., Ohshima, H. and Monji, H., Numerical investigation of flow structure in pipe elbow with large eddy simulation approach. In *ASME 2009 Pressure Vessels and Piping Conference* (pp. 449-458). American Society of Mechanical Engineers.

- [2-11] Dutta, P., Saha, S.K., Nandi, N. and Pal, N., Numerical study on flow separation in 90 pipe bend under high Reynolds number by k- ϵ modelling. 2016, *Engineering Science and Technology, an International Journal*, 19(2), pp.904-910.

Table 2.1 Experimental parameters of straight pipe flow measurement

Parameter	Value
Pipe Diameter (D)	50 mm
Basic frequency	8 MHz
Reynolds number Re	1800 to 30000
Channel Distance[mm]	0.74
Incline Angle of Transducer[degree]	10
Water Temperature [Degree Celsius]	± 20 °C
Number of Channels	108

Table 2.2 Error of volumetric measuring method

Reynolds number (Re)	Electromagnetic flow meter (L/min)	Experimental results [L/min]	% error
1800	4.26	4.21	1.18
3000	7.10	7.25	2.06
5300	12.50	12.45	0.40
10000	23.60	24.12	2.15
15000	35.40	36.21	2.23
20000	47.20	48.26	2.19
30000	70.70	71.21	0.71

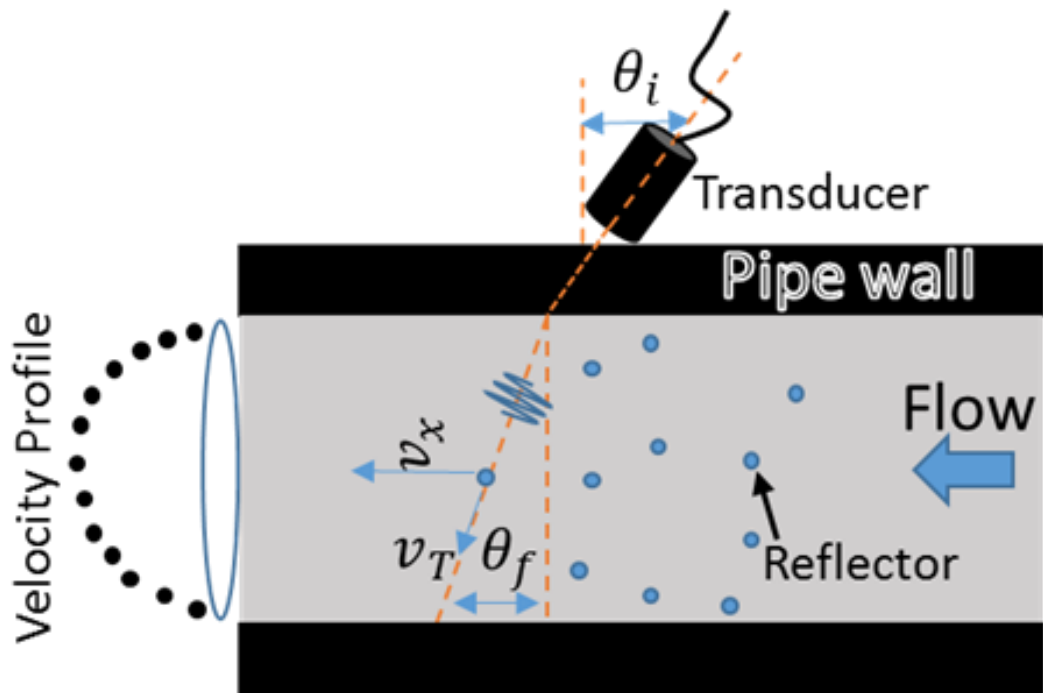


Figure 2.1. The principle of one-dimensional velocity profile measurement.

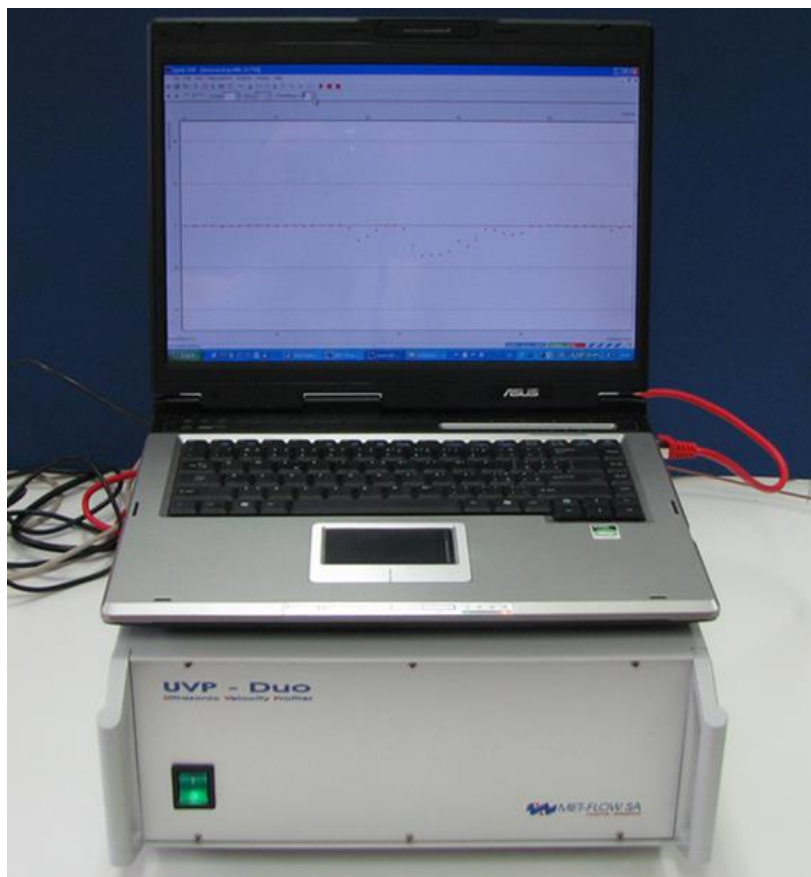


Figure 2.2. Hardware system of UVP-Duo.

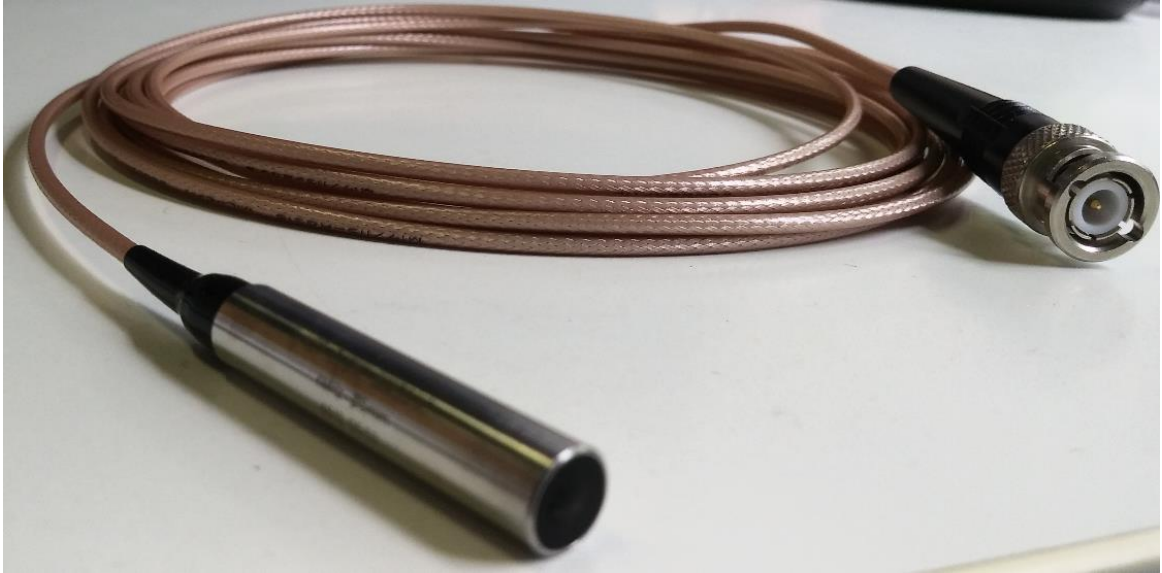


Figure 2.3. Single element ultrasound transducer.

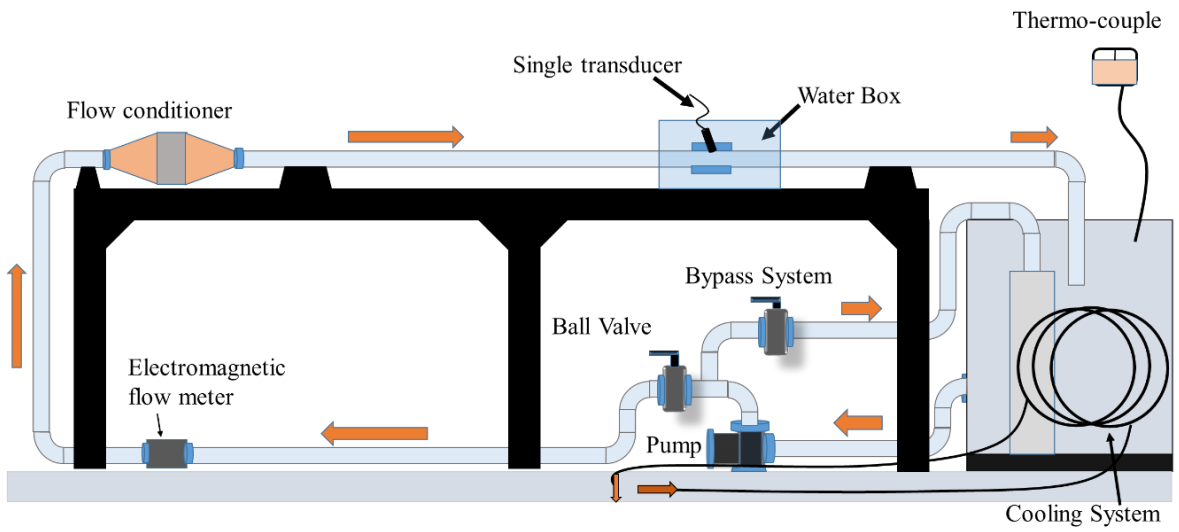


Figure 2.4. Schematic view of straight pipe flow measurement set up.

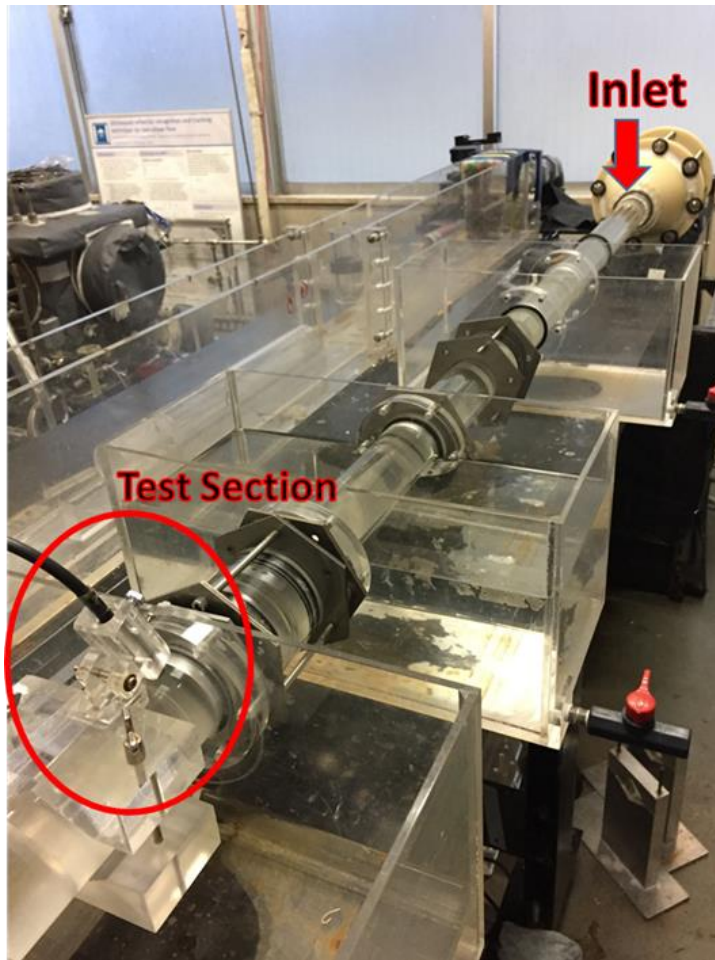


Figure 2.5. Picture of straight pipe flow measurement set up.

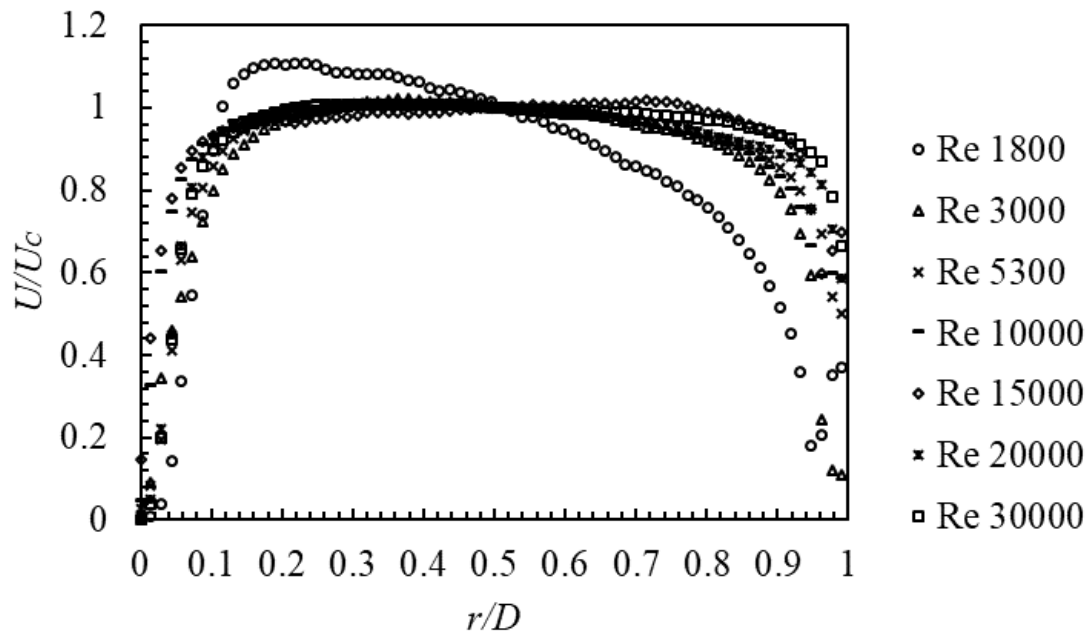


Figure 2.6. Velocity Profiles at 10D using UVP-Duo.

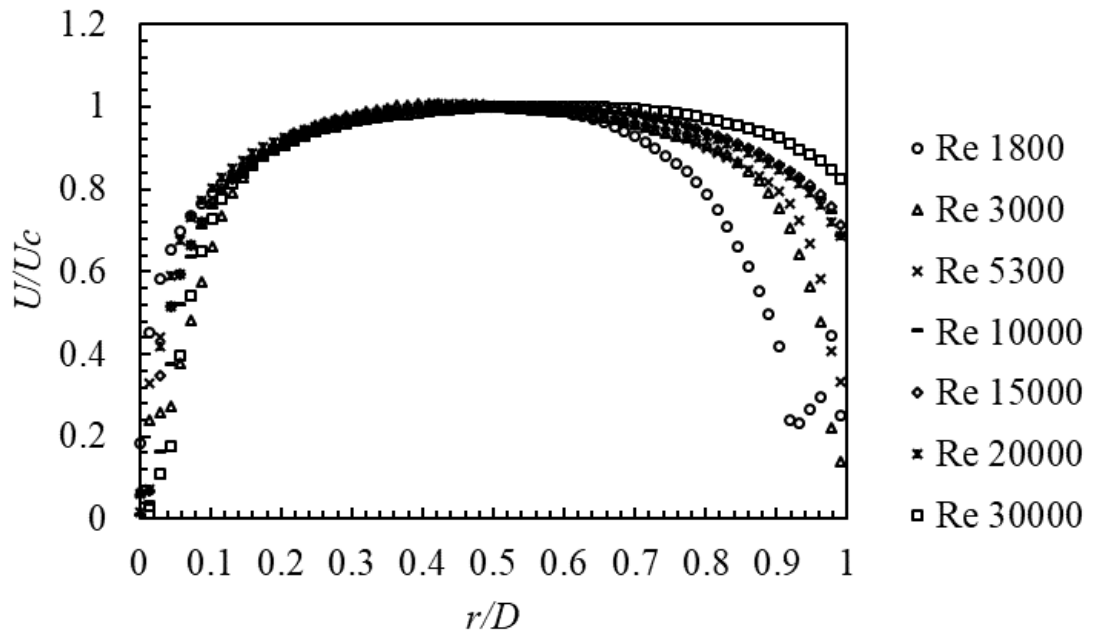


Figure 2.7. Velocity Profiles at 18D using UVP-Duo.

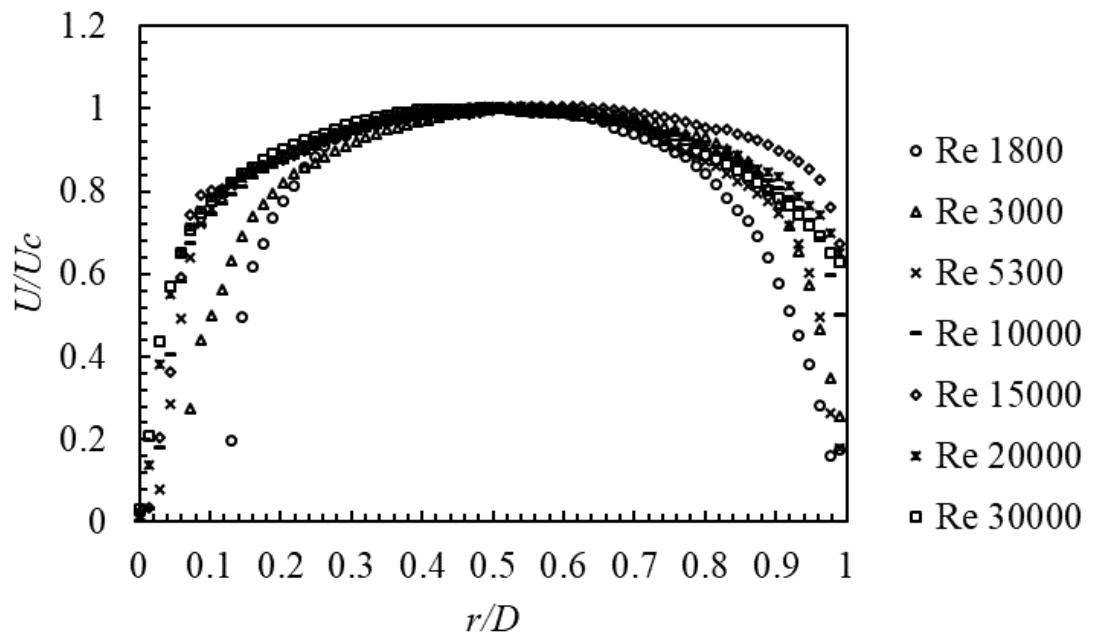


Figure 2.8. Velocity Profiles at 24D using UVP-Duo.

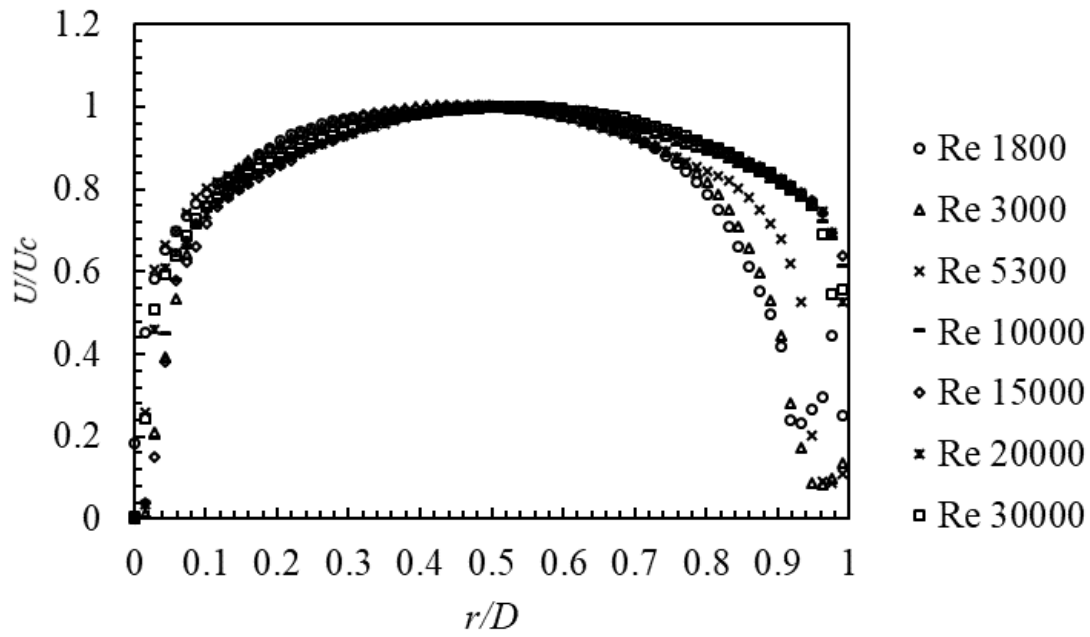


Figure 2.9. Velocity Profiles at 30D using UVP-Duo.

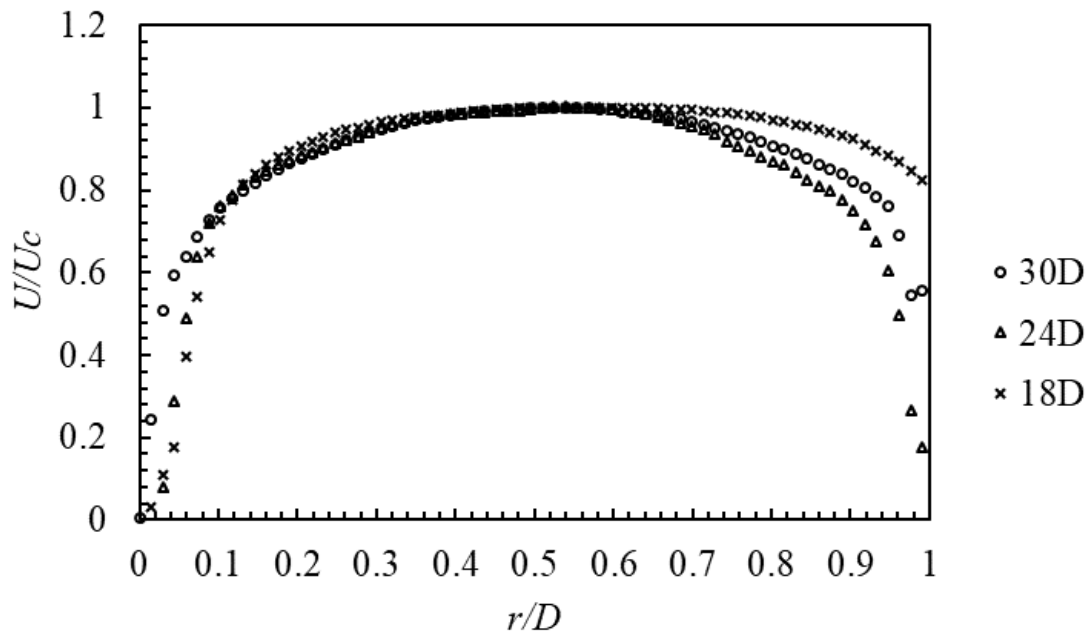


Figure 2.10. Velocity Profiles in the developed region at Re 30000.

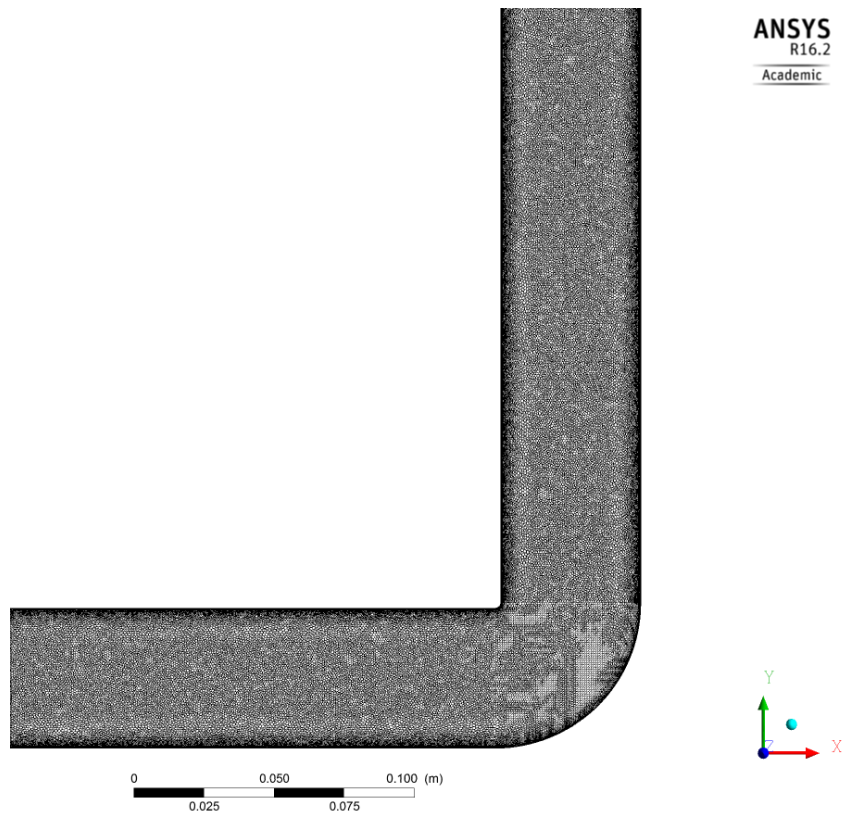


Figure 2.11. Geometry of a simulated single elbow.

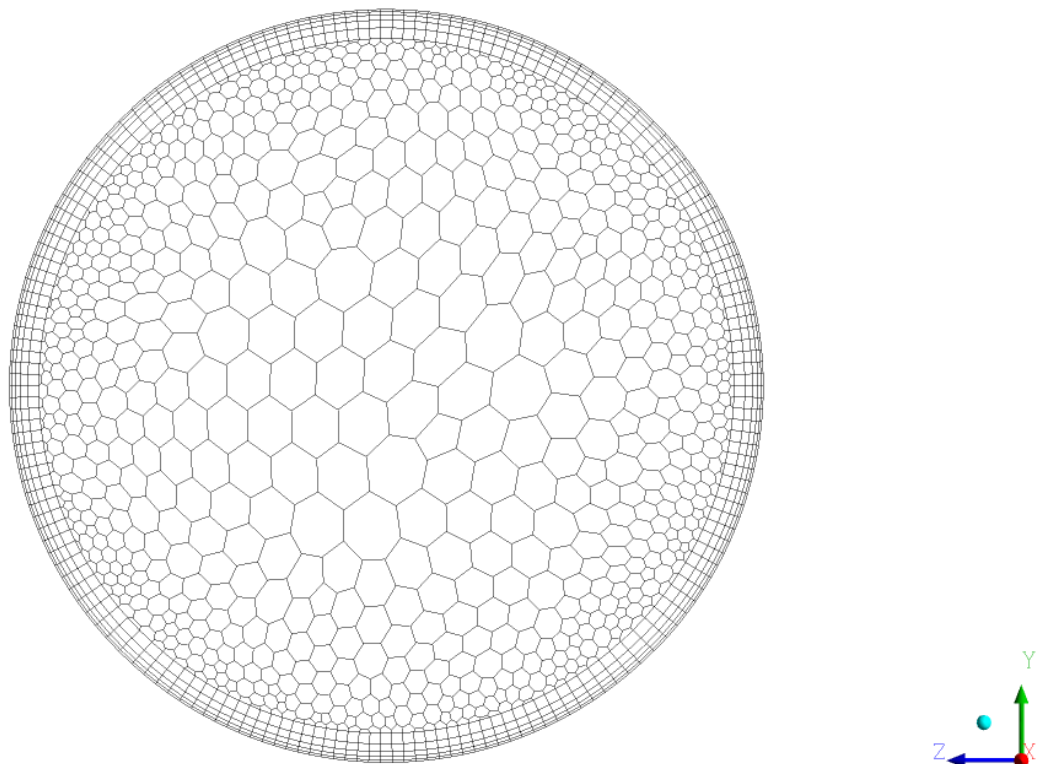


Figure 2.12. Mesh quality of the cross-sectional plane.

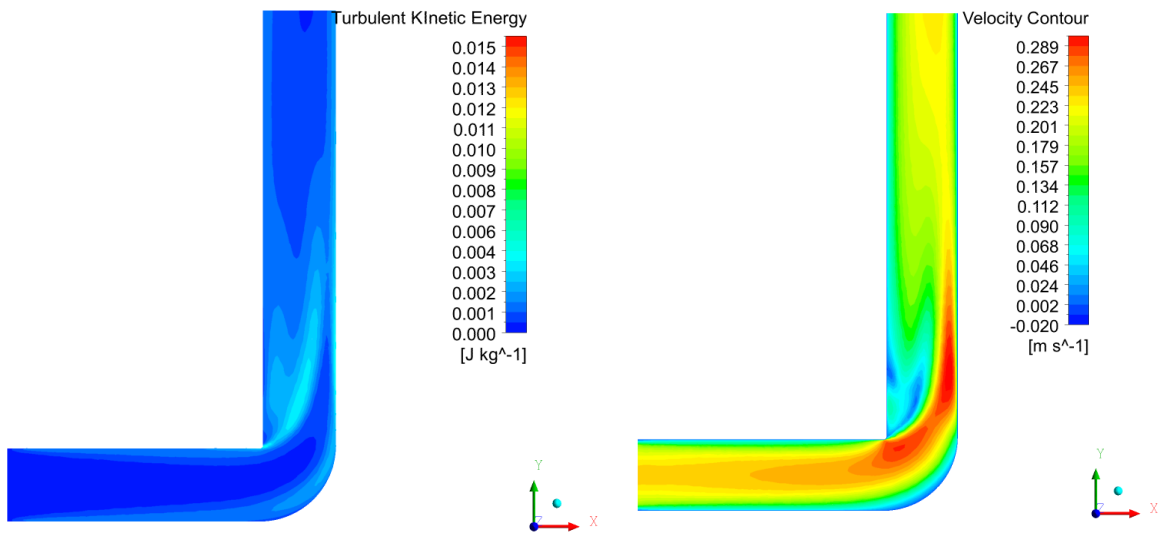


Figure 2.13. Turbulent Kinetic Energy and Velocity Contour at Re 10,000.

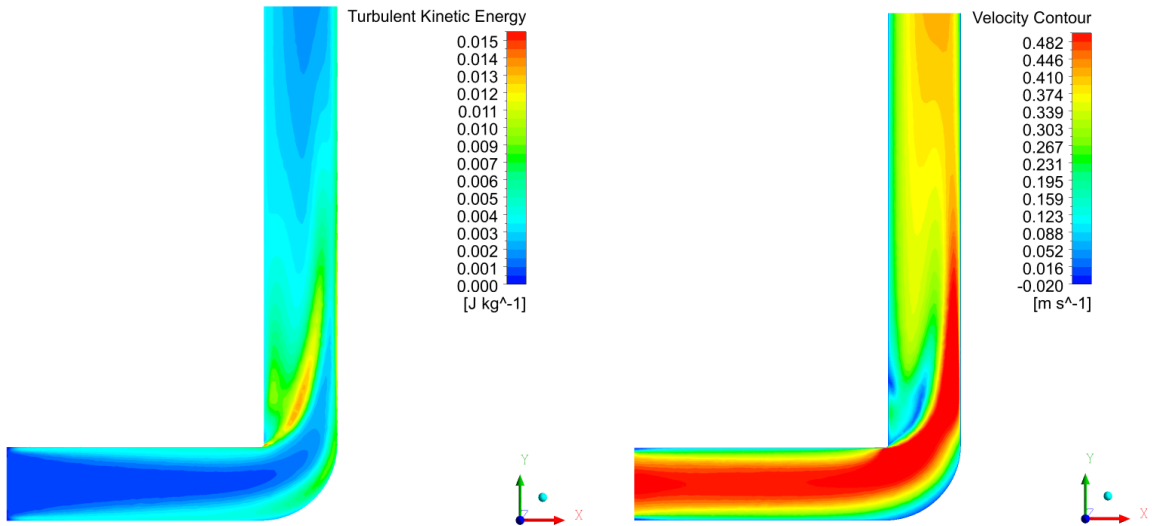


Figure 2.14. Turbulent Kinetic Energy and Velocity Contour at Re 20,000.

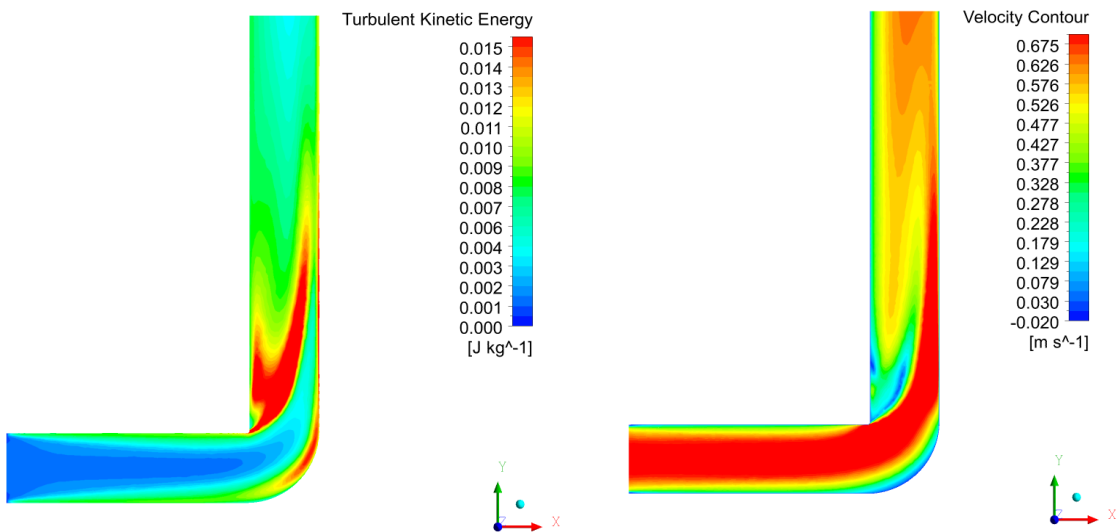
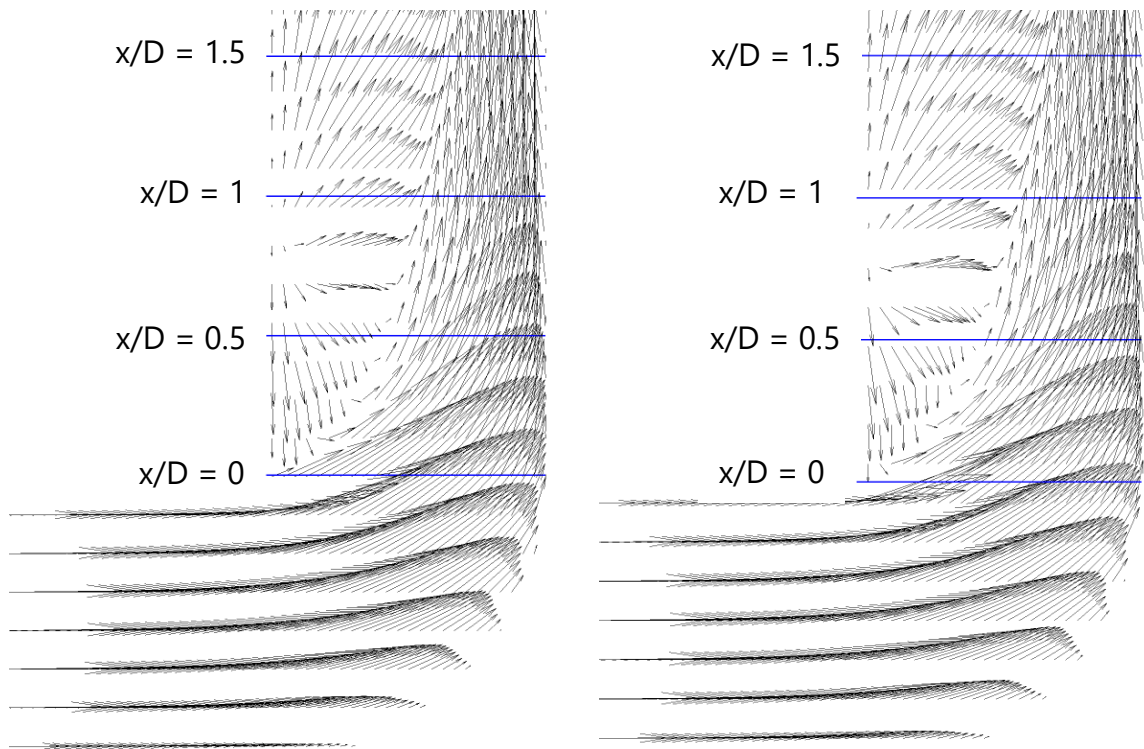
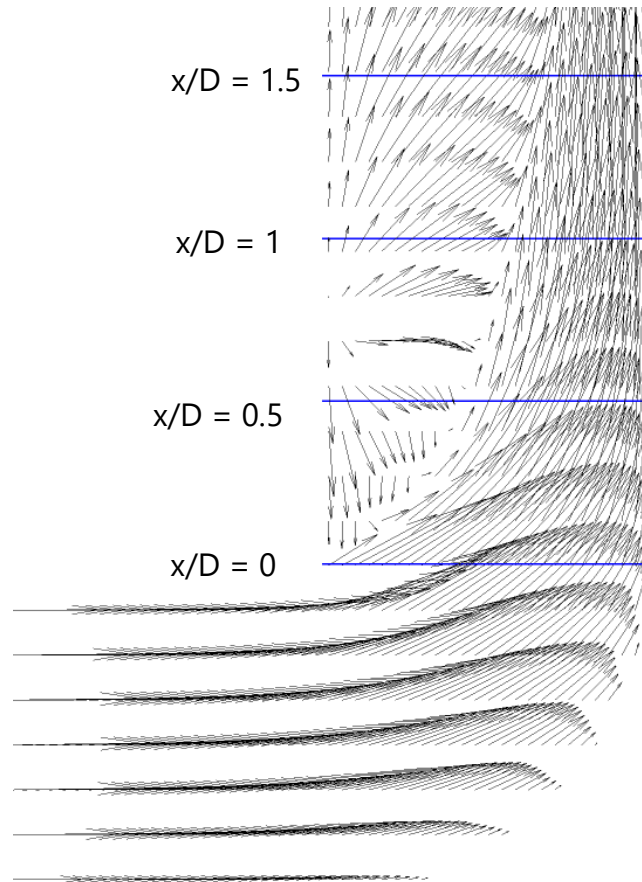


Figure 2.15. Turbulent Kinetic Energy and Velocity Contour at Re 30,000.



(a) Re 10,000

(b) Re 20,000



(c) Re 30,000

Figure 2.16. Axial velocity field downstream of a single elbow.

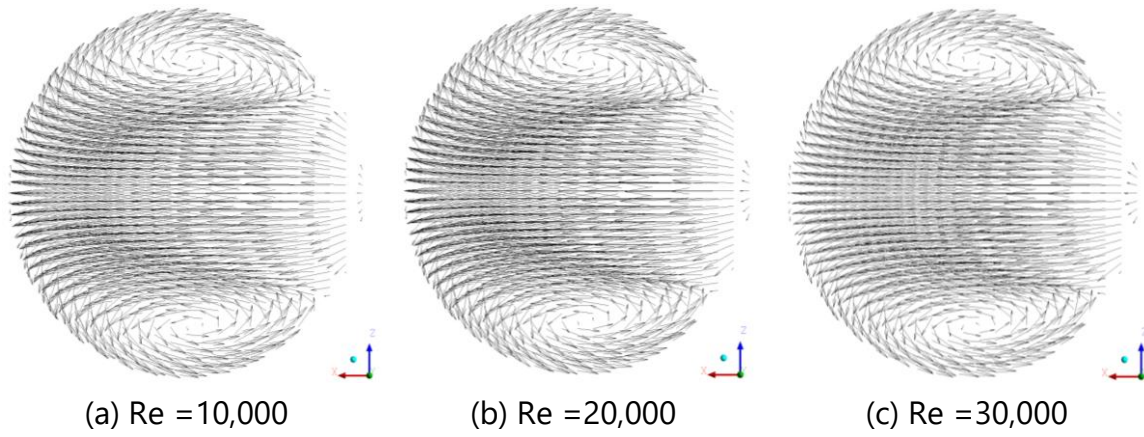


Figure 2.17. Tangential velocity field downstream of a single elbow in cross-section plane at $x/D = 0$.

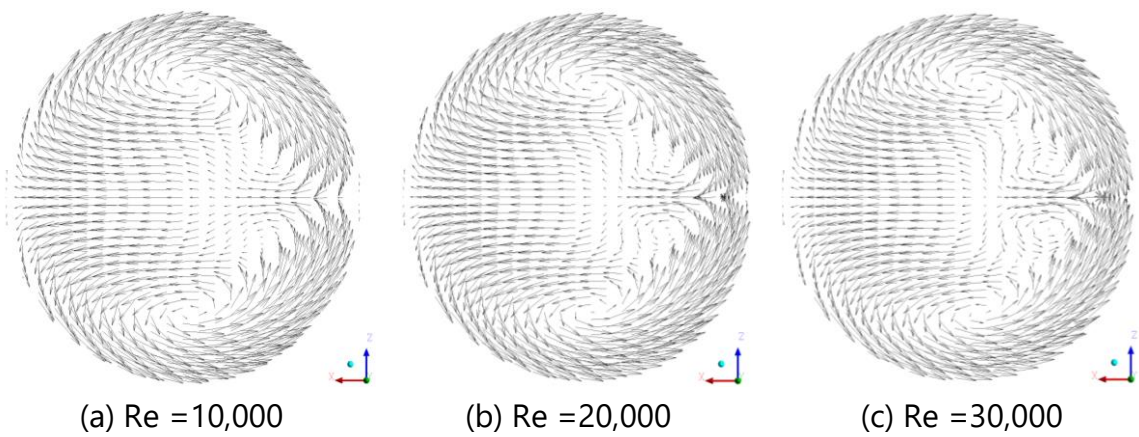


Figure 2.18. Tangential velocity field downstream of a single elbow in cross-section plane at $x/D = 0$.

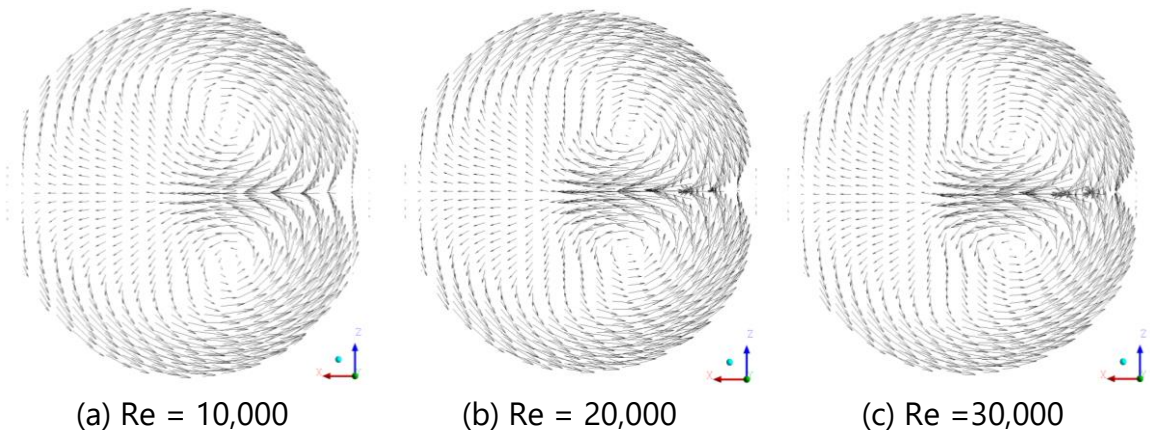


Figure 2.19. Tangential velocity field downstream of a single elbow in cross-section plane at $x/D = 1$

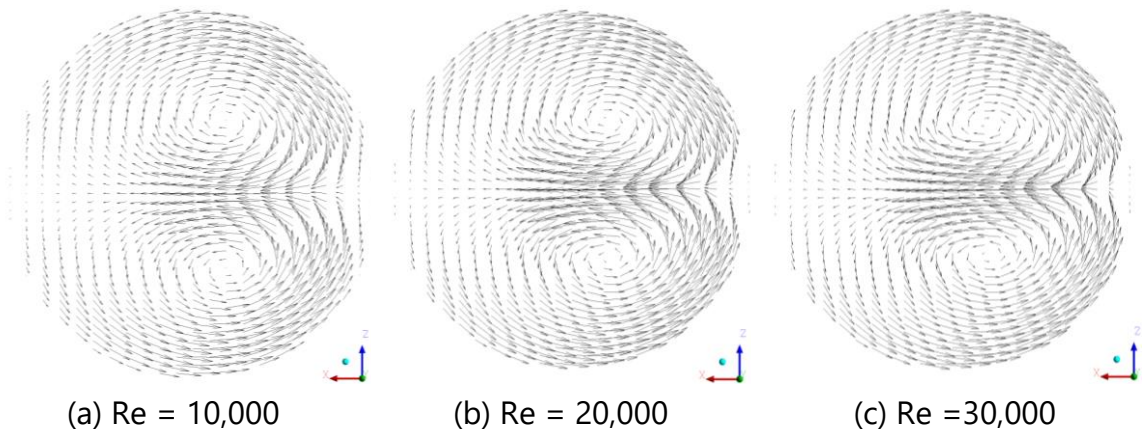


Figure 2.20. Tangential velocity field downstream of a single elbow in cross-section plane at $x/D = 1.5$

Chapter 3
Turbulent Flow Measurement
Downstream of Double Elbow
Using Phased Array
UVP and PIV

3.1 Introduction

In fluid dynamic engineering, some researchers are studying the characteristic of swirling turbulent flow in the circular pipe or the rectangular channel due to its complexity. Turbulent flow can be found in engineering process such as in gas cyclone [3-1], turbine [3-2], and rod bundle in a nuclear reactor [3-3]. The recirculated swirling flow could also occur just downstream of the elbow or 90-degree bend pipe. The bent pipe can be encountered in many piping systems of the industries. Under the recirculating flow condition, the significant pressure fluctuation and the high-velocity fluctuation happen in the elbows, and these are sources of flow-induced vibration (FIV) [1-9]. FIV can cause the corrosion phenomenon of the pipe wall, and the pipe break accident may occur in a piping system of the industries and the power plants. Therefore, the characteristic of flow field and velocity fluctuation are significant issues for the pipeline safety.

In the previous studies, the influence of swirling flow was investigated downstream of elbow and orifice in different swirl intensities [3-4]. In that experiment, the effect of swirling flow on the pipe wall thinning was observed by using plaster dissolution method and the velocity field was visualized using stereo particle image velocimetry (PIV). Moreover, the influence of elbow curvature on flow structure of the elbow outlet under high Reynolds number condition was investigated to get the information of velocity fluctuation and flow-induced vibration [2-7]. The flow-induced vibration (FIV) occurs, especially in a short-elbow pipe. Therefore, Mizutani *et al.* [1-17] investigated the influence of inlet condition upstream the triple elbow. Particle Image Velocimetry (PIV) was used for the velocity flow mapping, and the tangential injection method was used to generate the fluid swirling flow in their study. The triple elbow with short curvature radius was used to be close to an actual condition and to accumulate knowledge towards optimization of a prospective piping layout in the conceptual design of Japan Sodium Fast Reactor (JSFR) [1-18]. In the previous studies, the researchers mostly used the optical system to measure the velocity field and velocity fluctuation. However, the optical system has some

challenges to apply in non-transparent wall channel or pipe. Also, it is difficult for the applications in actual plant process. On the other hand, another measurement technique should be developed to evaluate the velocity field and velocity fluctuation. The developed measurement technique should be multidimensional and can be applied in the non-transparent conditions

Takeda [1-20] developed Ultrasonic Velocity Profiler (UVP) to measure instantaneous velocity profile for non-transparent media and opaque liquid flows. Originally, conventional UVP method only measures one-dimensional velocity profile in the measurement line. In the case of two-dimensional velocity vector measurement, Takeda and Kikura [1-23] investigated velocity field of the mercury flow using UVP system with multiple transducers. Nevertheless, the measurement system using multiple transducers is quite large as the number of transducers is increased. To minimize this problem, the authors had developed Phased Array Ultrasonic Velocity Profiler (Phased Array UVP). In Phased Array UVP, the sensor has multiple ultrasonic piezoelectric elements and ultrasound beam can be steered to a specific angle by controlling time delay of ultrasound transmission from each piezoelectric element. Therefore, velocity profiles can be measured in multiple measurement lines. For the flow mapping, Fukumoto *et al.* [1-24] confirmed Phased Array UVP for velocity flow mapping for detecting water leakage in the tank.

The main objective is to investigate velocity fluctuation of secondary flow downstream of the double bend pipe applying Phased Array UVP. Two-dimensional velocity field from the measurement of Phased Array UVP is compared with PIV method and the axial and radial velocity fluctuation are analyzed in one-dimensionally.

3.2 Two-dimensional Velocity by Phased Array UVP

Phased Array UVP based on Doppler shift frequency detection along ultrasound beamlines. The working principle of Phased Array UVP system based on

Doppler shift frequency detection along ultrasound beamlines. Phased array sensor emits an ultrasonic pulse, and each piezoelectric element of sensor receives the echo reflected from the surface of a particle. The exciting element emits a spherical ultrasonic wave. When adjacent elements emit within a close second, interference of wavefronts occurs as shown in **Figure 3.1 (a)**. **Figure 3.1 (b)** shows a schematic diagram of phased array sensor which a is element size, d is inter-element spacing, and c is element width. The pattern of the interference depends on the time delay, the steering angle of ultrasonic beam can be changed at the time delay Δt . The steering angle θ_s and the time delay Δt is related with the speed of sound in a medium c and inter-element spacing d as shown in Eq. (3.1).

$$\theta_s = \sin^{-1} \left[\frac{c\Delta t}{d} \right] \quad (3.1)$$

Basic equation of Doppler shift is derived from Doppler equation as shown below:

$$f_d = \frac{2 * s * f_0}{c} \quad (3.2)$$

where f_d is the Doppler frequency, s is the speed at which object is approaching the transducer, f_0 is the basic frequency of the transducer, and c is the speed of sound in the medium, i.e., water ($c = 1480$ m/s at 20 °C).

If the object is moving at an angle θ to the transducer, then $s = V * \cos \theta$. By substitution, we get the Doppler shift equation for a single transducer:

$$f_d = \frac{2 * f_0 * V * \cos \theta}{c} \quad (3.3)$$

Equation 3 can be rewritten as:

$$f_d = \left(\frac{f_0 * V}{c} \right) * 2 * \cos \theta \quad (3.4)$$

where $2 * \cos \theta$ applies to a roundtrip Doppler shift using a single transducer.

If two transducers are used, one receiver and one transmitter, as shown in **Figure 3.2**. Then, $2 * \cos \theta$ becomes $\cos \theta + \cos \gamma$, where θ is the angle between the transmitter

and the vector V , and γ is the angle between the receiver and the vector V . Moreover, $\alpha = \theta - \gamma$, where α is the angle between the transmitter and receiver, then $\cos \gamma = \cos(\theta - \alpha)$.

The Doppler equation becomes:

$$f_d = \left(\frac{f_0 * V}{c} \right) * [\cos \theta + \cos(\theta - \alpha)] \quad (3.5)$$

Using the trigonometric identity:

$$\cos(\theta - \alpha) = \cos \theta * \cos \alpha + \sin \theta * \sin \alpha \quad (3.6)$$

The Doppler Eq. (5) becomes:

$$f_d = \left(\frac{f_0 * V}{c} \right) * [\cos \theta + \cos \theta * \cos \alpha + \sin \theta * \sin \alpha] \quad (3.7)$$

In this paper, phased array sensor is used as transmitter and receiver (transceiver). As shown in **Figure 3.3**, the number of piezoelectric elements is eight elements. These eight elements transceiver transmit ultrasound beam at the same time or delayed for certain time to get steering angle, then the beams from these transceivers will interference pattern forming (beamforming) into one beam.

For measuring two-dimensional velocity vector, the development system uses two piezoelectric elements as transceivers to calculate the actual velocity magnitude and angle from the returned signal at specific measuring volume, i.e., Channel 4 (Ch 4). The Doppler shift equation for the piezoelectric element number 8 is identical to Eq (3.7):

$$f_{d8} = \left(\frac{f_0 * V}{c} \right) * [\cos \theta + \cos \theta * \cos \alpha + \sin \theta * \sin \alpha] \quad (3.8)$$

where f_{d8} is the Doppler frequency received by the piezoelectric element number 8 at angle α (measured clockwise from the axis of the transmitting beam), f_0 is basic frequency, V is the magnitude of the velocity of the particle travelling at angle θ

(measured clockwise from the axis of the transmitting beam), and c is the speed of sound in fluid i.e water.

The Doppler shift equation for the piezoelectric element number 1 is:

$$f_{d1} = \left(\frac{f_0 * V}{c} \right) * [\cos \theta + \cos \theta * \cos \alpha + \sin \theta * \sin \alpha] \quad (3.9)$$

where f_{d1} is the Doppler frequency received by the piezoelectric element number 1 at angle β (measured clockwise from the axis of the transmitting beam), and all other terms are identical to those of the piezoelectric element number 8.

The signals from both of these transceivers are demodulated with the transmitted frequency f_0 to produce four quadrature signals. It should be noted that at a given depth (channel) from the surface of both piezoelectric elements f_0 , c , α , and β are all-constant due to the fixed geometry of the piezoelectric elements. The real velocity vector V is calculated by multiplying the four-quadrature signals from the two transceivers elements number 1 and 8. The multiplying produces two subcomponents, which are the sum of the frequencies and the difference between the frequencies. Using trigonometry:

$$\cos f_{d1} * \cos f_{d8} = \frac{1}{2} [\cos(f_{d1} + f_{d8}) + \cos(f_{d1} - f_{d8})] \quad (3.10)$$

From Eq. (3.8) and Eq. (3.9), we will get the equations for the sum and difference as follow:

$$f_{d1} + f_{d8} = \frac{f_0 * V}{c} \left[\begin{array}{l} \cos \theta + \cos \theta * \cos \beta + \sin \theta * \sin \beta + \\ \cos \theta + \cos \theta * \cos \alpha + \sin \theta * \sin \alpha \end{array} \right] \quad (3.11)$$

If $\sin \beta = -\sin \alpha$ and $\cos \beta = \cos \alpha$, then Eq. (11) becomes

$$f_{d1} + f_{d8} = \frac{f_0 * V}{c} \left[\begin{array}{l} \cos \theta + \cos \theta * \cos \beta + \sin \theta * \sin \beta + \\ \cos \theta + \cos \theta * \cos \alpha + \sin \theta * \sin \alpha \end{array} \right] \quad (3.12)$$

$$f_{d1} + f_{d8} = \frac{f_0 * V}{c} [2 * \cos \theta (1 + \cos \theta)]$$

$$f_{d1} + f_{d8} = \frac{2 * f_0}{c} (1 + \cos \theta) * V * \cos \theta$$

$$f_{d1} - f_{d8} = \frac{f_0 * V}{c} \left[\begin{array}{l} \cos \theta + \cos \theta * \cos \beta + \sin \theta * \sin \beta - \\ \cos \theta - \cos \theta * \cos \alpha - \sin \theta * \sin \alpha \end{array} \right] \quad (3.13)$$

If $\sin \beta = -\sin \alpha$ and $\cos \beta = \cos \alpha$, then Eq. (13) becomes

$$f_{d1} - f_{d8} = \frac{f_0 * V}{c} \left[\begin{array}{l} \cos \theta + \cos \theta * \cos \beta + \sin \theta * \sin \beta - \\ \cos \theta - \cos \theta * \cos \alpha - \sin \theta * \sin \alpha \end{array} \right] \quad (3.14)$$

$$f_{d1} - f_{d8} = \frac{f_0 * V}{c} [-2 * \sin \theta * \sin \alpha]$$

$$f_{d1} - f_{d8} = -\frac{2 * f_0}{c} * \sin \alpha * V * \sin \theta$$

If $V_x = V * \sin \theta$ and $V_y = V * \cos \theta$, then from Eq. (12) and (14):

$$V_x = -\frac{(f_{d1} - f_{d8})}{2 * f_0} \frac{c}{\sin \alpha} \quad (3.15)$$

$$V_y = \frac{(f_{d1} + f_{d8})}{2 * f_0} \frac{c}{(1 + \cos \alpha)} \quad (3.16)$$

Since these V_x and V_y are orthogonal, the real magnitude can be determined by vector addition, and simple trigonometry can determine the angle:

$$V = \sqrt{V_x^2 + V_y^2} \quad (3.17)$$

$$\delta = \tan^{-1} \left(\frac{V_y}{V_x} \right) \quad (3.18)$$

The spatial resolution or channel distance is defined as:

$$\Delta y = \frac{N_{cycle}}{2 * f_0} * c \quad (3.19)$$

where Δy is channel distance, N_{cycle} is a number of cycles per pulse, c is the speed of sound, and f_0 is the basic frequency of the transducer. If $N_{cycle} = 2$, $c = 1480$ m/s, and $f_0 = 2$ MHz, then channel distance (Δy) is 0.74 mm.

Phased Array UVP system is showed in **Figure 3.4**. National Instrument LabVIEW program is used to control Phased Array UVP system and reconstruct two-dimensional velocity vector. The measurement system consists of a 2 MHz phased

array sensor with eight piezoelectric elements, 8-channel pulse receiver, analog to digital converter and personal computer to control the pulse receiver and analyze echo signal from the digitizer.

3.3 Near-field effect by Phased Array sensor

In Phased Array UVP system, we have to consider the effect of the near field oscillation. The high oscillation burst occurs near the active elements surface. It influences the accuracy of the measurement close to the sensor (near-field region). The near-field boundary of phased array sensor has been numerically investigated as shown in **Figure 3.5**. The numerical calculation is based on the work by Ocheltree and Frizzel [3.6] and performed using MATLAB®. Near-field oscillation boundary depends on the width of piezoelectric element b and the wavelength of the ultrasound pulse λ . From Eq. (3.20), we can estimate near-field oscillation length $N_{oscillation}$ of phased array sensor.

$$N_{oscillation} = \frac{k_a b^2}{8\lambda} \quad (3.20)$$

where, k_a is correction factor, and b is piezoelectric total element width. The correction factor can be calculated from the rectangular element ratio $(b/c) = 1$ as shown in **Figure 3.6**. From the calculation, the near-field oscillation boundary is 5.78 mm from the element surface. Hamdani *et al.* [3-13] confirmed the near-field effect on the velocity measurement. Velocity data on the near-field region showed a bad accuracy. Nevertheless, the velocity data beyond the near field showed a good agreement with conventional UVP, and they confirmed that the angle uncertainty for two-dimensional velocity was $\pm 1^\circ$.

3.4 Experimental setup

The experiment was conducted in a water circulation system, which consisting of the cooling system to keep constant temperature. The water temperature is keep in 25 °C for sound speed $c = 1480$ m/s. The inner diameter of the pipe is 50 mm and made of acrylic. The distance from the inlet to double bend is $40D$ ($D = 50$ mm). In that position, the fluid is in the fully developed turbulent pipe flow condition as shown in **Figure 3.7**. The double bent pipe is utilized to investigate the recirculating flow. The double bent pipe has a bent angle of 90 degrees and curvature radius $R_c = 25$ mm. The schematic view of the measurement position is shown in **Figure 3.8**.

For this experiment, we measured in the axial plane at $x/D = 1$ and $x/D = 1.5$ from the downstream of the second elbow to observe the flow acceleration phenomenon of recirculating flow in the reattachment point region. The water flows in the turbulent flow condition at Reynolds number ($Re = 10,000$). The time transient temperature data is recorded using thermocouple during the measurements. **Table 3.1** and **3.2** show the experimental and measurement system conditions

A phased array sensor, which has basic frequency 2 MHz, is installed through the pipe wall. Thus, there is a direct contact between sensor and fluid to overcome the refraction in pipe wall and fluid medium. The number of cycle in an ultrasound pulse is $n_{cycle} = 2$ and the spatial resolution is 0.74 mm.

3.5 PIV measurement setup

Particle Image Velocimetry (PIV) method is applied in this experiment to compare the results of Phased Array UVP. PIV system consisted of a laser (DANTEC DYNAMICS), High-Speed Camera (FastCam SA5). The camera is located at the top of the measurement region, and the laser beam emits from the side of the pipe through the pipe center to measure the axial plane of the fluid. PIV measurement section and the detail view of measurement section are shown in **Figure 3.9** and **Figure 3.10**. The picture of measurement system is shown in **Figure 3.11** and **Figure 3.12**. In PIV

method, High-Speed Camera captures the images of nylon tracer particles lightened by the laser sheet in working fluid. The total number of frames per one record was 5250, and the camera captured 750 frames per second. The image sizes are 110 mm \times 110 mm (1024 pixel \times 1024 pixel). The data from the images analysis in PIV Lab application by using MATLAB program. The reference region is 200 pixel \times 24 pixels. Two-dimensional velocities are obtained by averaging 5250 subsequent images of the particles motion.

3.5 Results and discussions

Figure 3.13 shows two-dimensional velocity vector from PIV measurement. The measurement area starts from $x/D = 0.6$ to $x/D = 1.55$. The flow distortion and recirculation flow occur downstream region of double bend pipe outlet. Therefore, two different flow patterns ($y/D = 0.2$ to $y/D = 0.6$) and ($y/D = 0.7$ to $y/D = 0.9$) can be recognized in the flow field. We can assume that the recirculating flow region is located from the sharp bend curvature to $x/D = 1$ according to the direction of the velocity vector. The forward flow starts around $x/D = 1$ and continues to the downstream region.

Figure 3.14 shows two-dimensional velocity vector from Phased Array UVP measurement at $x/D = 1$ and $x/D = 1.5$ downstream of the double bend pipe. In each measurement position, we measured three measurement lines, and the interval between each measurement lines is 5 degree. The vector field cannot be measured near the oscillation boundary of the phased array sensor. In the experiment, the near-field oscillation boundary is observed from $y/D = 0$ to $y/D = 0.08$. The ten thousand instantaneous velocity vectors are averaged in each measurement line because, in the turbulent flow condition, the velocity fluctuation is very high downstream of the double bend pipe. In the position of $x/D = 1$, velocity vectors in the first two measurements are reversed flow direction at the bottom part of measurement lines, and the main flow region is located from $y/D = 0$ to $y/D = 0.8$. We can observe the reattachment point at zero degree perpendicular measurement line of $x/D = 1$. It

means that the forward flow starts from that measurement line and at $x/D = 1.5$ the reverse flow is disappeared but the flow pattern is still asymmetric.

Two measurement results are compared in **Figure 3.15**. The black velocity vector is from Phased Array UVP, and the red velocity vector is from PIV. To compare the measurements result, the velocity vector in PIV results are selected at the same spatial resolution and same measurement line as Phased Array UVP velocity vector. In PIV measurement result, the velocity vector cannot be analyzed close to the pipe boundary from $y/D = 0$ to $y/D = 0.16$ because of pipe curvature effect and the reflection of laser sheet. In the main flow area, flow pattern are same in both case, but the velocity magnitude in PIV is a bit larger than Phased Array UVP. However, it is not much different if we compare in one-dimensional case. In the recirculating flow region, the reverse flow pattern can be seen in Phased Array UVP result. In PIV results, the reverse flow vector field is not totally reverse. However, we can assume that the recirculation flow region is located from the elbow end to $x/D = 1$. The quantitative comparison between Phased Array UVP and PIV was shown in **Figure 3.16**.

Velocity fluctuation is analyzed from instantaneous velocity vector from Phased Array UVP measurement at the perpendicular 0 degree measurement line in $x/D = 1$ and $x/D = 1.5$ positions. **Figure 3.17** shows the root mean square (RMS) value of axial velocity (U_{rms}) and radial velocity (V_{rms}). RMS value of axial and radial velocity is important to analyze the velocity fluctuation in the turbulent flow. From U_{rms} analyzed graph, the axial velocity fluctuation at the position $x/D = 1$ is very high between $y/D = 0.6$ and $y/D = 0.8$ (see in Fig.12 (a)). However, the axial velocity fluctuation at the position $x/D = 1.5$ is almost stable compare with $x/D = 1$. It means that the high velocity fluctuation occurs at the boundary of the main flow and recirculating flow. In Fig. 12 (b), the radial velocity fluctuation is high at the center of the pipe. When the fluid enters the elbow and touches the curved wall, the flow direction changes and the circular flow well-known as the secondary flow in the bent pipe occurs. Therefore, at the core of the flow (near the pipe center), the high radial velocity fluctuation is induced in $x/D = 1$ and $x/D = 1.5$.

3.6 Conclusions

In order to understand the velocity distribution of turbulent flow just downstream of the double bent pipe outlet, the measurement of the two-dimensional velocity vector is carried out by Phased Array UVP system and PIV. The flow distortion and recirculating flow occur in the measurement region downstream of the double bend pipe. From both measurement results, the recirculating flow region was observed and the reattachment point occurs around $x/D = 1$. In the velocity fluctuation analysis, the axial velocity fluctuation apparently occurs at the boundary of the main flow and the recirculating flow. The radial velocity fluctuation occurs at the center of the pipe.

References

- [3-1] Hoekstra, A. J., Derksen, J. J., & Van Den Akker, H. E. A.: An experimental and numerical study of turbulent swirling flow in gas cyclones, *Chemical Engineering Science*, **54**(13-14), (1999), 2055-2065.
- [3-2] Susan-Resiga, R., Ciocan, G. D., Anton, I., & Avellan, F.: Analysis of the swirling flow downstream a Francis turbine runner, *Journal of Fluids Engineering*, **128**–1, (2006), 177-189.
- [3-3] McClusky, H. L., Holloway, M. V., Beasley, D. E., & Conner, M. E.: Development of swirling flow in a rod bundle subchannel, *Journal of Fluids Engineering*, **124**–3, (2002), 747-755.
- [3-4] Takano, T., Ikarashi, Y., Uchiyama, K., Yamagata, T. & Fujisawa, N.: Influence of swirling flow on mass and momentum transfer downstream of a pipe with elbow and orifice, *International Journal of Heat and Mass Transfer*, **92**,(2016), 394-402.
- [3-5] British Standards EN12668-2 Non-destructive testing: Characterization and verification of ultrasonic examination equipment, Part 2-Probes, (2008), 47-48.

Table 3.1 Experimental condition

Parameters	Value
Reynolds numbers [-]	10000
Fluid (water) temperature [°C]	25 ± 1
The radius of elbow curvature [mm]	25
Pipe diameter [mm]	50
Proximity between two elbows [mm]	300

Table 3.2 Experimental condition of Phased Array measurement

Parameters	Value
Frequency of Phased array sensor [MHz]	2
Number of cycle in a pulse [-]	2
Spatial resolution [mm]	0.74
Steering angle [degree]	-10°, -5°, 0°
Pulse repetition frequency [kHz]	1
Number of repetition [-]	128
Time resolution [s]	0.128
Number of velocity profiles	10,000

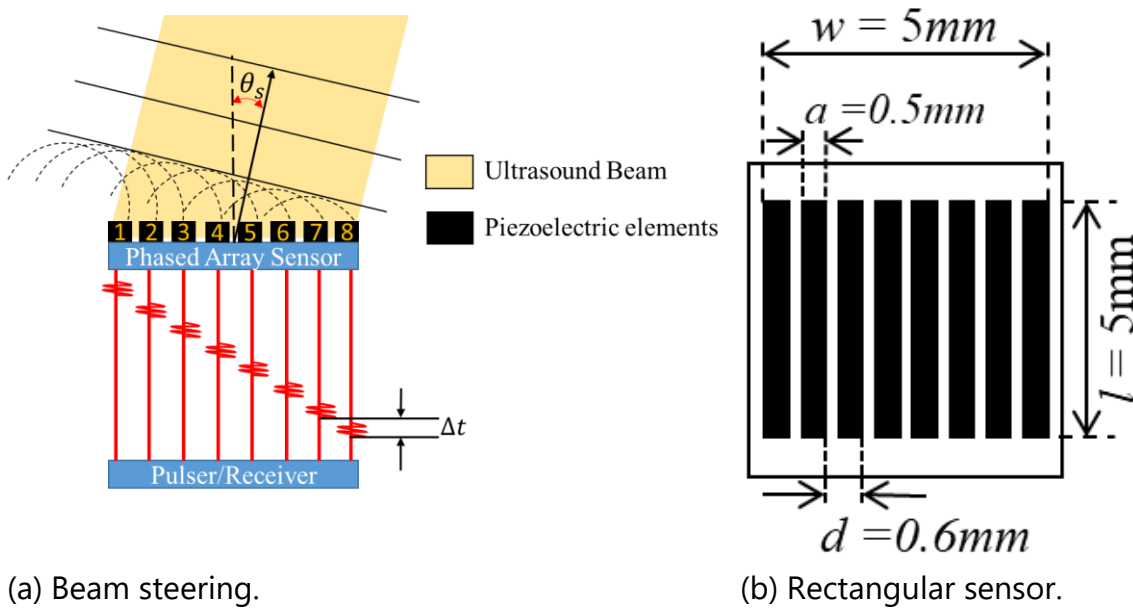


Figure 3.1. Beam steering principle of Phased Array sensor and its schematic diagram.

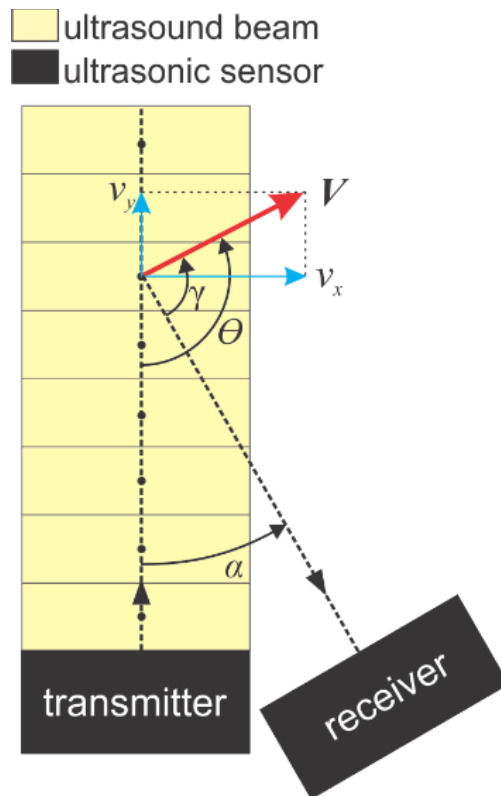


Figure 3.2. A two-transducer ultrasound system produces a Doppler signal from velocity vector V .

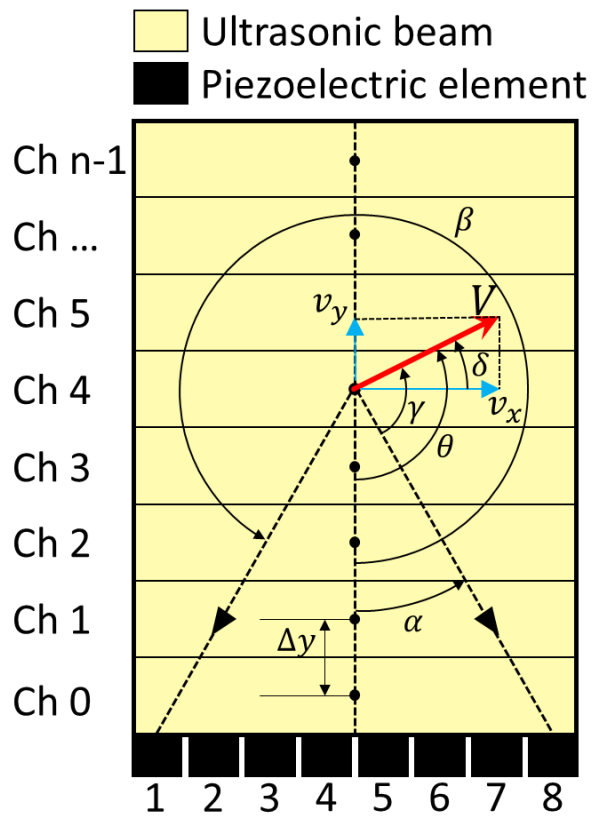


Figure 3.3. Velocity vector reconstruction.

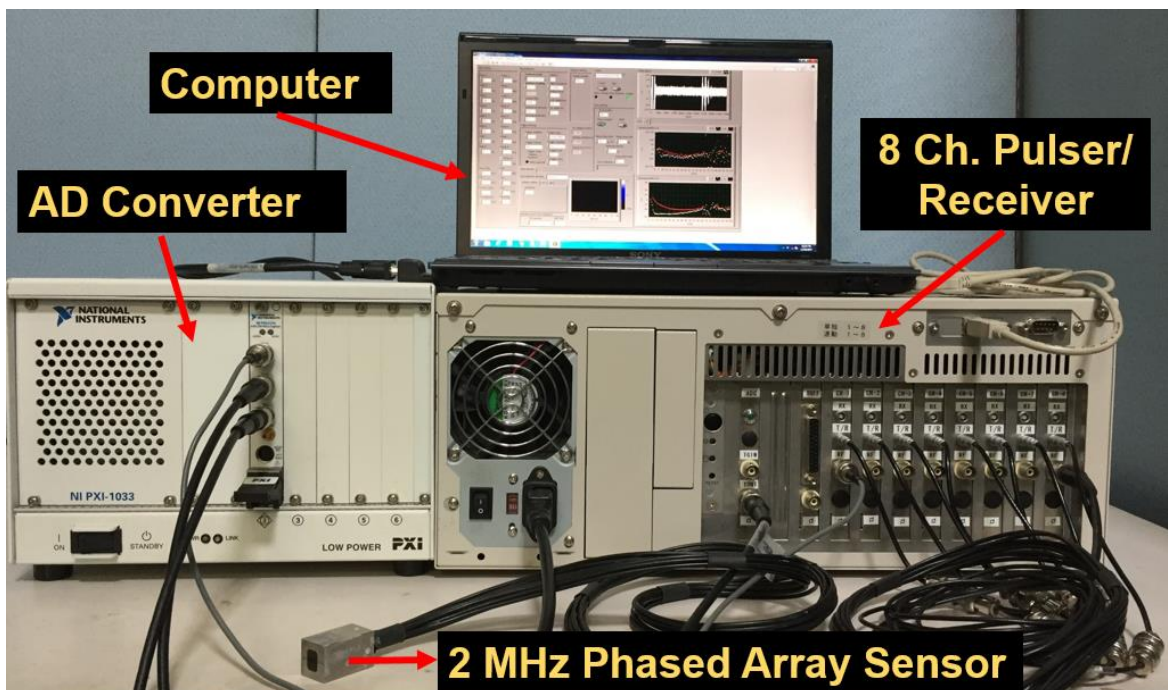


Figure 3.4. Phased array UVP measurement system.

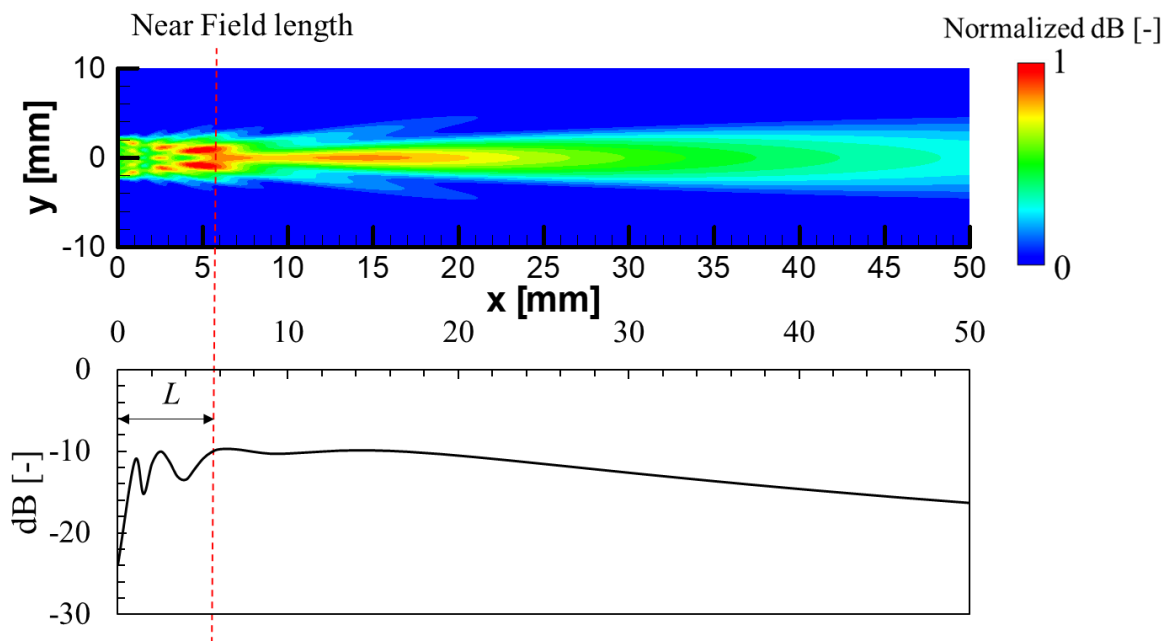


Figure 3.5. Near-field length of sound pressure.

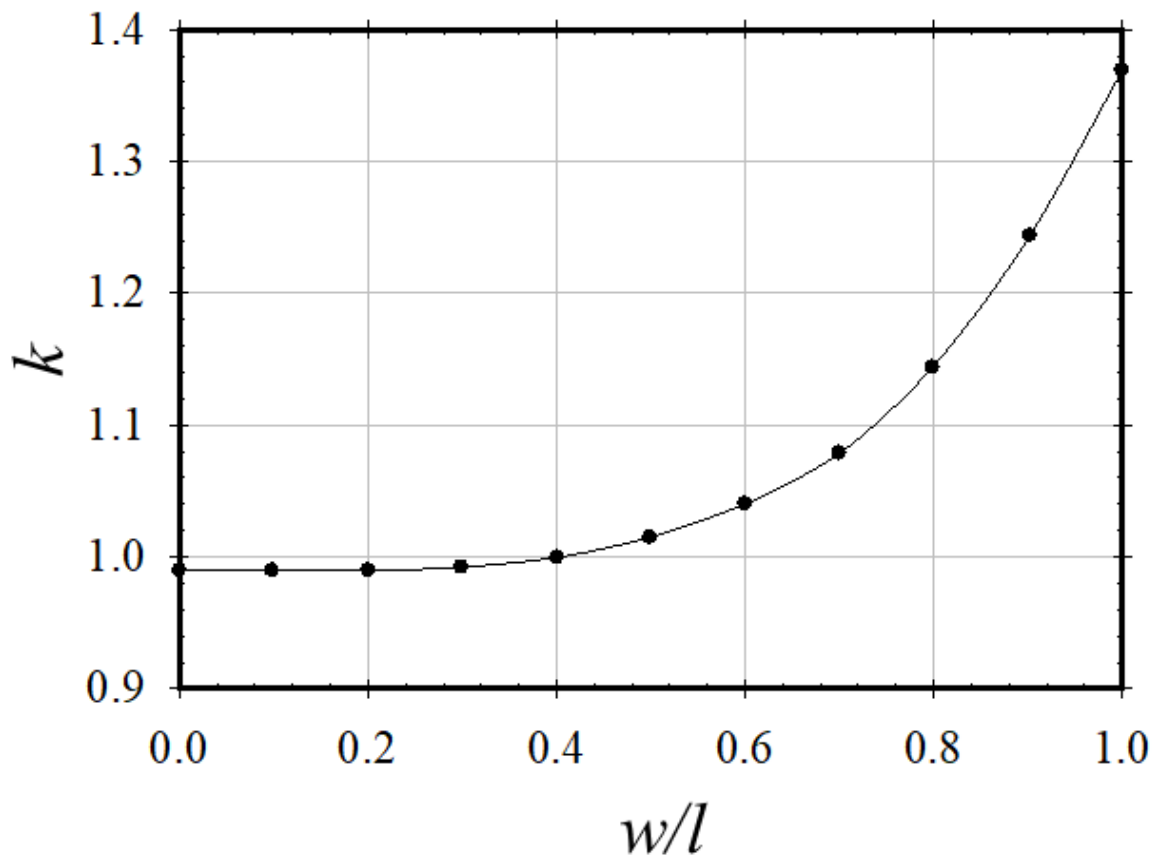


Figure 3.6. Correction factor of the rectangular sensor.

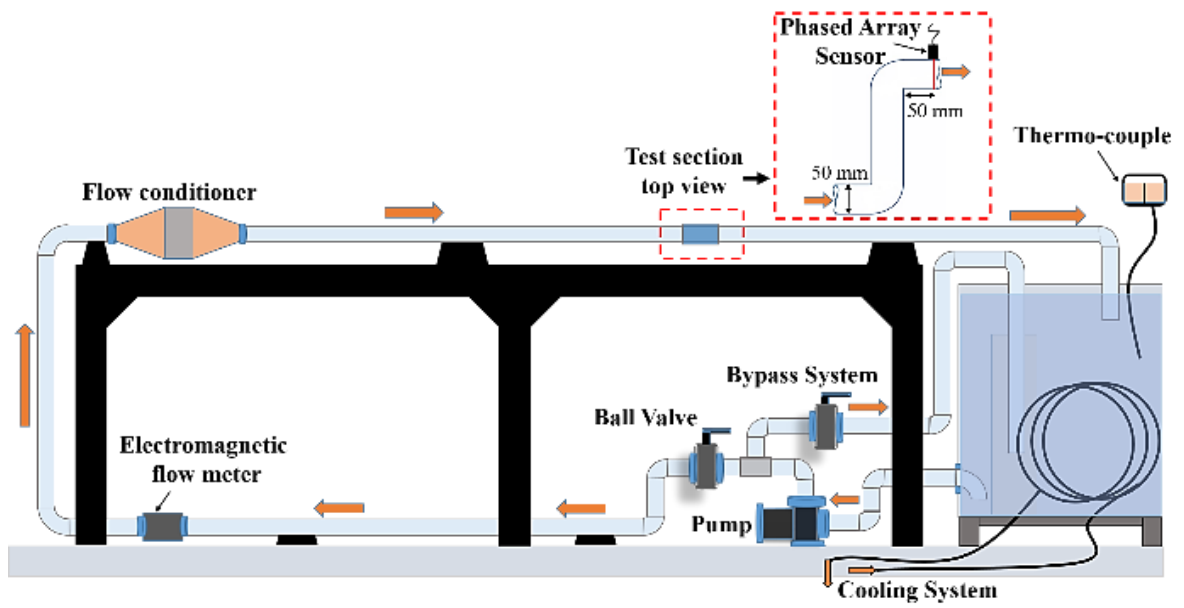


Figure 3.7. Experimental facilities of a piping system.

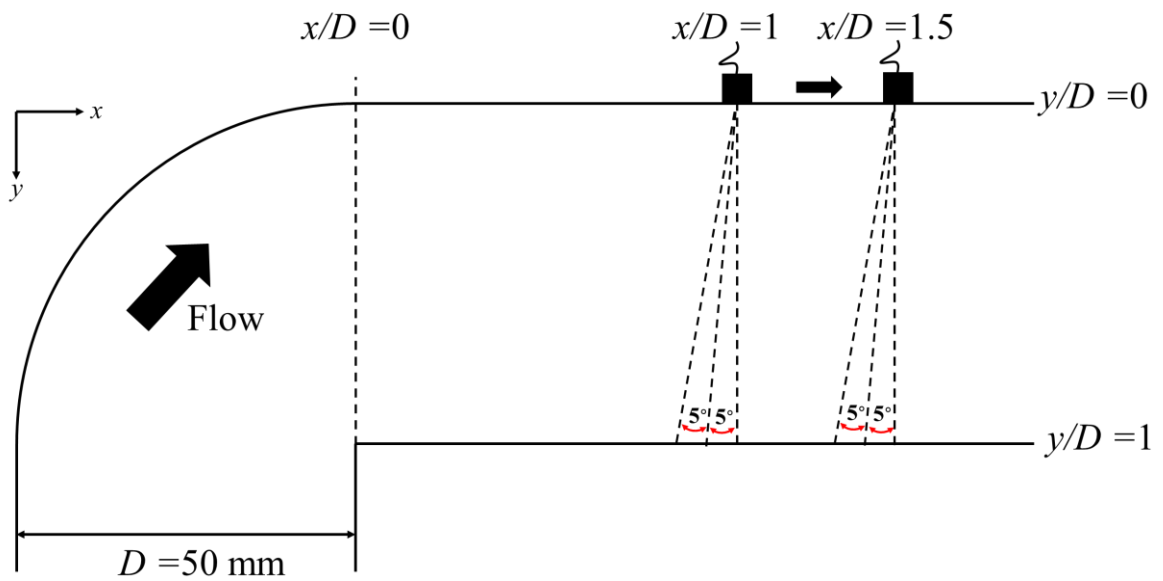


Figure 3.8. Detail view of measurement position.

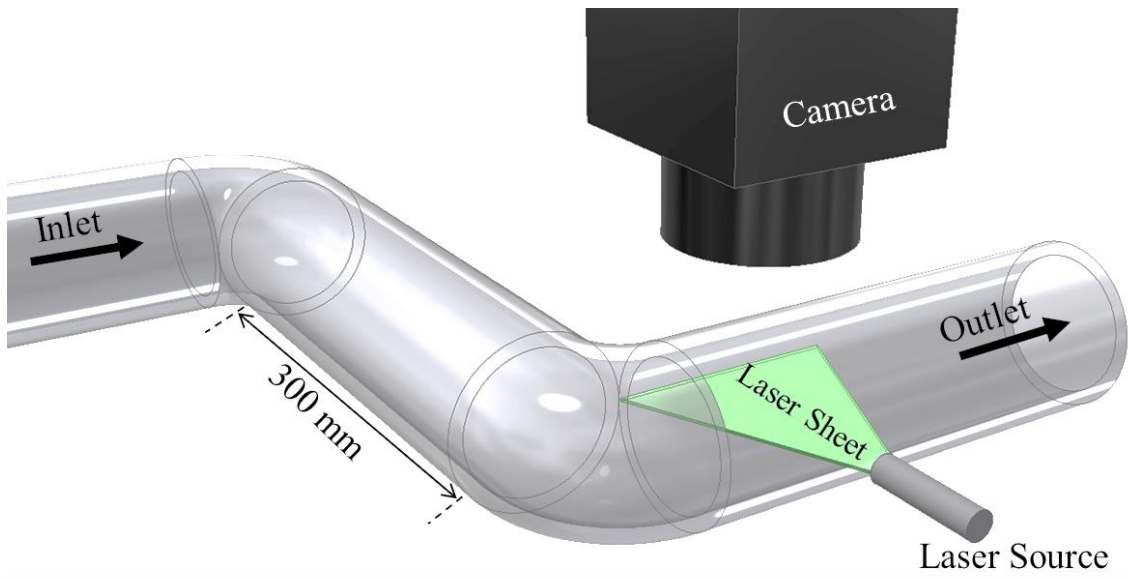


Figure 3.9. PIV measurement position.

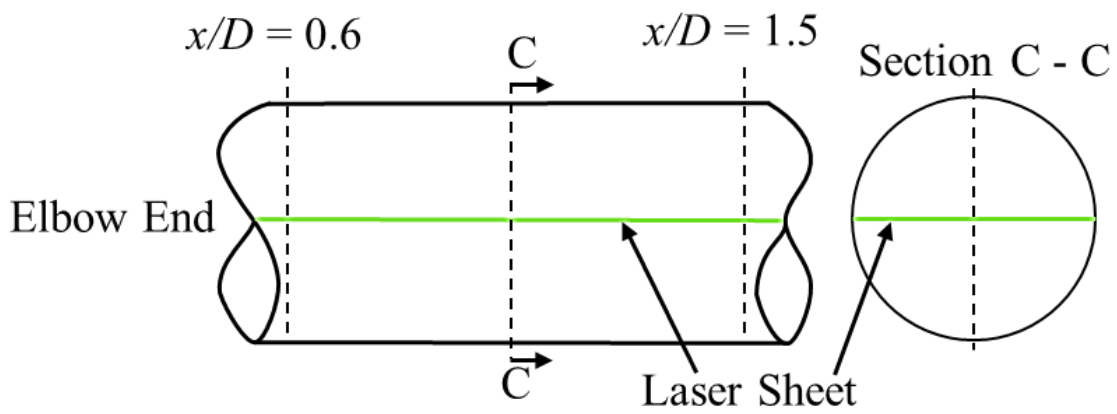


Figure 3.10. Detail view of PIV test section.

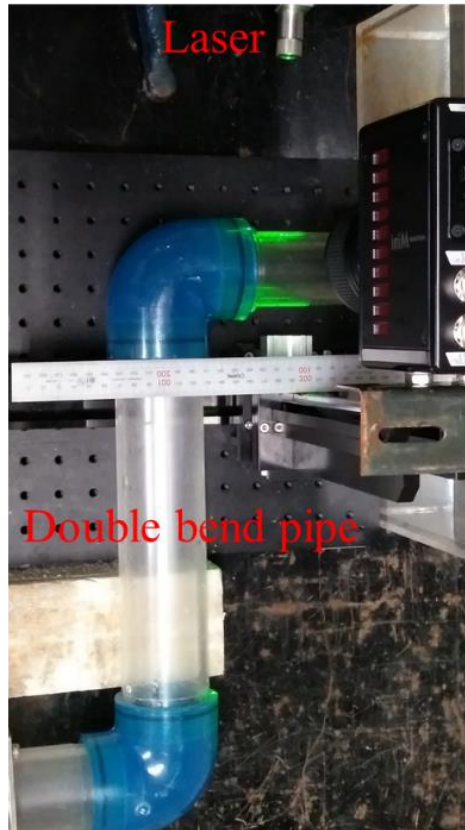


Figure 3.11 Top view picture of the test section.

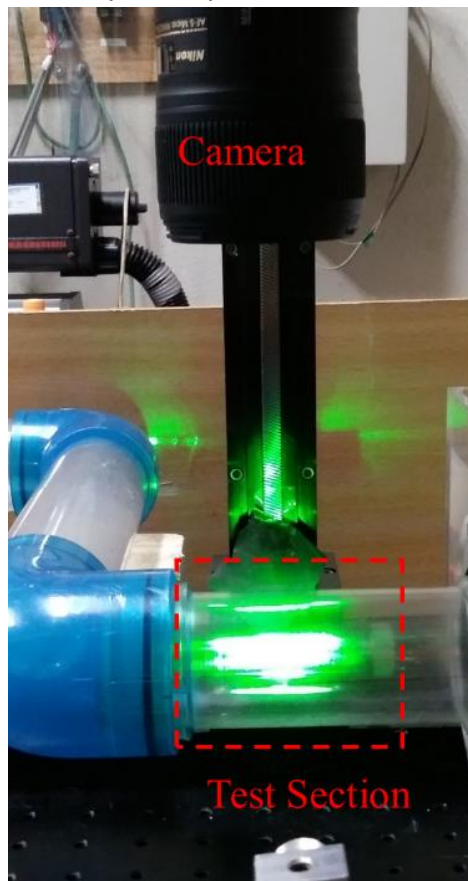


Figure 3.12 Side view picture of the test section.

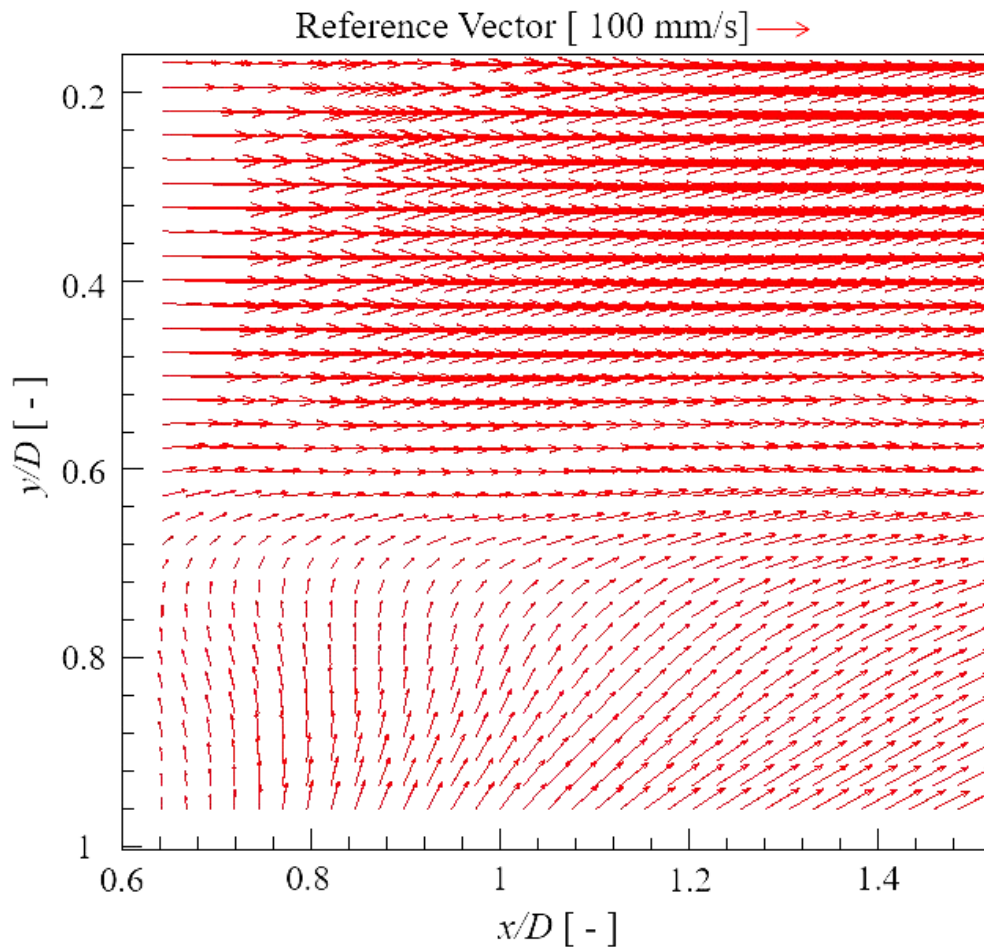


Figure 3.13 Average velocity vector from PIV measurement.

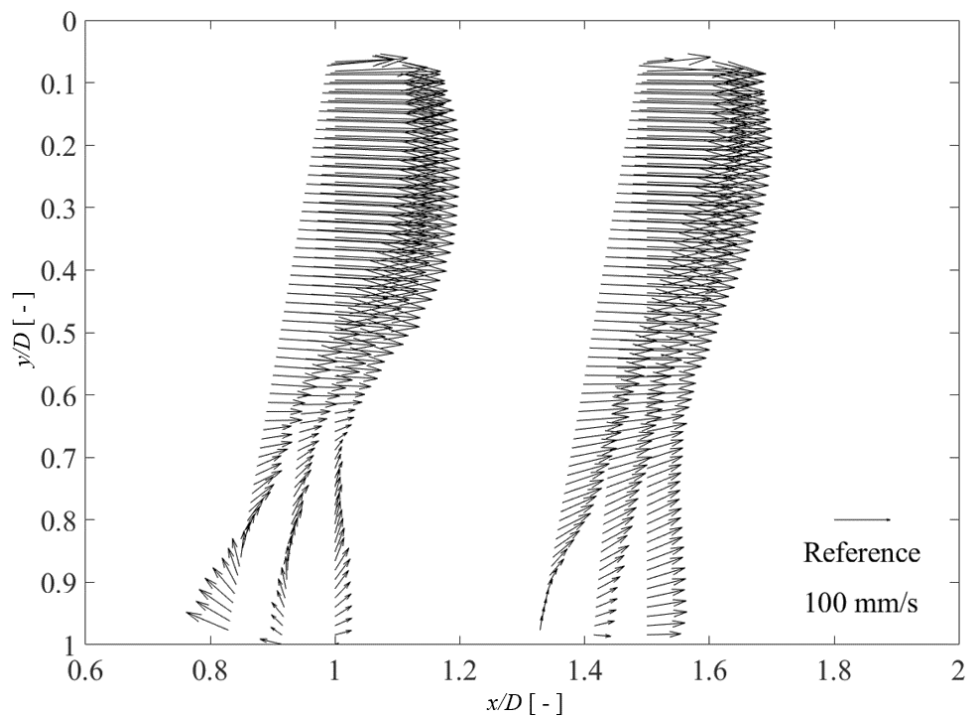


Figure 3.14 Average velocity vector from Phased Array UVP measurement.

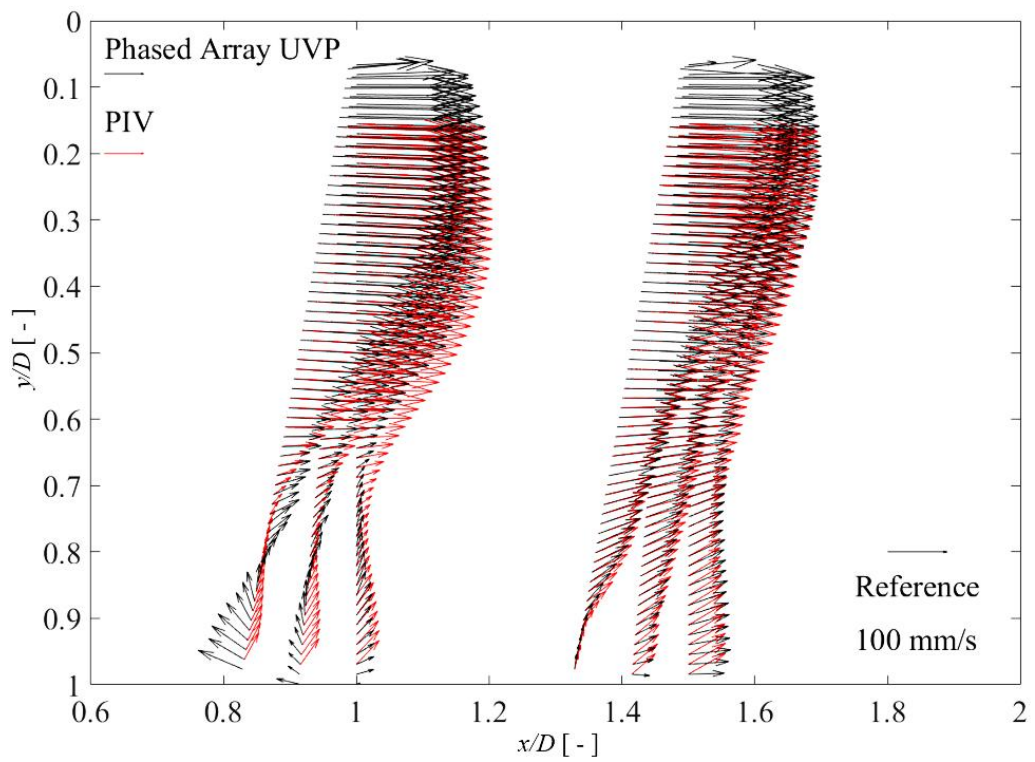


Figure 3.15 Phased Array UVP and PIV measurement results in two-dimensional vector.

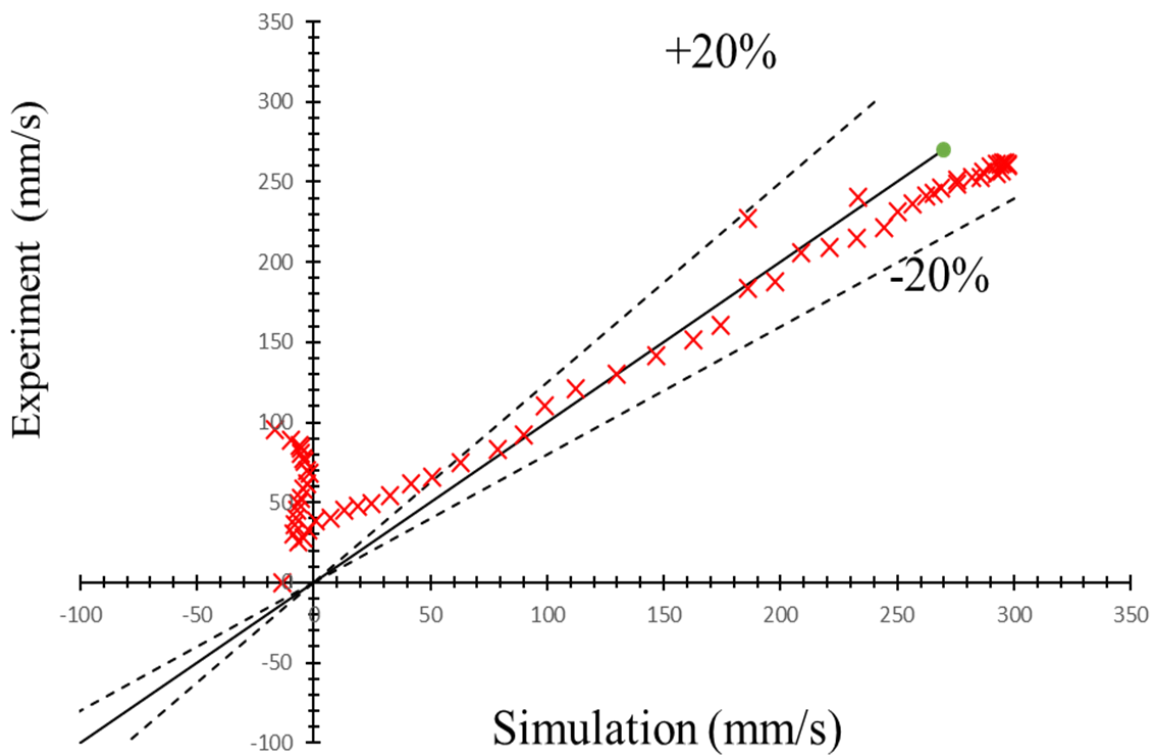
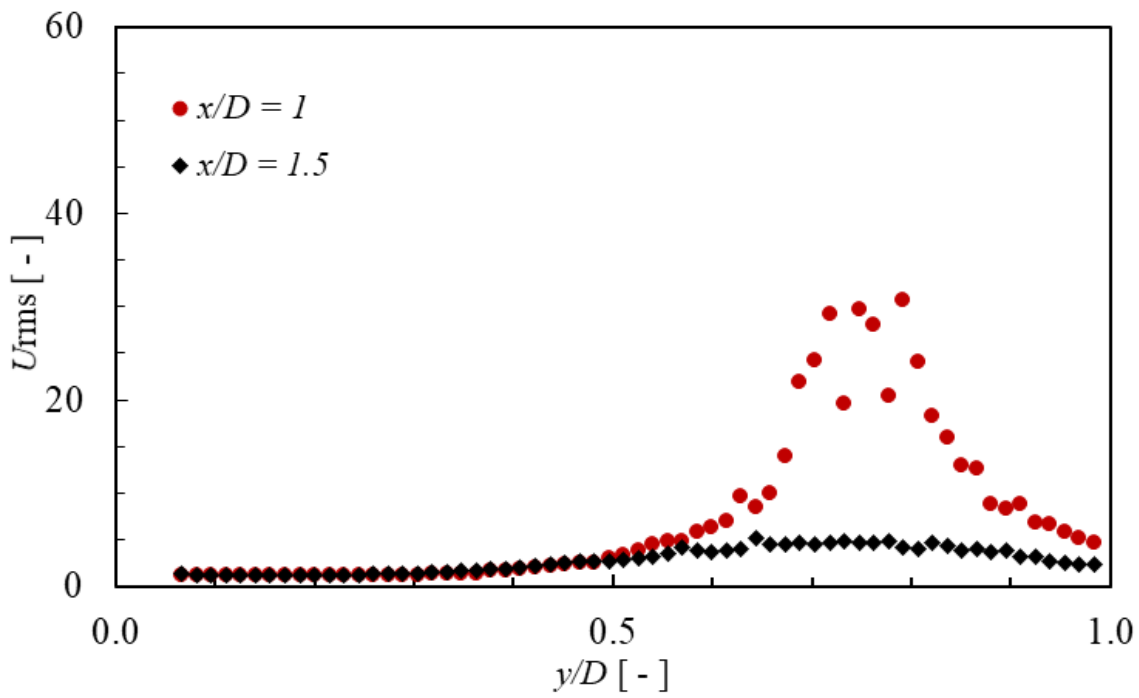
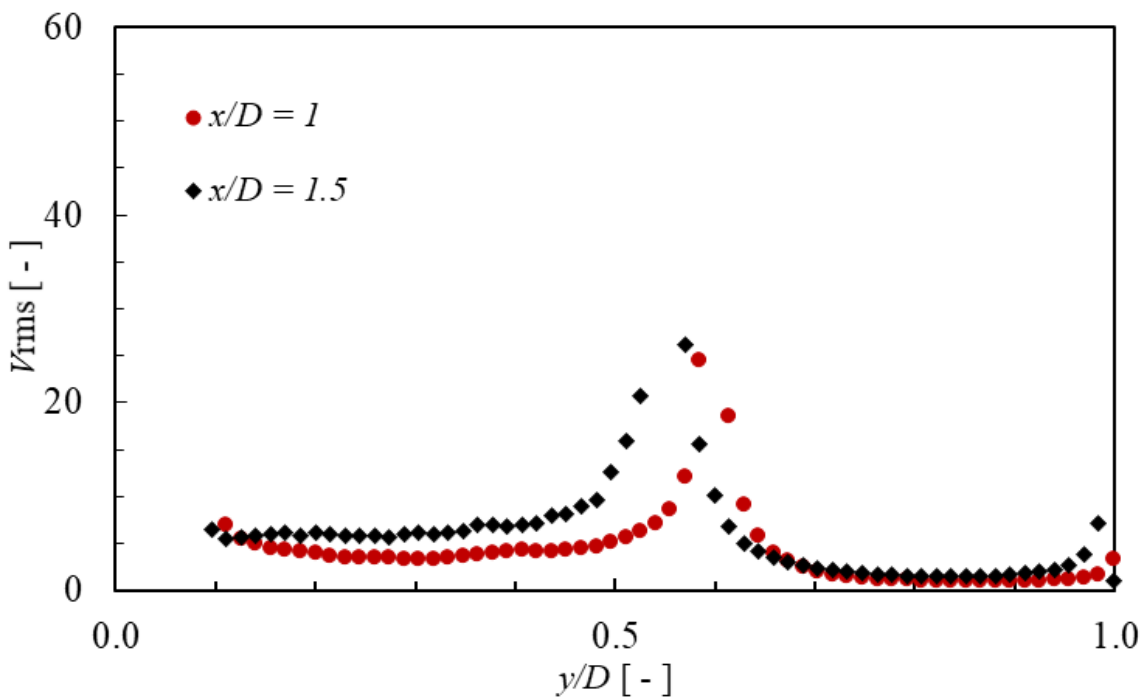


Figure 3.16 Quantitative comparison between Phased Array UVP and PIV.



(a) Root mean square of axial velocity.



(b) Root mean square of radial velocity.

Figure 3.17 Velocity fluctuation analysis from Phased Array UVP measurement.

Chapter 4

Influence of Inlet Swirling Flow on Flow Structure and Velocity Fluctuation

4.1 Introduction

Pipeline systems in many industries and power plants are usually characterized by its layout complexity, which consists of many main long straight pipes and secondary pipes connected by sharp bends. In nuclear power plants, the flow downstream of a 90° bend is essential for the primary and secondary cooling systems, where many sharp bends are used to interconnect the components. However, fluid flows through a 90° sharp bends are a very complex phenomenon. As the fluid flows through a bend, the centrifugal force acting on the fluid develops a radial pressure gradient. Because of the pressure gradient in the fluid, the secondary flow is generated downstream of the bend. In addition, a significant pressure gradient produces swirling flow downstream the bend pipe [4-1]. Under the swirling flow condition, the significant pressure fluctuation and the high-velocity fluctuation occur in the bends. These are sources of flow-induced vibration (FIV). Consequently, FIV can cause the fatigue fracture in a piping system of the industries and power plants [4-2]. Therefore, the investigation of fluid flow field and velocity fluctuation are essential issues for the pipeline safety.

The structure of the secondary flow in the bends is dependent on the bend curvature radius (R_c) and Reynolds number (Re). Some researchers have investigated the flow characteristics in the 90° single bend pipe flow with curvature ratio of $R_c/D > 1.3$ (R_c : curvature radius, D : pipe diameter) both experimentally and numerically [4-3, 4-6]. When the non-dimensional curvature ratio of the bend is greater than 1.5, the secondary flow which consisting of a pair of counter-rotating vortices (Dean vortices) are generated. Meanwhile, the velocity profile of the primary stream wise flow is distorted and shifted away from the center of the curvature of the elbow [4-7]. For the small curvature ratio, Kawamura *et al.* [4-8] studied the flow separation using the bends with curvature ratio of $R_c/D = 1.1, 2, 4$. The experiments were done by using Laser Doppler Velocimetry (LDV) at Reynolds numbers of $5 \times 10^4 < Re < 1 \times 10^5$. They revealed that the flow separation occurred at $R_c/D = 1$ and did not occur at $R_c/D = 2$ and $R_c/D = 4$. Also, they found that the power spectrum of the turbulence

intensity downstream near the elbow with any curvature ratio and Reynolds number had a distinct peak at the reduced frequency of about 0.5. Later on, Ono *et al.* [3-6] investigated the water experiments in two bends with different curvature ratio ($R_c/D = 1$ and $R_c/D = 1.5$) in order to investigate the interaction between flow separation and the secondary flow due to the elbow curvature. Particle Image Velocimetry (PIV) was used in their experiment, and they confirmed that the flow separation always occurred in the short-elbow ($R_c/D = 1$) while the flow separation occurred intermittently in the long-elbow case ($R_c/D = 1.5$).

The experiments on the above previous studies mainly were conducted under the inlet condition of fully developed flow and flat velocity profile. However, non-uniform velocity profile on the inlet condition might be appeared in a specific condition. Kubo *et al.* [4-9] confirmed that a swirling flow occurred in the dual elbow. The experiments were done by two-dimensional Particle Image Velocimetry (2D-PIV) at Reynolds number $Re = 3 \times 10^5$ with three types of curvature ratio $R_c/D = 1, 1.5, 2$. They found that the swirl intensity of the swirling flow, which was generated in the dual elbow, became high and fluctuated largely as the curvature ratio was small. The influence of inlet swirling flow on 90° bend pipe was studied in order to understand the flow structure downstream the bend pipe flow. Sudo *et al.* [4-10] measured the pressure and velocity distribution at $Re = 6 \times 10^4$ with a curvature ratio of $R_c/D = 2$ under the weak inlet swirling flow condition. They found that inlet swirl flow affected the behavior of secondary flow generating at the downstream of the bend pipe flow. Later, Kalpakli and Orlu [4-11] experimentally studied the influence of swirling intensity at the inlet on the 90° bend pipe flow. The investigation was done using stereoscopic particle image velocimetry. When the swirl number was increased to $S = 1.2$, it was found that the Dean vortices at the downstream of bend pipe became a single large-scale motion located almost at the center of the pipe and flow became a dominated swirl flow. Swirling inlet flow condition is also encountered in the cold-leg piping system in a nuclear reactor. Therefore, Yamano *et al.* [1-11, 1-16] investigated the effect of swirl flow at the inlet on the 90° double bend pipe both experimentally and numerically, to evaluate the flow-induced vibration for primary

cooling pipes in the Japan sodium-cooled fast reactor (JSFR). The experiment was done by PIV method with curvature ratio $R_c/D = 1$. They found that the flow separation region was deflected at the downstream from the bend when the inlet condition on the first bend was swirling flow. Later, Mizutani *et al.* [1-17] investigated the influence of inlet condition upstream the triple elbow. Particle Image Velocimetry (PIV) was used for the velocity flow mapping, and the tangential injection method was used to generate swirling flow on the inlet. The triple elbow with curvature ratio $R_c/D = 1$ was used to be close to an actual condition and to accumulate knowledge towards optimization of a prospective piping layout in the conceptual design of Japan Sodium Fast Reactor (JSFR) [1-18].

In the previous studies, the researchers mostly used the optical system to measure the velocity field and velocity fluctuation. However, the optical system has some challenges to apply in non-transparent wall channel or pipe. Also, it is difficult for the applications in actual plant process. Thus, another measurement technique should be developed to evaluate the velocity field and velocity fluctuation. In addition, the influence of the strong swirling inlet on the double bend with curvature ratio $R_c/D < 1$ has not been done yet. So in this study, the influence of the strong swirling inlet condition on the velocity fluctuation at the 90° double bend pipe with curvature ratio $R_c/D = 0.5$ is investigated with ultrasound technique. Ultrasound technique measurement is used because its advantages which can be applied in the non-transparent pipe and opaque liquid flow [1-20].

Initially, conventional Ultrasonic Velocity Profiler (UVP) method only measures one-dimensional velocity profile in the measurement line. In this study, a phased array sensor was utilized to measure instantaneous two-dimensional velocity profile. This chapter observes influence of inlet swirling flow on the flow structure and velocity fluctuation downstream of double bend pipe layout, which made by 90° double elbow with inlet swirling flow and without inlet swirling flow condition. Phased Array UVP measurement done in the case of with and without inlet swirling flow condition.

The main objective of this chapter is to clarify the reattachment point of secondary swirling flow that occurs just downstream of the double bend pipe and to observe the influence of strong swirling inlet flow on the velocity fluctuation of the 90° double bend pipe flow using ultrasound technique. The bend curvature caused the secondary swirling flow, and the high-velocity fluctuation occurs near the reattachment point region. To achieve this purpose, Phased Array UVP system is utilized to measure the two-dimensional velocity and the axial and tangential velocity fluctuation at the secondary flow region.

4.2 Experimental setup

The experiment was conducted in a horizontal water circulation system at atmospheric pressure, which consisting of the cooling system, electromagnetic flow meter, pump, ball valve, a bypass pipe, and flow conditioner as shown in **Figure 4.1**. Water is supplied to the test channel from the water storage tank by a 3phase induction motor pump (65×50FSED EBARA CORPORATION). The flow rate of the liquid phase is controlled using the control ball valve. The flow rate is measured by magnetic flow meter (MAGMAX MGC010 Tokyo Keiso Co., Ltd) with accuracy $\pm 0.5\%$. Fluid enters the straight pipe test section after an elbow. Therefore a flow conditioner is installed to eliminate the flow distortion effects of the elbow. The length of straight pipe before entering the first bend is $42D$ ($D = 50$ mm) in order to achieve fully developed turbulent pipe flow condition at the inlet of the first bend. In this experiment, the double bend pipe is utilized to investigate the secondary swirling flow. The double bent pipe has a bent angle of 90 degrees and curvature ratio $R_c/D = 0.5$. The Reynolds number is $Re = 1 \times 10^4$, based on the bulk velocity and the pipe diameter. The cooling system is used to control and maintain a constant water temperature. The temperature is recorded using thermocouple during the measurements, and it is confirmed that the water temperature fluctuation is $\pm 1^\circ\text{C}$.

4.2.1 The Swirling Generator

For the generation of swirling flow, some different methods exist (e.g., pipe rotation, tangential injection, guide-vane, twisted tape, helical turbulators, and propeller-type), which have a different effect on the main flow [4-12]. In this present study, we used the rotary swirler [4-13, 4-14]. The rotary swirler is used as swirl generator because it is easy to control the swirl intensity. The top view of the experimental set up with the swirling generator is shown in **Figure 4.2**.

The swirl generator is installed at 12D upstream of the double bent pipe. The rotary swirler consists of a 150 mm long aluminum pipe with inner diameter 50 mm. Small tubes of diameter 3 mm and 50 mm long are inserted into the aluminum pipe. The small tubes are packed as tightly as possible, and their number is approximately 95. The pipe can be rotated about its axis at speed varying from 15 to 1,100 r.p.m. by induction motor (5IK90SW-5 Oriental Motor Co., Ltd) and a timing belt (K40L50BF) connects it. With the pipe rotating, the growth of the boundary layer on the pipe walls establishes an azimuthal velocity distribution corresponding to the solid-body rotation in the core. Whereas the rotary swirler allows the solid rotation of the small tubes in peripheral direction, while the axial velocity distribution is made uniform by the function of the small tubes structure [4-13]. Therefore, the swirl intensity can be defined as the ratio of the circumferential momentum to the axial momentum.

For axisymmetric flow, swirl intensity is usually defined by its swirl number (S). A parameter S that is used by several researchers [4-14 , 4-15] is defined as follow:

$$S = \frac{2\pi\rho \int_0^R v_x v_y r^2 dr}{2\pi\rho R \int_0^R r v_x^2 dr} \quad (4.1)$$

where r is the radial distance from a pipe axis, v_x is the streamwise mean velocity and v_y is the circumferential mean velocity.

An alternative to the parameter S on the rotating swirler is defined as follow [4-20]:

$$S = \frac{\omega D}{2U_m} \quad (4.2)$$

Equation (4.2) indicates that the swirl intensity can be evaluated directly from the angular velocity ω of the rotary pipe, the diameter D of the pipe and the bulk velocity U_m of the flow through the pipe.

4.2.2 Experimental Procedures

Firstly, Ultrasonic Velocity Profiler (UVP-Duo) was used to measure one-dimensional instantaneous velocity of fluid downstream of the first elbow. We expect to know flow phenomenon in the elbow for the condition of different Reynolds number and different swirl number. The water flows in the range of Reynolds number 10,000 to 30,000. The swirl number $S = 0.25$ to $S = 1.0$ were set up for inlet swirl condition. Then, the measurement test section was move to the second elbow to measure same like in the first elbow. **Figure 4.3** and **Figure 4.4** show experimental set up and detail view of test section. **Table 4.1** shows the experimental for one-dimensional velocity profile measurement UVP-Duo.

A phased array sensor, which has basic frequency 2 MHz, is installed through the pipe wall. Thus, there is a direct contact between sensor and fluid to overcome the refraction in the pipe wall. The cross-sectional plane measurement is performed at 7D downstream of the swirling generator to observe developed swirling flow. The angular velocity of rotating pipe is measured by a digital optical tachometer (AD-5172 A&D Company) with accuracy $\pm 0.01\% \pm 1$ digit (10 – 6,000 r.p.m.). According to the literature [26], $S=1$ corresponds to the downstream development of initially strong swirl in pipe flow. Therefore, in this experiment, the swirl number is set to $S = 1$ in order to know the influence of strong swirl intensity at the inlet. For the cross-sectional plane measurement, to include the whole 360 degrees of the pipe, one measurement position will be taken 20 degrees, which adds up to 18 measurement lines. **Table 4.2** shows the experimental conditions of the measurements. In case of

axial plane measurements, there are four measurement positions at $x/D = 0.2$, $x/D = 0.6$, $x/D = 1$ and $x/D = 1.5$ downstream of the double bend. After the measurement is done at the first position, the sensor is moved to another position. The maximum steering angle of the phased array sensor is -10 degree to 0 degree. In each measurement position, we measured 3 measurement lines, and the interval between each measurement lines is 5 degree as shown in **Figure 4.5**.

In addition, the cross-sectional plane measurement were done to find out the phenomenon of the radial velocity at the reattachment point region $x/D = 1$ in case of swirling flow. In the cross-sectional plane measurement, the measurement phased angle changes -10 degree to +10 degree and the total measurement lines is 13 lines and phased angle changes in every 2 degree.

4.3 Results and discussion

4.3.1 One-dimensional velocity analysis

In order to investigate the flow phenomenon in the elbow, one dimensional velocity measurements were performed in the first elbow and in the second elbow. **Figure 4.6 and Figure 4.7** show the measurement results in the first elbow in different Reynolds and in different swirl number. From that results, Reynold number effect on the movement of the reattachment is very small (around 2 mm). However, swirl number effect is obvious. The movement is around 12 mm. The same phenomenon occurs in the second elbow measurement results as shown in **Figure 4.8 and Figure 4.9**. Therefore, we can say swirl number influence on the movement of the reattachment point.

In the case of without inlet swirling flow condition, **Figure 4.10 and Figure 4.11** show the experiment results of one-dimensional normalized axial and tangential velocity with their standard deviations in four positions downstream of the double bend pipe.

Ten thousand instantaneous velocities are averaged in each velocity profile. The vertical axis indicates the dimensionless distance of measurement line through the pipe. The horizontal axis is the dimensionless axial and tangential velocity normalized by the average axial velocity and the average tangential velocity respectively. According to **Figure 4.10**, the low velocity magnitude was observed at $x/D = 0.2$ to $x/D = 1$ in the extrados pipe wall region ($y/D = 0.7$ to $y/D = 1$). This region ($y/D = 0.7$ to $y/D = 1$) is the secondary flow region. As we can see the velocity profiles in secondary flow region are slightly different in every axial position. These differences are related to the flow structure of the fluid, which flow direction is reverse to the main flow. Nevertheless, the velocity magnitude starts to increase at $x/D = 1$. Therefore, we can assume there is a no reverse flow beyond $x/D = 1$. **Figure 4.11** shows one-dimensional time-average tangential velocity at each measurement positions. The tangential velocity magnitude is relatively high on the secondary flow region, start from $x/D = 0.6$ to $x/D = 1.5$. At the center of the pipe ($y/D=0.5$), the velocity magnitude is relatively lower compared to the end wall regions. The reason is that the bend pipe curvature generate the centrifugal force and it enhances tangential velocity magnitude near the pipe walls.

Figure 4.12 shows the one-dimensional time-average axial velocity with their standard deviations downstream of the double bend pipe with inlet swirling flow condition ($S=1$). In the case without and with inlet swirling flow condition, at each axial measurement positions, there is no significant difference on the velocity profiles in the main flow region ($0 < y/D < 0.7$). However, in case of with swirling flow, the velocity magnitude in the secondary flow region ($0.7 < y/D < 1$) is stronger than without inlet swirling flow condition. These differences are due to the inlet swirling flow enhance the centrifugal force on the curvature bend. **Figure 4.13** shows the one-dimensional time-average tangential velocity profile of inlet swirling flow with their standard deviations. The strong tangential velocity occurs at $x/D = 0.6$ and $x/D = 1$ because the swirling enhance the tangential velocity in the main flow region ($0.1 < y/D < 0.4$) and the secondary flow region ($0.7 < y/D < 1$). These results indicate that tangential velocity in swirling flow is more dominant on main flow regime than

without swirling flow condition. According to the standard deviation, the tangential velocity fluctuation in the inlet swirling condition is higher than without inlet swirling flow. It means that the inlet swirling flow also increases the tangential velocity fluctuation.

4.3.2 Two-dimensional velocity with and without inlet swirling flow

Two-dimensional velocity measurement results are plotted to know the flow structure downstream of 90° double bend pipe in the condition of with and without inlet swirling flow. **Figure 4.14** shows two-dimensional time average axial velocity without inlet swirling flow at four downstream locations of the second bend pipe. The velocity vector cannot be measured enough near the oscillation boundary of the phased array sensor from $0 < y/D < 0.08$ for all positions due to the ultrasound field oscillation effects. From the measurement result at $x/D = 0.2$, the direction of velocity vectors separate from the edge of the bend. It indicates the flow separation starts from the edge of the bend at $x/D = 0.2$ (i.e., separation point). Then, the separated fluid attaches near the first line measurement of $x/D = 1.5$ (i.e., reattachment point). The secondary flow region is located between the separation point and the reattachment point. It means that there is a no reverse flow downstream the reattachment point and the flow acceleration occurs beyond the reattachment point.

Firstly, to confirm the inlet swirling condition, we visualized two-dimensional radial velocity as shown in **Figure 4.15**. The measurement is taken at 7D downstream from the swirling generator. It is confirmed that the generated swirling flow is symmetric, and the velocity distribution is homogenous. In the core region of the pipe, the velocity magnitude is lower than near wall region. The highest velocity magnitude is between the core and near wall region.

After confirming inlet swirling flow, we investigated the influence of swirling flow on the flow structure downstream of the double bend. **Figure 4.16** shows the measurement results in case of swirling flow condition. The result shows the flow separation phenomenon is same as the condition of without inlet swirling flow. However the reattachment point shift to upstream around 25 mm when swirling flow

is introduced as inlet condition. The reattachment point occurs near the first measurement line of $x/D = 1$. Therefore, the reverse flow region is narrow. At $x/D = 1.5$, the fluid becomes the accelerated swirling flow. **Figure 4.17** to **Figure 4.20** show two-dimensional radial velocity at the cross-sectional plane at $x/D = 1.0$ in the condition of swirling flow $S = 0.0$, $S = 0.25$, $S = 0.5$ and $S = 0.75$. From that measurement, the radial velocity fields were observed at the reattachment point region at $x/D = 1$.

4.3.3 Comparison of Velocity Fluctuation with and without Inlet

swirling flow

For the investigation of velocity fluctuation, we calculated turbulent intensity for axial velocity and tangential velocity in the condition of without inlet swirling flow and with inlet swirling flow respectively. The x-axis represents the normalized distance, and the y-axis represents turbulent intensity. The turbulent intensity of axial velocity and tangential velocity fluctuation is very effective to analyze the velocity fluctuation. **Figure 4.21** and **Figure 4.22** show the comparison of turbulent intensity in axial and tangential velocity at the position of $x/D = 1$ downstream of the double bend pipe. According to axial turbulent intensity graph, the axial velocity fluctuation is relatively high between $y/D = 0.6$ and $y/D = 0.8$ (see **Figure 4.21**). It means that the high-velocity fluctuation occurs at the boundary of the main flow and secondary flow. Moreover, the influence of reattachment point exists in this region. From the comparison, the axial velocity fluctuation of without inlet swirling is higher than inlet swirling. The reason is that the inlet swirling flow suppress axial velocity fluctuation.

Figure 4.22 shows tangential turbulent intensity analysis. This graph indicates the tangential velocity fluctuation is high near the extrados sidewall and at the center of the pipe. When the fluid touches the extrados sidewall, the flow direction changes. Some fluids flow as the main flow and some fluids change as the secondary flow. Therefore in the main flow region (near the extrados) and at the core of the secondary swirling flow (at the pipe center) occurs the high tangential velocity fluctuation. Here, the maximum turbulent intensity is around 40% with inlet swirling flow, and the

maximum turbulent intensity is around 25% without swirling flow. Therefore, the velocity fluctuation of inlet swirling flow is stronger than without inlet swirling flow. It seems that swirling flow enhances tangential velocity fluctuation.

4.4 Conclusions

Phased Array UVP system was applied for two-dimensional velocity measurements in the condition of without inlet swirling flow and with inlet swirling flow on the double bend pipe flow. According to one-dimensional velocity profiles, the velocity magnitude of inlet swirling flow is much stronger than without inlet swirling flow in the secondary flow region. These differences are due to the influence of the inlet swirling flow. In two-dimensional velocity of without inlet swirling flow, the flow separation occurs around $x/D = 0.1$, and the reattachment point is located at $x/D = 1.5$. In case of inlet swirling flow, the flow separation phenomenon is same as the condition of without inlet swirling flow, but the reattachment point is located at $x/D = 1$. Therefore, the reverse flow region is narrow. At $x/D = 1.5$, the fluid becomes the accelerated swirling flow. In the condition of without inlet swirling flow, the axial velocity fluctuation is higher than with inlet swirling flow, but tangential velocity fluctuation is lower than inlet swirling flow.

References

- [4-1] Sudo, K., Sumida, M., & Hibara, H. (1998) Experimental investigation on turbulent flow in a circular-sectioned 90-degree bend. *Experiments in Fluids*, **25**, 42-49. Karashi, Y., Uchiyama, K., Yamagata, T. and Fujisawa, N. (2016) Influence of swirling flow on mass and momentum transfer downstream of a pipe with elbow and orifice. *International Journal of Heat and Mass Transfer*, **92**, 394-402.
- [4-2] Paidoussis, M. P. (1983) A review of flow-induced vibrations in reactors and reactor components. *Nuclear Engineering and Design*, **74**, 31-60.
- [4-3] Enayet, M. M., Gibson, M. M., Taylor, A. M. K. P., & Yianneskis, M. (1982) Laser-Doppler measurements of laminar and turbulent flow in a pipe bend. *International Journal of Heat and Fluid Flow*, **3**(4), 213-219.
- [4-4] Crawford, N., Spence, S., Simpson, A., & Cunningham, G. (2009) A numerical investigation of the flow structures and losses for turbulent flow in 90 elbow bends. *Proceedings of the Institution of Mechanical Engineers, Part E: Journal of Process Mechanical Engineering*, **223**, 27-44.
- [4-5] Dutta, P., Saha, S. K., Nandi, N., & Pal, N. (2016) Numerical study on flow separation in 90° pipe bend under high Reynolds number by k- ϵ modelling. *Engineering Science and Technology, an International Journal*, **19**, 904-910.
- [4-6] Röhrig, R., Jakirlić, S., & Tropea, C. (2015) Comparative computational study of turbulent flow in a 90 pipe elbow. *International Journal of Heat and Fluid Flow*, **55**, 120-131.
- [4-7] Kim, J., Yadav, M., & Kim, S. (2014) Characteristics of secondary flow induced by 90-degree elbow in turbulent pipe flow. *Engineering Applications of Computational Fluid Mechanics*, **8**, 229-239.
- [4-8] Kawamura, T., Nakao, T., & Takahashi, M. (2002) Reynolds number effect on turbulence downstream from elbow pipe. *Trans. Jpn. Soc. Mech. Eng., Ser. B*, **68**, 645-651.

- [4-9] Kubo, T., Ebara, S., & Hashizume, H. (2012) Experimental Study of Influence of Elbow Curvature on a Swirling Flow Generated in a Three-Dimensionally Connected Dual Elbow. In *1st International Conference on Maintenance Science and Technology, E-Journal of Advanced Maintenance*, **5**, 34-41.
- [4-10] Sudo, K., Takami, T. and Hibara, H., Nomura, T. and Sumida, M. (1997) Weakly Swirling Flows through a 90° Bend. *Transactions of the Japan Society of Mechanical Engineers, Series B*, **63**,505-512.
- [4-11] Kalpakli, A., & Örlü, R. (2013) Turbulent pipe flow downstream a 90 pipe bend with and without superimposed swirl. *International Journal of Heat and Fluid Flow*, **41**, 103-111.
- [4-12] Saraç, B. A., & Bali, T. (2007) An experimental study on heat transfer and pressure drop characteristics of decaying swirl flow through a circular pipe with a vortex generator. *Experimental Thermal and Fluid Science*, **32**, 158-165.
- [4-13] Takano, T., Ikarashi, Y., Uchiyama, K., Yamagata, T. and Fujisawa, N. (2016) Influence of swirling flow on mass and momentum transfer downstream of a pipe with elbow and orifice. *International Journal of Heat and Mass Transfer*, **92**, 394-402.
- [4-14] Rocklage-Marliani, G., Schmidts, M., & Ram, V. I. V. (2003) Three-dimensional laser-Doppler velocimeter measurements in swirling turbulent pipe flow. *Flow, Turbulence and Combustion*, **70**, 43-67.
- [4-15] Kitoh, O. (1991) Experimental study of turbulent swirling flow in a straight pipe. *Journal of Fluid Mechanics*, **225**, 445-479.

Table 4.1 Experimental conditions for UVP-Duo

Parameters	Value
Reynolds number [$Re = \rho * D * U_m / \mu$]	10,000 , 20,000 and 30,000
Fluid (water) temperature	25 ± 1 °C
Swirl number S	0.0, 0.25, 0.5, 0.75, 1.0, 1.25 and 1.5
Frequency of transducer	4 MHz
Spatial resolution Δy	0.74 mm
Number of velocity profiles	10,000

Table 4.2 Experimental conditions and Phased Array UVP parameters

Parameters	Value
Reynolds number [$Re = \rho * D * U_m / \mu$]	10,000
Dean number [$De = Re * (R_c / D)^{0.5}$]	7,071
Fluid (water) temperature	25 ± 1 °C
Angular velocity of rotation pipe ω	0, 480 min ⁻¹
Swirl number S	0, 1
Frequency of phased array transducer	2 MHz
Steering angle θ_s	0, -5, -10°
Pulse repetition frequency f_{prf}	1 kHz
Number of repetition N_{rep}	256
Spatial resolution Δy	0.74 mm
Time resolution $\Delta t [N_{rep} / f_{prf}]$	0.256 s
Number of velocity profiles	10,000

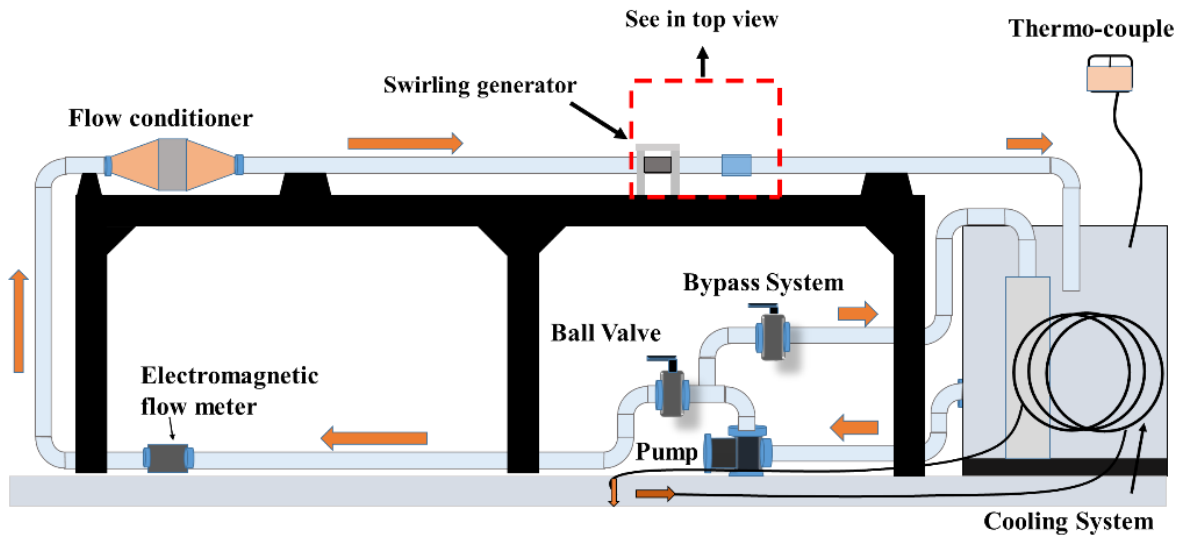


Figure 4.1 Experimental apparatus of water circulation system.

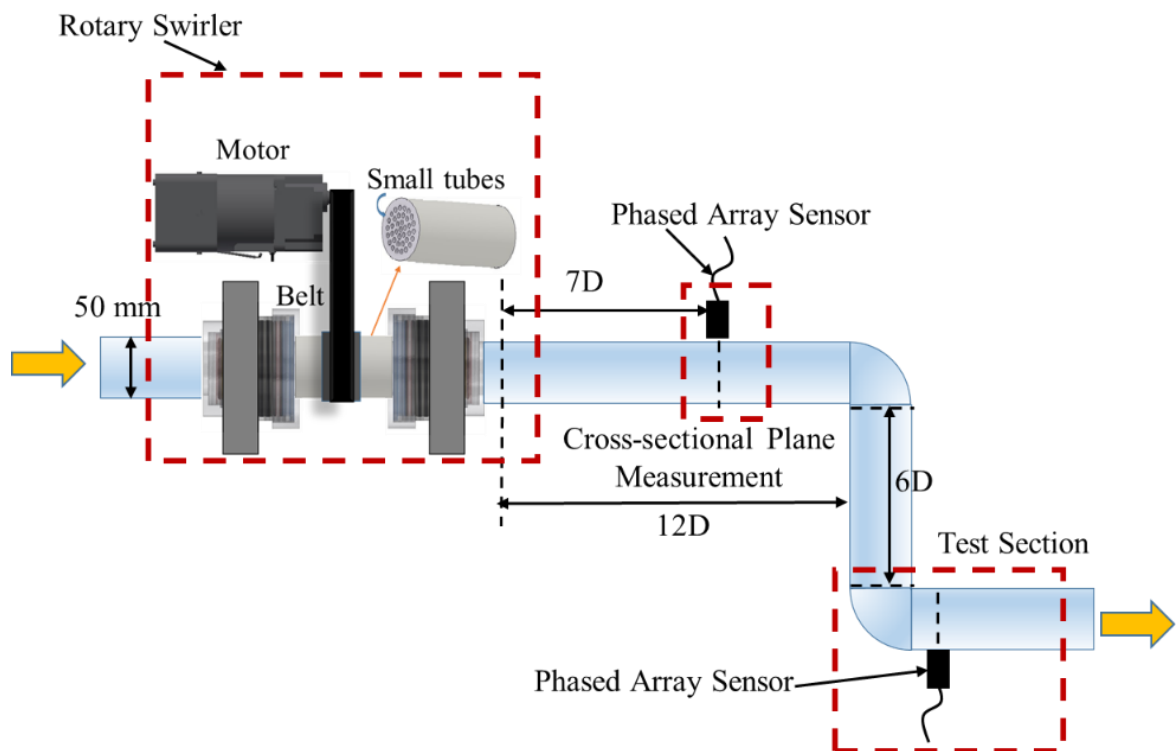


Figure 4.2 Swirling generator and double bend pipe from top view.

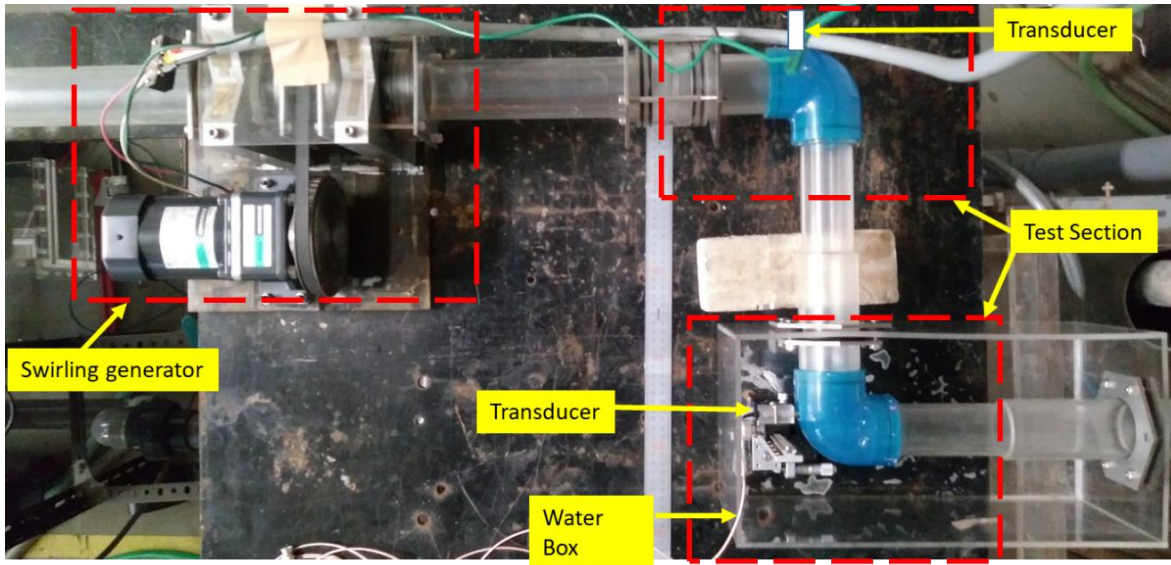


Figure 4.3 Picture of test section for one-dimensional measurement (UVP-Duo).

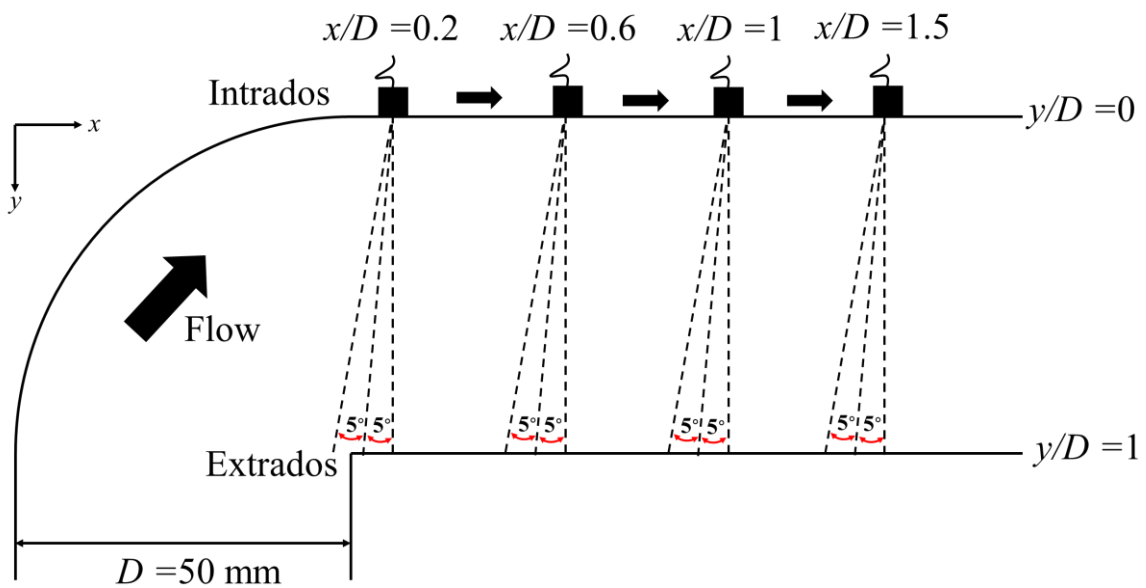
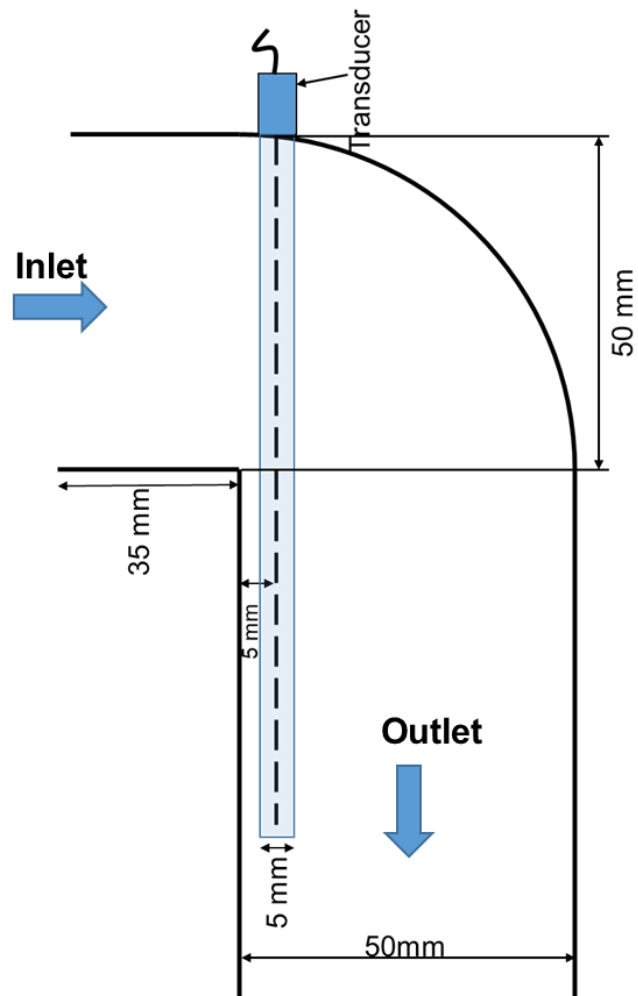
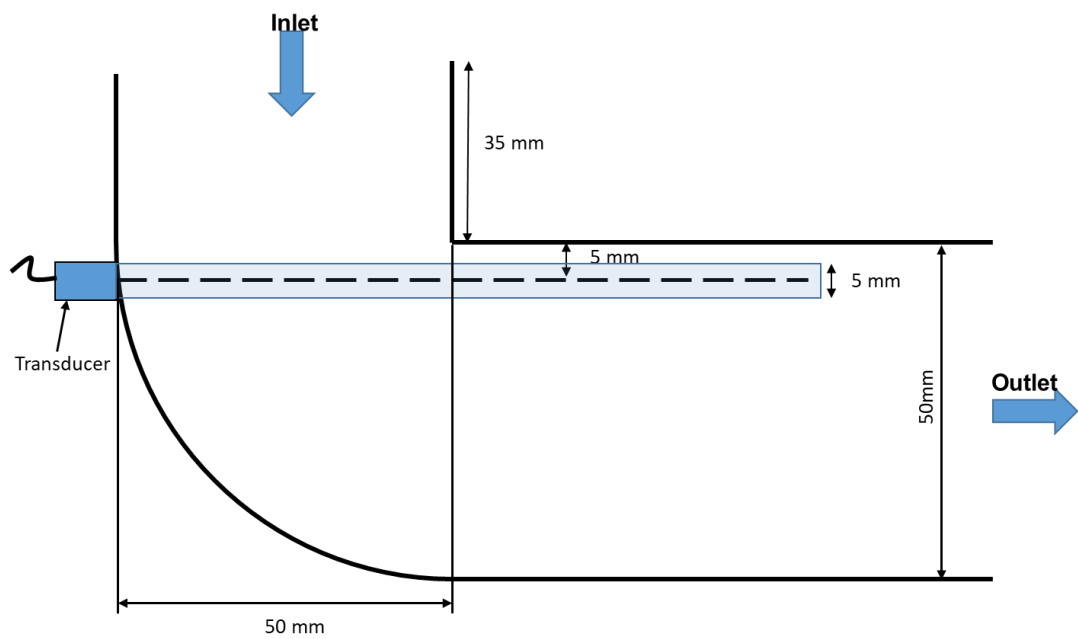


Figure 4.4 Detail view of the measurement positions (Phased Array UVP).



(a) Test section in First elbow (UVP-Duo).



(b) Test section in second elbow (UVP-Duo).

Figure 4.5 Detail view of test section in second elbow (UVP-Duo).

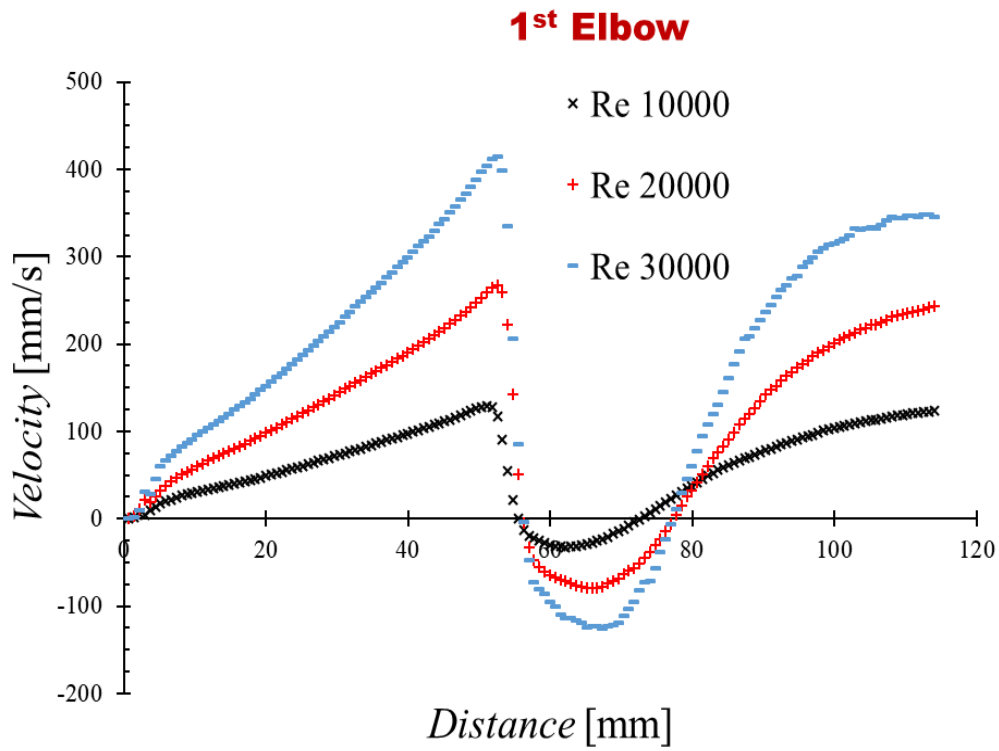


Figure 4.6 1D velocity profile in the first elbow for different Reynolds number.

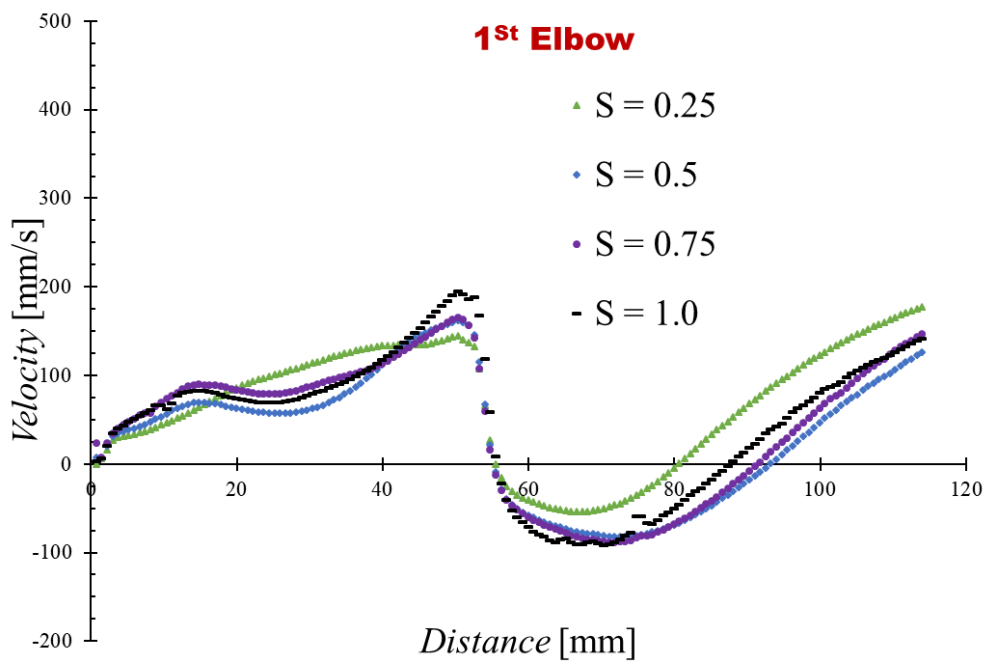


Figure 4.7 1D velocity profile in the first elbow for different swirl number.

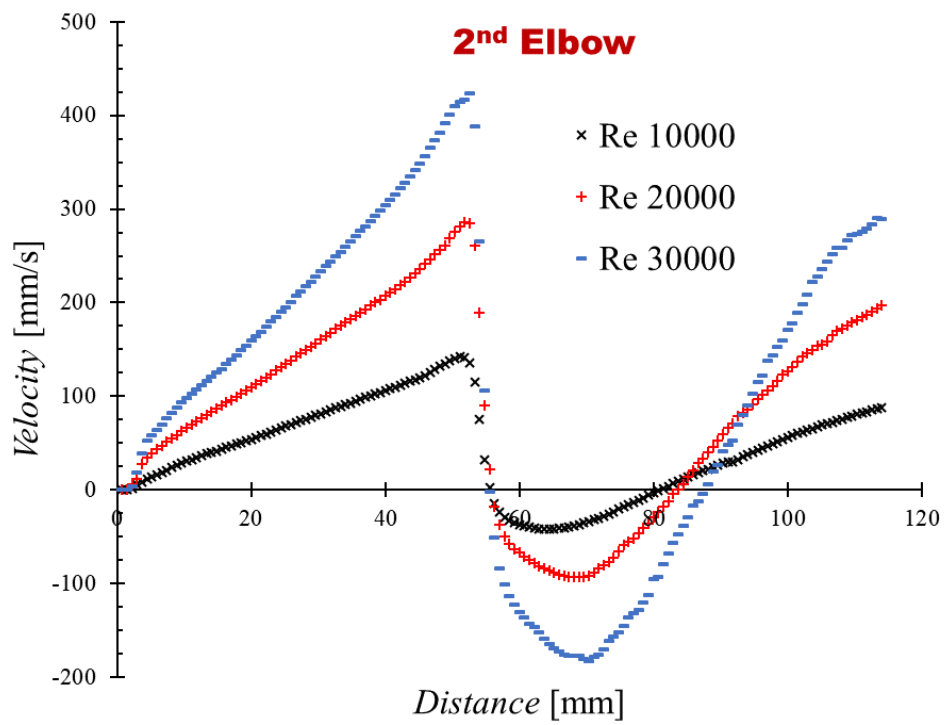


Figure 4.8 1D velocity profile in the second elbow for different Reynolds number.

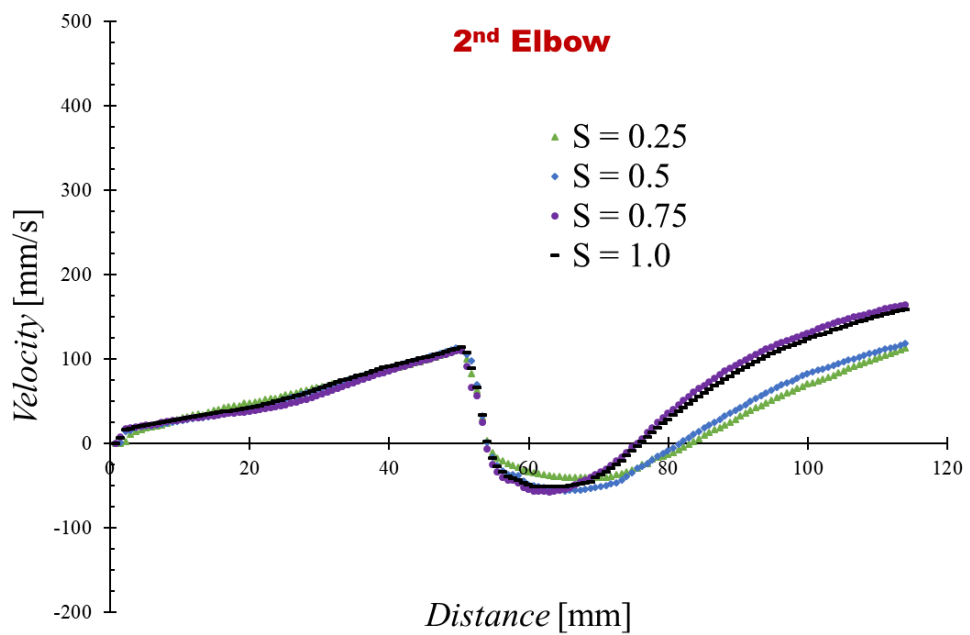


Figure 4.9 In the second elbow for different swirl number.

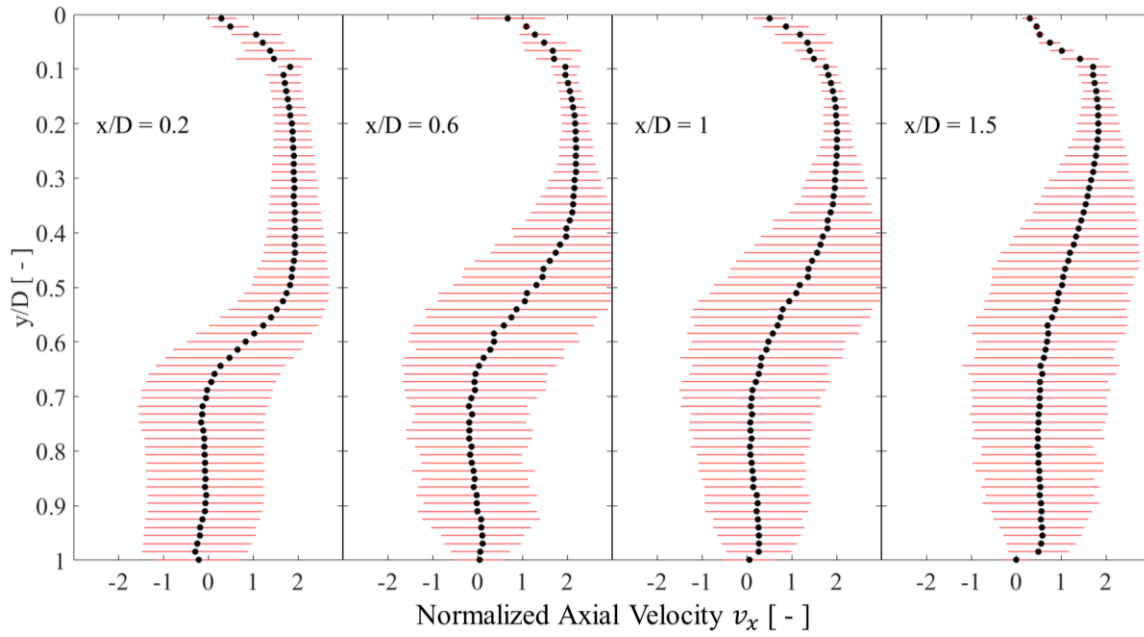


Figure 4.10 Time-average axial velocity without inlet swirling flow ($S=0$).

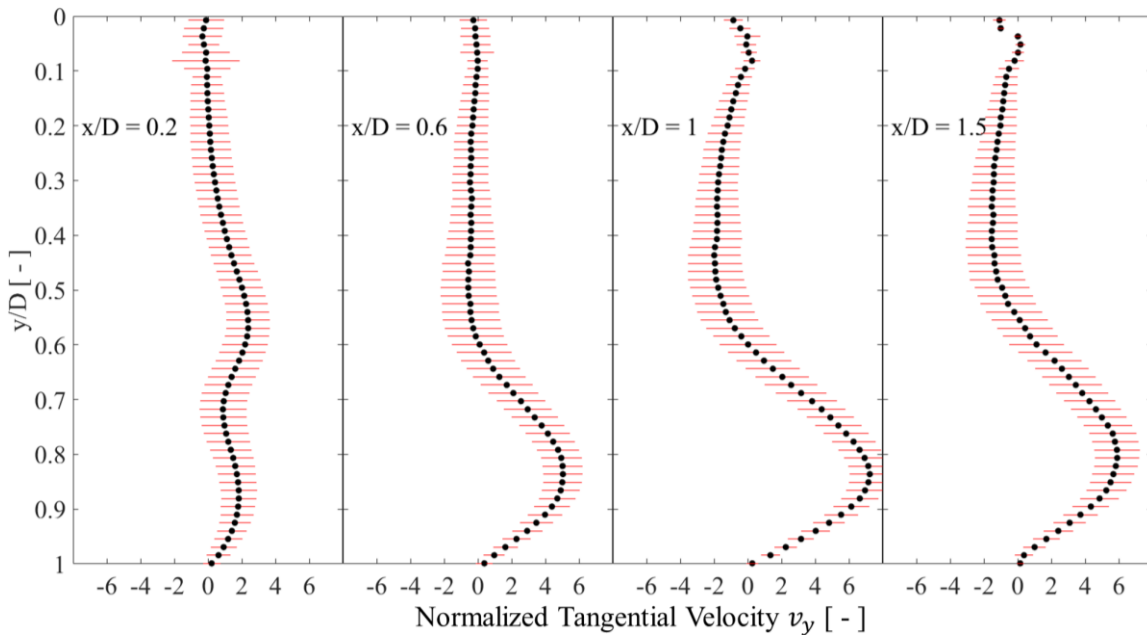


Figure 4.11 Time-average tangential velocity without inlet swirling flow ($S=0$).

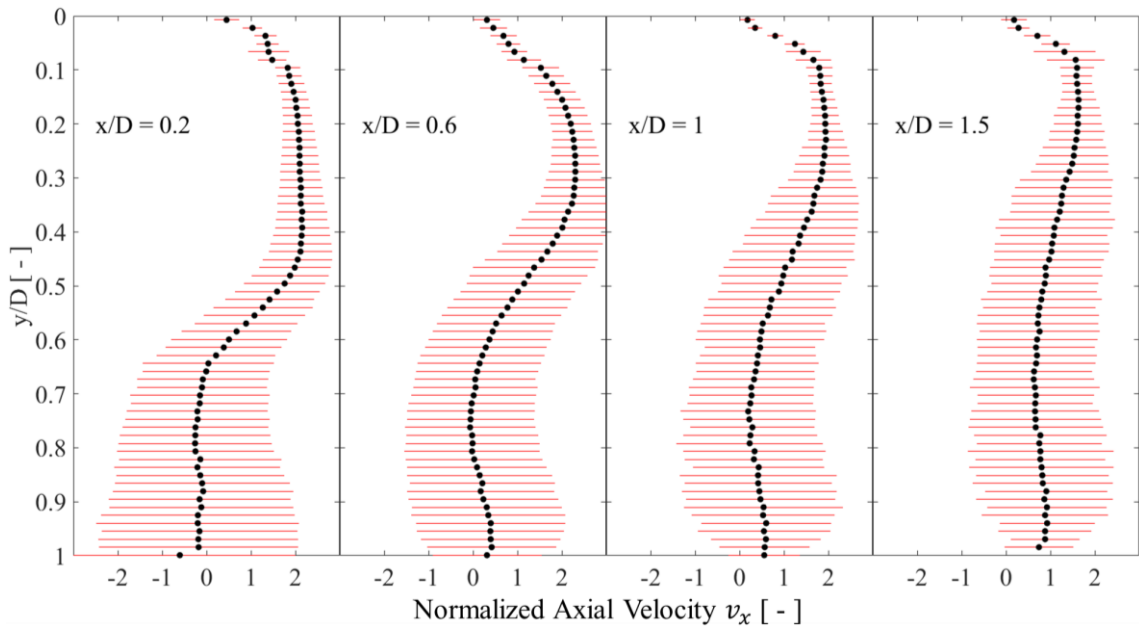


Figure 4.12 Time-average axial velocity without inlet swirling flow ($S=1$).

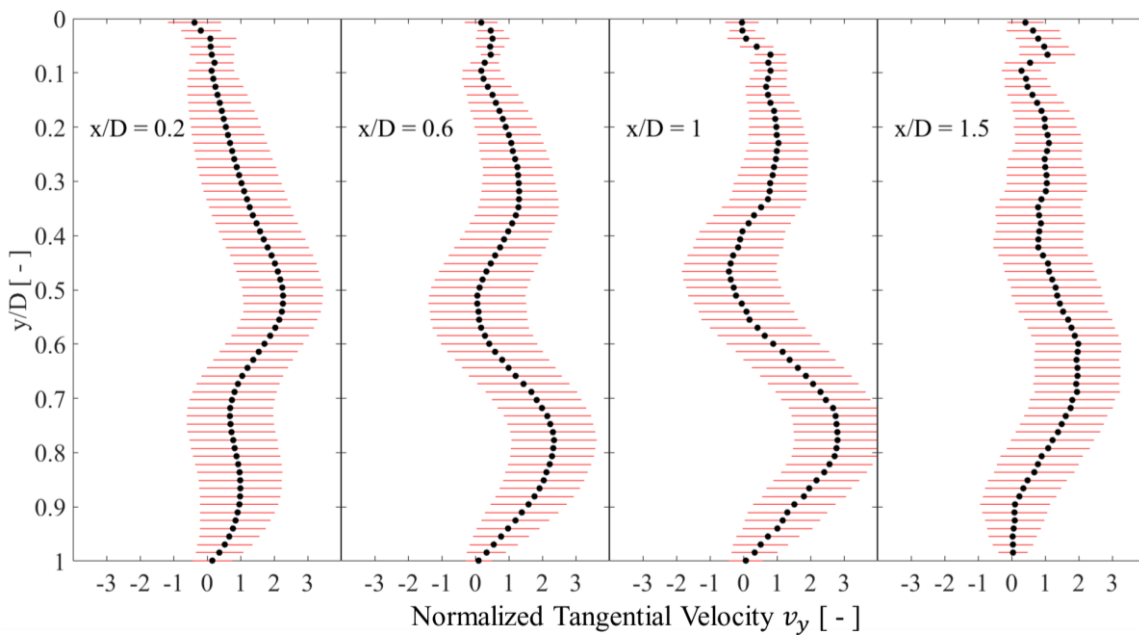


Figure 4.13 Time-average tangential velocity without inlet swirling flow ($S=1$).

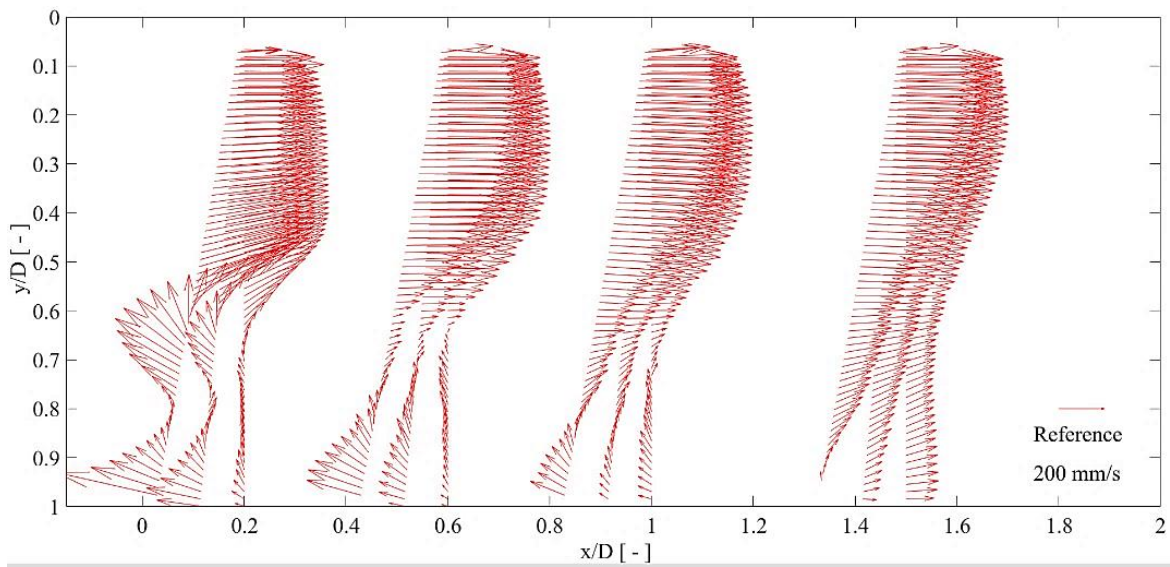


Figure 4.14 Two-dimensional time average axial velocity without inlet swirling flow ($S = 0$).

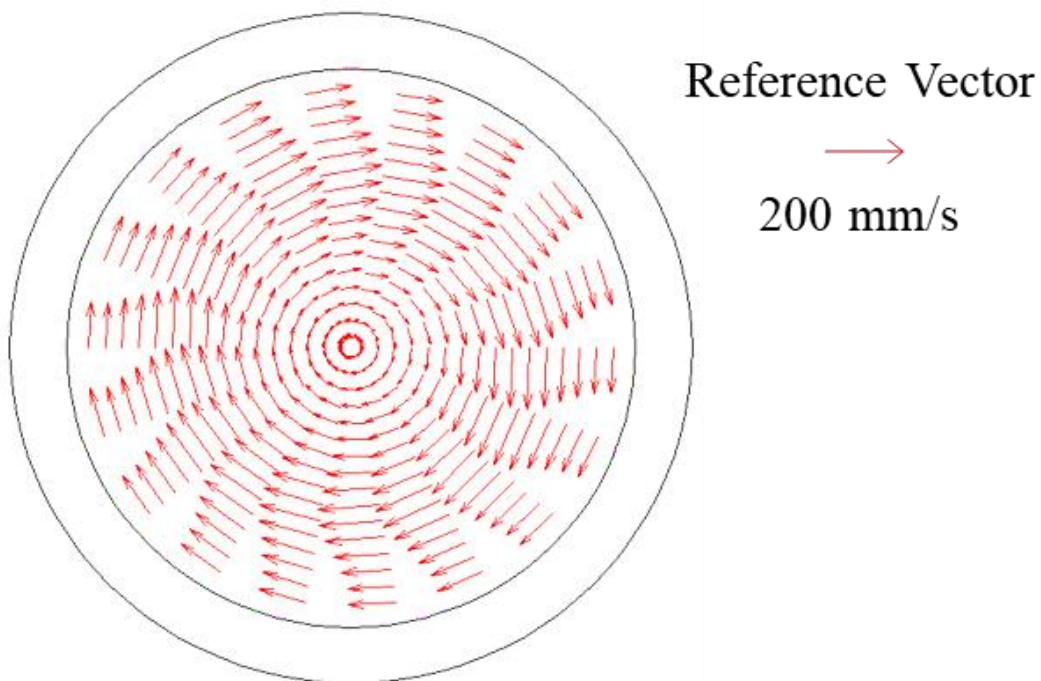


Figure 4.15 Two-dimensional time average radial velocity with the inlet swirling flow ($S = 1$).

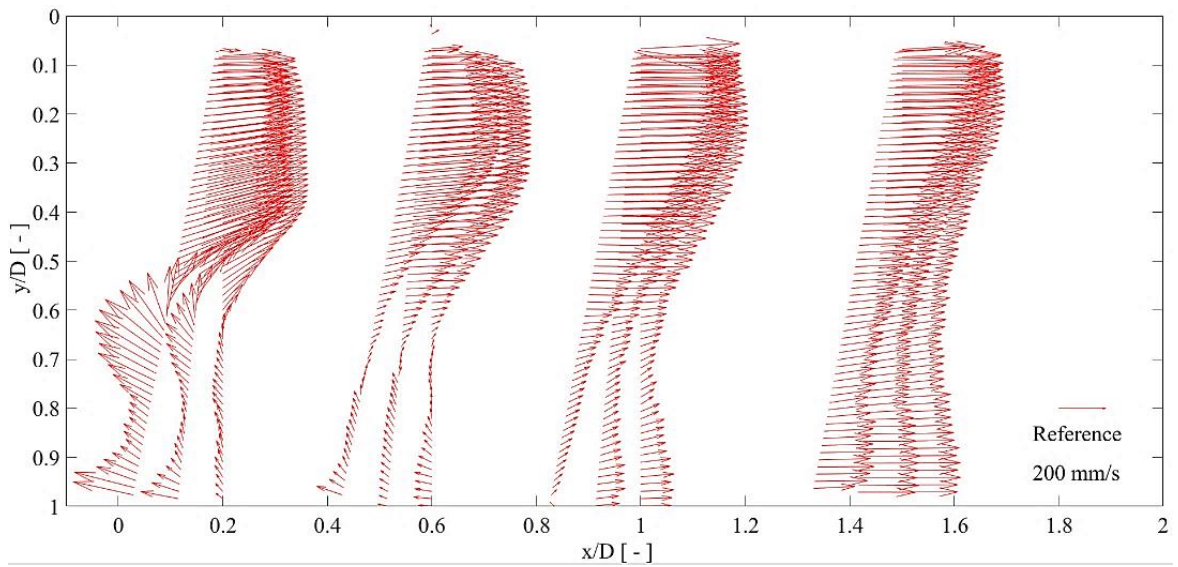


Figure 4.16 Two-dimensional time average axial velocity with the inlet swirling flow ($S = 1$).

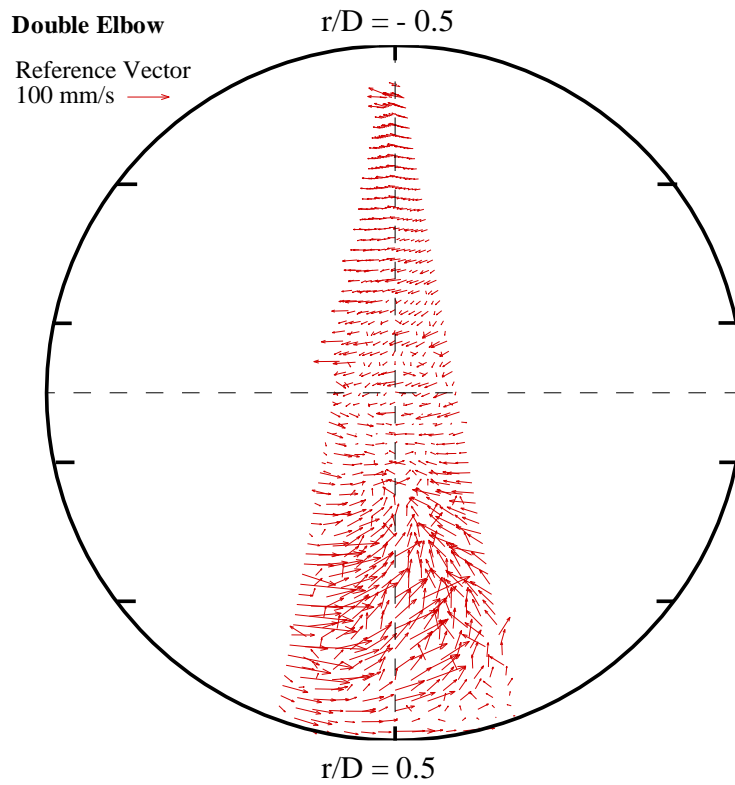


Figure 4.17 Two-dimensional time average radial velocity without inlet swirling flow ($S = 0.0$) at $x/D = 1$.

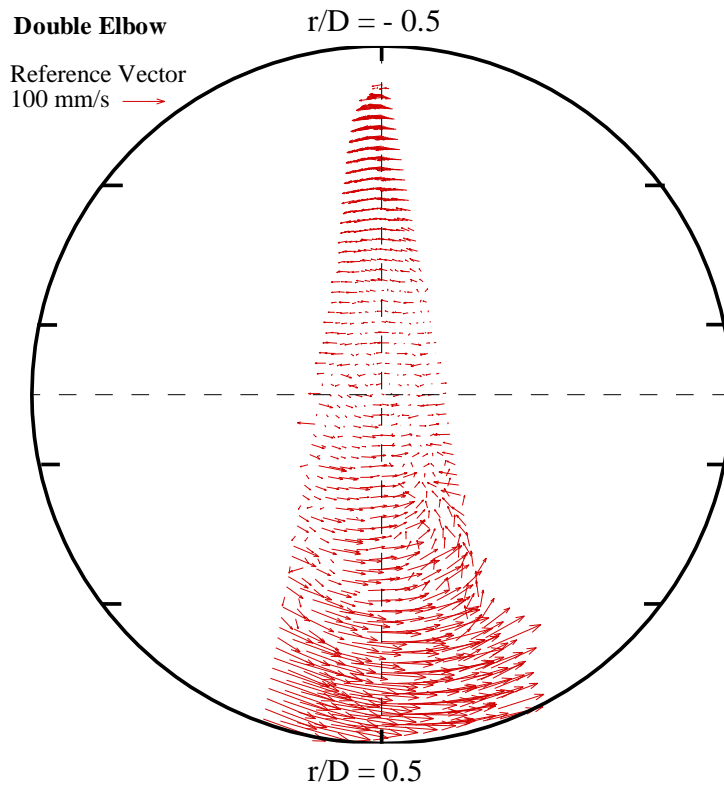


Figure 4.18 Two-dimensional time average radial velocity with the inlet swirling flow ($S = 0.25$) at $x/D = 1$.

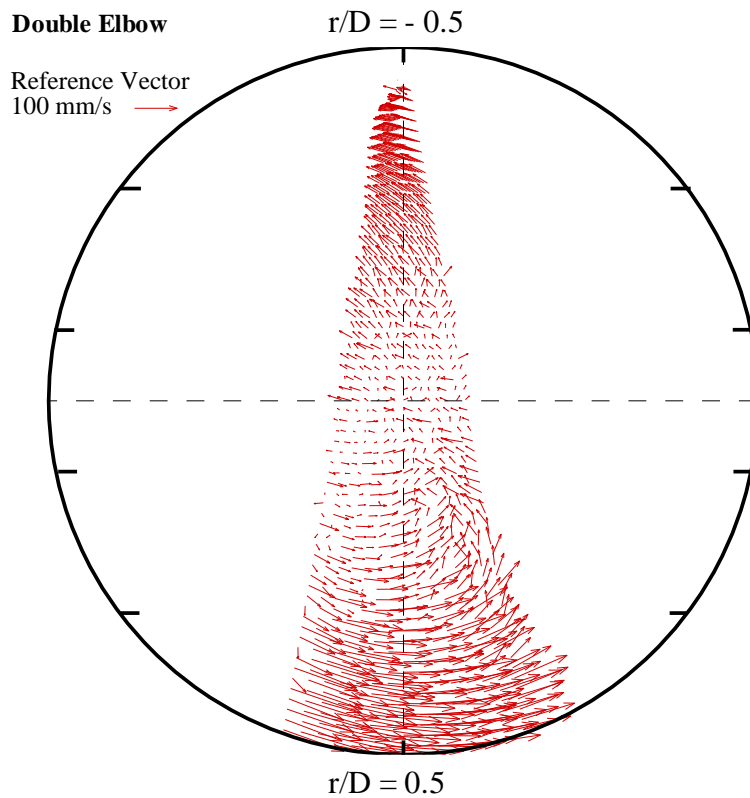


Figure 4.19 Two-dimensional time average radial velocity with the inlet swirling flow ($S = 0.5$) at $x/D = 1$.

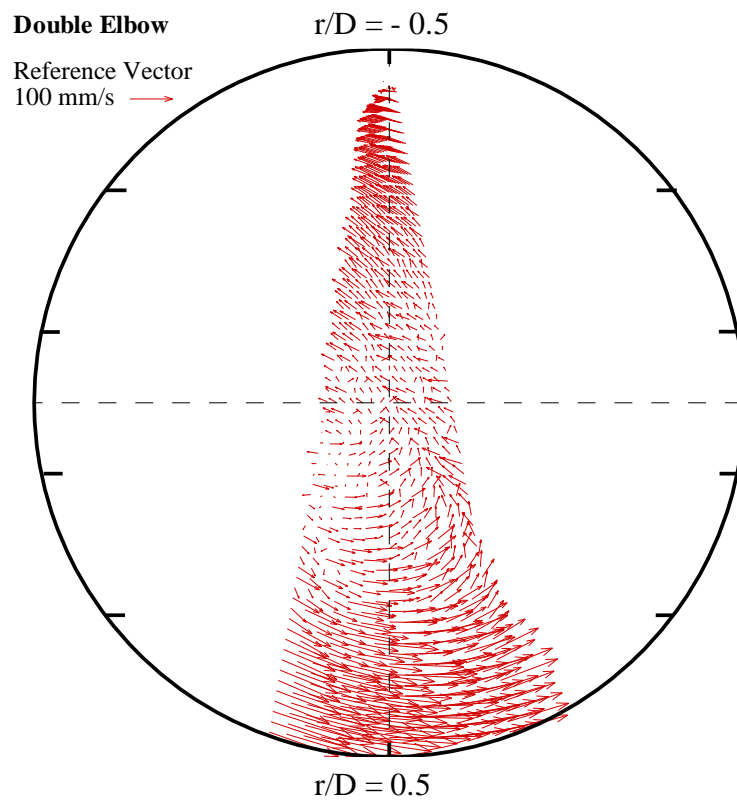


Figure 4.20 Two-dimensional time average radial velocity with the inlet swirling flow ($S = 0.75$) at $x/D = 1$.

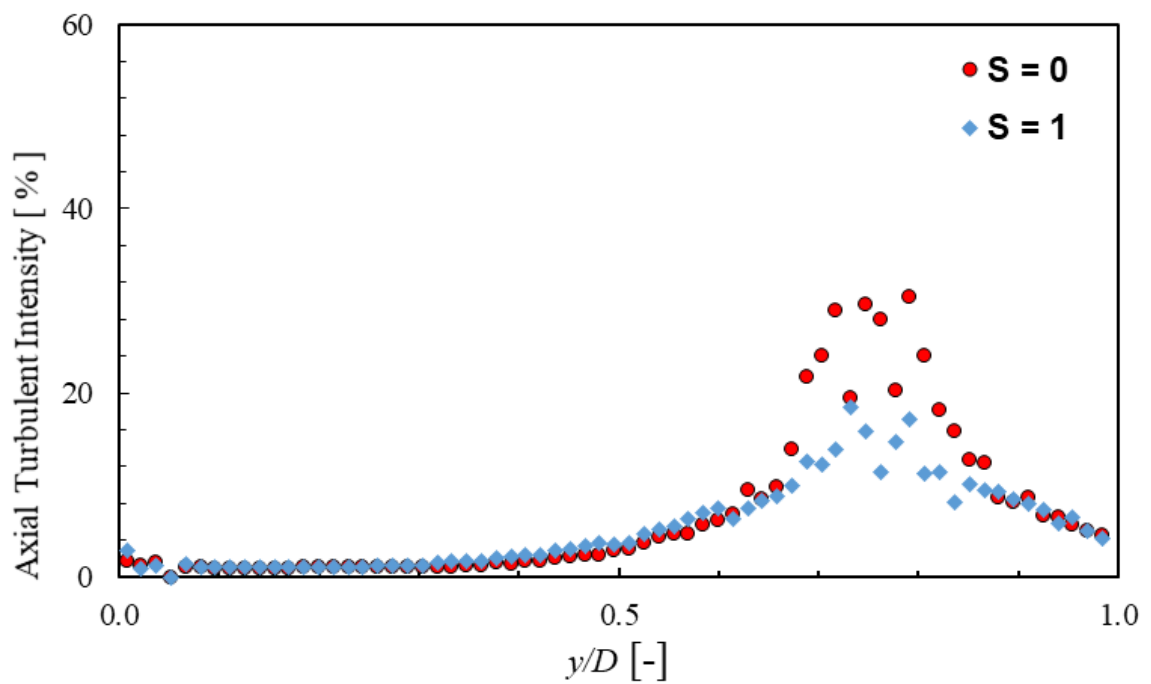


Figure 4.21 Comparison of the axial velocity fluctuation between with and without inlet swirling.

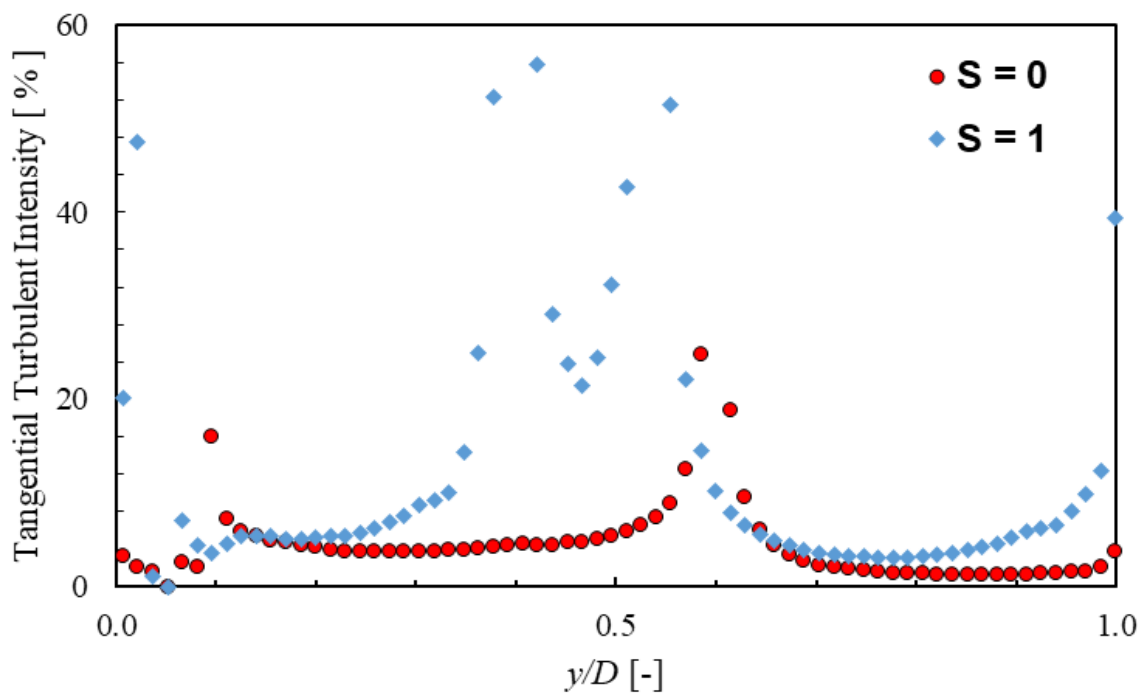


Figure 4.22 Comparison of the radial velocity fluctuation between with and without inlet swirling.

Chapter 5
Experimental and Numerical
Investigation of Swirling flow
Downstream of Triple Elbow
Pipe Layout

5.1 Introduction

Turbulent flow through a compact piping system is encountered in a variety of industrial applications and the power plants. The complicated flow occurs downstream region of the compact pipe layout. Also, the secondary swirling flow can be generated downstream of the elbow or 90-degree bend pipe. The bend pipes are always used for the different purposes. The investigation of fluid velocity fluctuation in the bend pipe layout is still challenging in the study of fluid dynamics. Under the swirling flow condition, the significant pressure fluctuation and the high-velocity fluctuation occur in the elbows. These are sources of flow-induced vibration (FIV). FIV can cause the corrosion phenomenon of the pipe wall, and then the pipe break accident happens in a piping system of the industries and the power plants [5.1 – 5.2]. The investigation of fluid flow structure and fluid velocity fluctuation are essential issues for the pipeline safety. Therefore, some researchers had attempted to investigate fluid flow structure and fluid velocity fluctuation on multiple bends pipe, experimentally and numerically.

In the previous studies, CFD simulation using Open FOAM® on 90-degree-bend elbow was performed to characterize the swirling secondary flow in the downstream of a pipe bend [1.12]. A comparative study was performed to select an appropriate turbulence model for the analysis. One of the first studies that provided the flow through a bend by Al-Rafai *et al.* using the $k - \varepsilon$ model [5.3] and compared with experimental results. They performed experiments and numerical calculations for a turbulent flow at $Re = 3.4 \times 10^4$ in two types of bend curvature ratio $\gamma = 0.07$ and 0.14. Laser Doppler Velocimetry (LDV) was utilized in the experiment. The main results consisted of mean and root mean square stream wise velocities. The result showed that the secondary flow is stronger in the bend with the higher curvature ratio γ . In addition, Hilgenstock and Ernst [1.14] tested two common models ($k - \varepsilon$ and renormalization group known as RNG) and provided acceptable results. Kalpakli and Örlü [5.4] studied experimental study for the turbulent flow in a bend pipe with imposed swirl. They studied Dean vortices and swirl motion for swirl intensity $S = 0$

to 1.2 at the downstream region of a bend pipe by using Particle Image Velocimetry (PIV) method. Chang and Lee [1.19] also investigated the effects of swirl on the secondary flow field along a bend in Reynolds number $Re = 1.0 - 2.5 \times 10^4$. The measurement system of previous studies, LDV and PIV system were applied to investigate fluid velocity and swirling flow structure. However, these systems have some challenges and it is difficult for the applications in actual plant process. Therefore, another measurement technique should be developed to evaluate the velocity field and velocity fluctuation. In this study, the ultrasonic technique is applied to measure two-dimensional velocity field.

The main objective of this study is to observe velocity field of secondary swirling flow which, occurs just downstream of the triple bend pipe. The swirling flow structure was visualized downstream of the triple elbows layout using Phased Array Ultrasonic Velocity Profiler (Phased Array UVP). In addition, the experimental results were performed to validate CFD numerical simulation. In this paper, the complexity of the turbulent flow under the swirling inlet flow condition is studied.

5.2 Experimental Apparatus and Measurement Procedures

The experiment was conducted in a water circulation system, which consisting of the cooling system and electromagnetic flow meter as shown in **Figure 5.1**. The inner diameter of the pipe is 50 mm and made of acrylic. The distance from the inlet to the triple elbows pipe is $42D$ ($D = 50$ mm). In that position, the fluid is in the fully developed turbulent pipe flow condition. The elbow has the curvature radius $R = 25$ mm. The geometry of the triple pipe layout is follow as the hot leg pipe of Japan sodium-cooled fast reactor (JSFR), which pipe diameter is 1/24 scale model of the actual pipe. The water flows in the turbulent flow condition at Reynolds number ($Re = 1 \times 10^4$). The cooling system controlled the water temperature to get room temperature 25°C . The temperature fluctuation is recorded using thermocouple during the measurements and the fluctuation is $\pm 1^\circ\text{C}$. For the generation of swirling flow, some different methods exist (pipe rotation, tangential injection, and vanes),

which have a different effect on the base flow [5.12]. In this present study, we used the pipe rotation method [5.1]. The swirl generator is installed at $10D$ upstream of the triple elbows. The detail view of the experimental set up with swirling generator is shown in **Figure 5.2**. The honeycomb is inserted into the rotary pipe to generate homogeneous swirl. The rotary pipe is used as the swirl generator because it is easy to control the swirl intensity.

A phased array sensor, which has basic frequency 2 MHz, is installed through the pipe wall. Thus, there is a direct contact between sensor and fluid to overcome the refraction in pipe wall and fluid medium. To measure inlet swirling flow, the axial and cross-sectional planes measurements were performed at $7D$ downstream of the swirling generator. One dimensional axial, radial and tangential velocity profiles of the swirling flow were collected in order to use as the inlet boundary condition for the numerical simulation. **Table 1** shows the experimental conditions of the measurements. For the axial flow measurements, there are 4 measurement positions at $x/D = 0.1$, $x/D = 0.6$, $x/D = 1$ and $x/D = 1.5$ downstream of the third elbow to find out velocity fluctuation in the secondary flow region. After the measurement was done at the first position, the sensor was moved to another position. The maximum steering angle of the phased array sensor is -10 degree to 0 degree. In each measurement position, we measured 3 measurement lines, and the interval between each measurement lines is 5 degree as shown in **Figure 5.3**.

In case of flow phenomenon observation, Ultrasonic Velocity Profiler (UVP-Duo) was used to measure one-dimensional instantaneous velocity of fluid downstream of the third elbow. We expect to know flow phenomenon in the elbow for the condition of different Reynolds number and different swirl number. The water flows in the range of Reynolds number 10,000 to 30,000. The swirl number $S = 0.25$ to $S = 1.0$ were set up for inlet swirl condition. **Figure 5.4** and **Figure 5.5** show experimental set up and detail view of test section.

5.3 Numerical Simulation Approach

A CFD analysis was performed for the turbulent fluid flow through the triple bend pipe. Three elbows with 25 mm radius of curvature make the triple bend pipe. The pipe layout was same as the experimental setup. The CFD code ANSYS Fluent (Version 16.2) was used to simulate a pipe flow through the triple elbow pipe layout as shown in **Figure 5.6**. The inlet length, upstream of the triple elbow is $3D$. Here, the inlet length can be reduced because the inlet swirling velocities from the experiment were utilized as the import profile. The pipe length from the downstream of the second bend is set to $6D$ to reduce calculation time and mesh element numbers. The mesh type was a polyhedral cell, and a total number of meshes was approximately 1.8 million. **Table 5.2** shows numerical parameters. Polyhedral cell type was used to get a proper orthogonal and skewness values. The mesh in the boundary layer close to the pipe has the inflection layer in the thickness of 0.02 mm and the total number of layer was 7. Mesh quality of the outlet cross-sectional plane is shown in **Figure 5.7**.

5.4 Experimental results and discussion

5.4.1 One-dimensional velocity profiles

In order to investigate the flow phenomenon in the elbow, one dimensional velocity measurements were performed in the third elbow. **Figure 5.8** and **Figure 5.9** show the measurement results in the third elbow in different Reynolds and in different swirl number. From those results, Reynold number effect on the movement of the reattachment is very small. However, swirl number effect is obvious. In third elbow, reverse flow region is narrow on Re 10,000 because pipe layout is vertical and the length between second and third are longer than between first and second elbow. Reattachment point for Re 20,000 and 30,000 occurs almost at the same position. Swirl number effect is still obviously influence on the changes of reattachment point.

The axial, radial and tangential velocities of the swirling flow were measured at $7D$ downstream of the swirling generator by using a phased array sensor. The sensor position was turned into the axial and cross-sectional planes to get the axial, radial and tangential velocities. The velocities were utilized for the boundary inlet conditions of the numerical simulation. **Figure 5.10**, **Figure 5.11** and **Figure 5.12** show one dimensional axial, radial and tangential velocity profiles of swirling flow at the radial distance of the pipe in the condition of swirl intensity $S = 1$ at Reynolds number $Re = 1 \times 10^4$. Due to the homogenous asymmetrical velocity distribution, the half velocity profiles were shown in the figure. The mean velocity distribution of swirling flow is lower than the near wall region. At the swirl core region, the velocity profiles of swirling flow are a bit flat because of the main flow velocity and the swirl intensity is not too high turbulent flow condition.

5.4.2 Two-dimensional velocity fields

At the downstream region of the triple elbows, we investigated the flow structure of the swirling flow. Two-dimensional velocity measurement results are plotted to visualize the swirling flow structure. Ten thousand instantaneous axial velocity vectors are averaged in each measurement line. **Figure 5.13** shows the measurement results of swirling flow at $x/D = 0.2$ to $x/D = 1.5$ in the downstream region of the triple elbows. The vertical axis indicates the dimensionless distance of the measurement line through the pipe. The horizontal axis is measurement positions downstream of the triple elbows. From the measurement result at $x/D = 0.2$, the direction of velocity vectors separate from the edge of sharp elbow. It indicates the flow separation starts from the edge of the elbow at $x/D = 0.2$ (i.e., separation point). Then, the separated fluid attaches near the first line measurement of $x/D = 1$ (i.e., reattachment point). The secondary flow region is located between the separation point and the reattachment point ($0.2 < x/D < 1$). The slow reverse flow occurs at $0.7 < y/D < 1$ in the secondary flow region. It means that there is a no reverse flow downstream the reattachment point ($x/D > 1$). However, the accelerated swirling flow still occurs beyond the reattachment point because the velocity magnitude at the

near pipe wall is still higher than at the pipe center. This experimental result was compared with CFD numerical simulation.

5.5 Numerical results and discussion

5.5.1 Two-dimensional velocity fields

The inlet swirling flow velocities from the experimental results were utilized to compare with experimental result and validate CFD numerical simulation. We used the axial, radial and tangential velocity profiles of swirling flow as the inlet boundary conditions and the geometry of the pipe layout was same as the experimental setup. **Figure 5.14** shows two-dimensional velocity field of the swirling flow structure from the numerical simulation result. If we compare with the experimental result, we can observe a good agreement with the experiment expect the separation flow pattern at $x/D = 0.2$. In the separation region, the fluid separation is not strong as the experiment. The reattachment point of the fluid occurs as same as the experiment around $x/D = 1$. It means the area of the reverse flow and secondary flow area is exactly located between $x/D = 0.2$ and $x/D = 1$. We can confirm the flow structure and the validation of CFD numerical simulation is acceptable. Furthermore, the flow visualization of numerical simulation results for the cross-sectional plane were plotted to observe detail flow structure of swirling fluid. For the investigation of velocity distribution, we visualized the velocity fields and axial velocity (velocity u) contour in the cross-sectional planes downstream of the triple elbows. The numerical simulation results at 10 mm, 30mm, 50mm and 75mm ($x/D = 0.2$, $x/D = 0.6$, $x/D = 1$ and $x/D = 1.5$) see in **Figure 5.15** to **Figure 5.18**. The top of each figure is the outside of the elbow (intrados) and the bottom is inside of the elbow (extrados). We can observe clearly the reverse flow in the secondary flow region at the extrados of elbow (see in **Figure 5.17** and **5.18**). Two counter rotating vortex cells (Dean vortices) can be seen near the left and right parts of elbow as shown in **Figure 5.15** and **Figure 5.16**. Then, the flow pattern is slightly changes as the circumferential flow in the clockwise

and counterclockwise directions from the lateral side of the pipe wall to the pipe center as shown in **Figure 5.17** and **5.18**. The axial velocity distribution is too different between the intrados and extrados of elbow according from the contour of each figure.

5.6 Conclusions

In conclusion, the experimental investigation and numerical simulation were done to observe the flow structure and velocity distribution at the inlet swirling flow condition. Phased Array UVP system can visualize two-dimensional velocity field and can confirm the flow separation and reattachment point. The flow separation occurs around the edge the sharp elbow and the reattachment point is located near $x/D = 1$. The numerical simulation result show that the swirling flow structure is quite similar with the experimental result. Therefore, the validation of the CFD simulation is acceptable. In case of cross-sectional plane visualization, two counter rotation vortex cells were observed at $x/D = 0.2$ and $x/D = 0.6$ positions. Then, the flow pattern is slightly changes as circumferential flow at $x/D = 1$ and $x/D = 1.5$. When the high velocity axial flow reached the outside wall, this flow was changed from outside to lateral side of pipe wall in clockwise and counterclockwise directions. In addition, the axial velocity distribution is too different between the intrados and extrados of pipe.

References

- [5-1] Fujisawa, N., 1996. Velocity measurements and numerical calculations of flow fields in and around Savonius rotors. *Journal of Wind Engineering and Industrial Aerodynamics*, 59(1), pp.39-50.
- [5-2] Kim, J., Moin, P. and Moser, R., 1987. Turbulence statistics in fully developed channel flow at low Reynolds number. *Journal of fluid mechanics*, 177, pp.133-166.
- [5-3] Al-Rafai, W.N., Woolley, N.H., Tridimas, Y.D. and Parry, A.J., 1991. Influence of solids concentration and size on gas-solid suspension flow in a 90° pipe bend. *Advanced Powder Technology*, 2(2), pp.133-150.
- [5-4] Örlü, R. (2009) Experimental studies in jet flows and zero pressure-gradient turbulent boundary layers. Doctoral dissertation, KTH

Table 5.1. Experimental conditions

Parameters	Value
Reynolds number [$Re = \rho * D * U_m / \mu$]	10,000 , 20,000 and 30,000
Dean number [$De = Re * (R_c / D)^{0.5}$]	7071
Fluid (water) temperature	25 ± 1 °C
Angular velocity of rotation pipe ω	0, 480 min^{-1}
Swirl number S	0, 0.25, 0.5, 0.75 and $S = 0.1$
Frequency of single and phased sensor	4 MHz and 2 MHz
Steering angle θ_s	0, -5, -10°
Pulse repetition frequency f_{prf}	1 kHz
Number of repetition N_{rep}	256
Spatial resolution Δy	0.74 mm
Time resolution $\Delta t [N_{rep} / f_{prf}]$	0.256 s
Number of velocity profiles	10000

Table 5.2. Numerical conditions

Parameters	Value
Turbulence model	$k - \epsilon$ (RNG)
Time	Steady state
Pressure-velocity coupling	SIMPLE
Gradient	Least squares cell based
Pressure	PRESTO!
Momentum	Quick
Turbulent kinetic energy	Quick
Specific dissipation rate	Quick
Mesh type	Polyhedral
Number of mesh	1.4×10^6
Inlet velocity	Axial, Radial and Tangential velocity profiles from the experiment

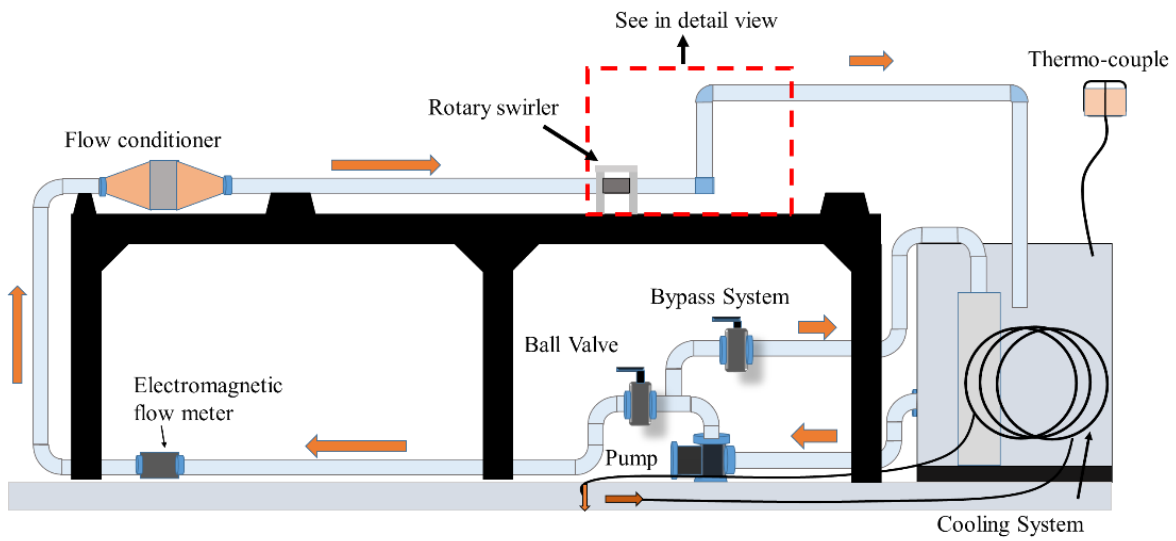


Figure 5.1 Experimental facilities of a piping system.

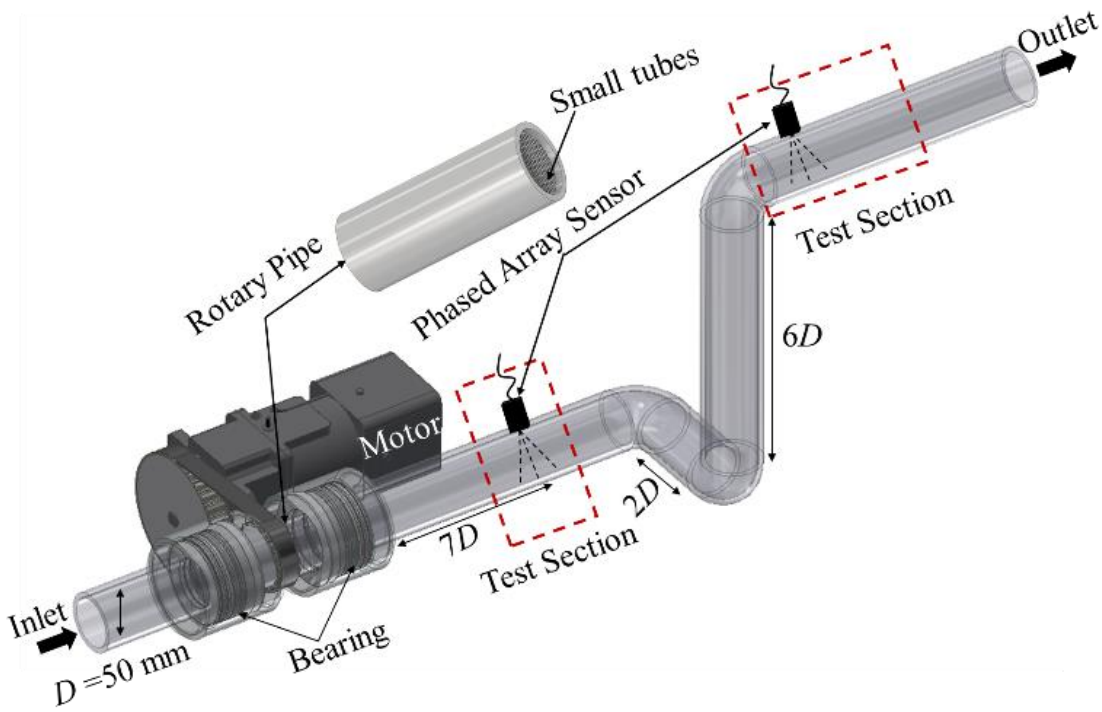


Figure 5.2 Detail view of the rotary swirler and pipe layout.

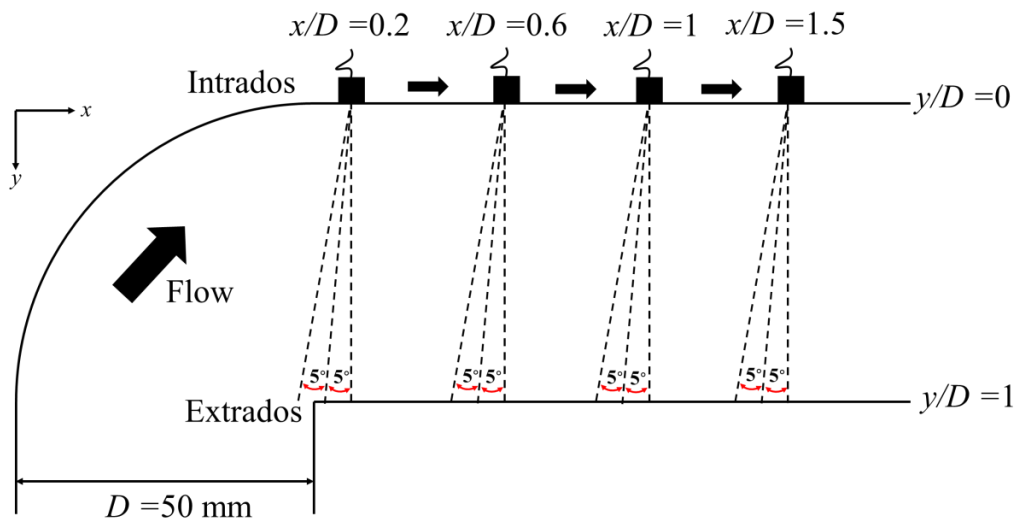


Figure 5.3 Test section downstream of the third elbow.

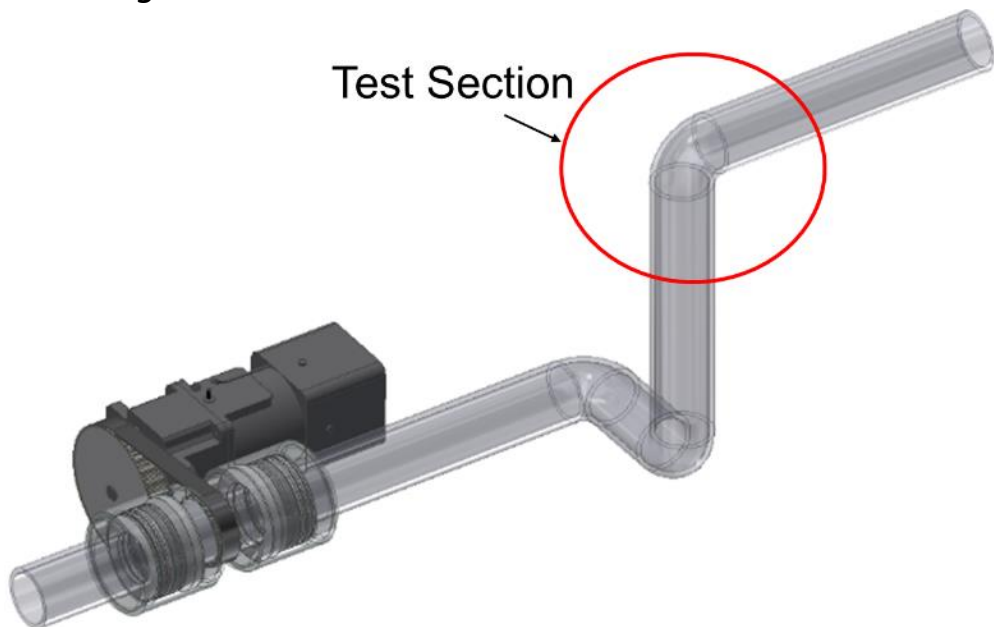


Figure 5.4 Test section in the third elbow for 1D velocity measurement

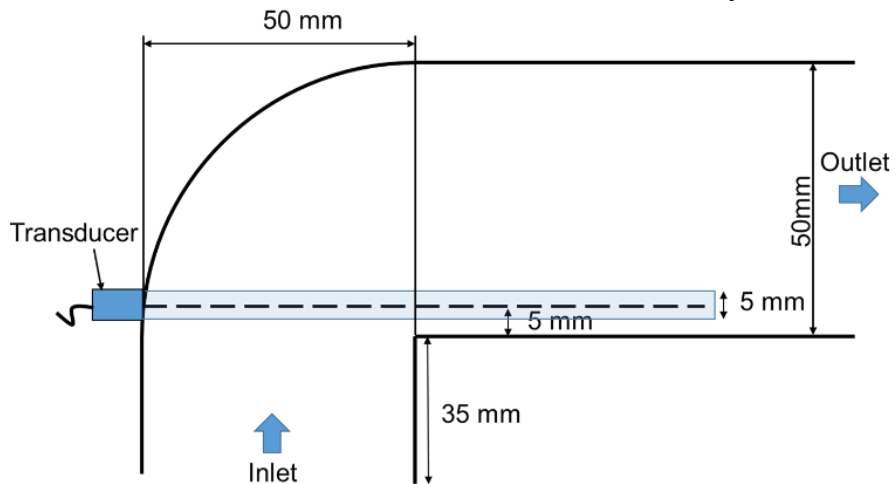


Figure 5.5 Detail view of Test section for 1D velocity measurement

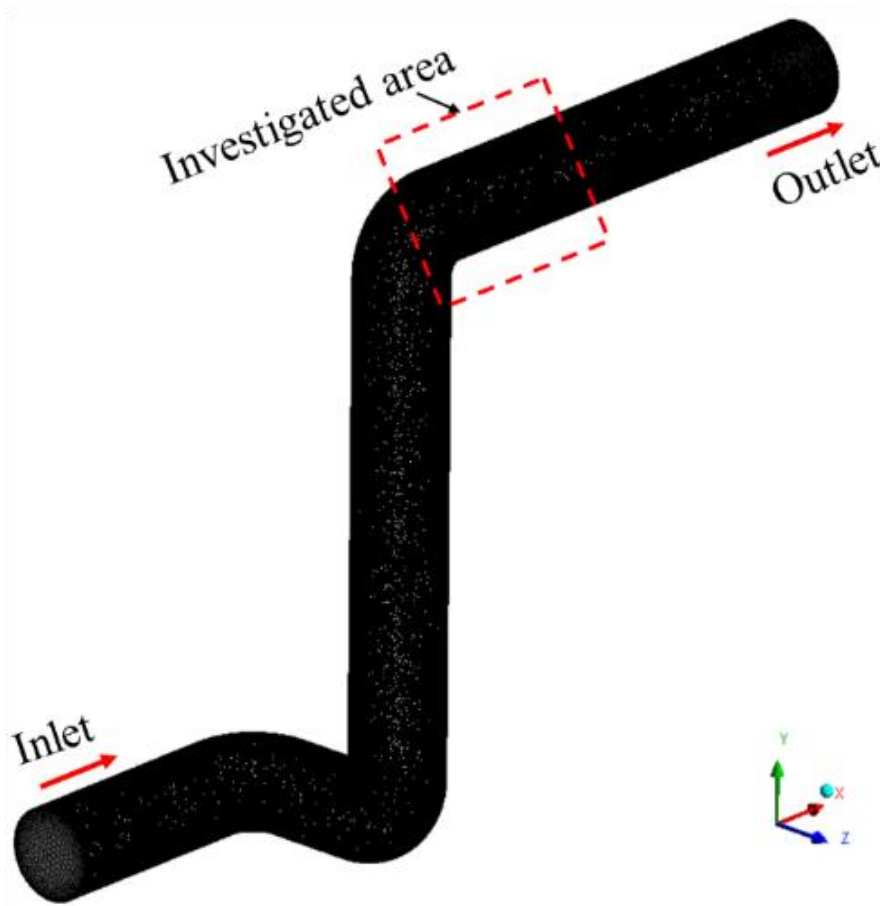


Figure 5.6 Simulation pipe geometry same as pipe layout with experiment.

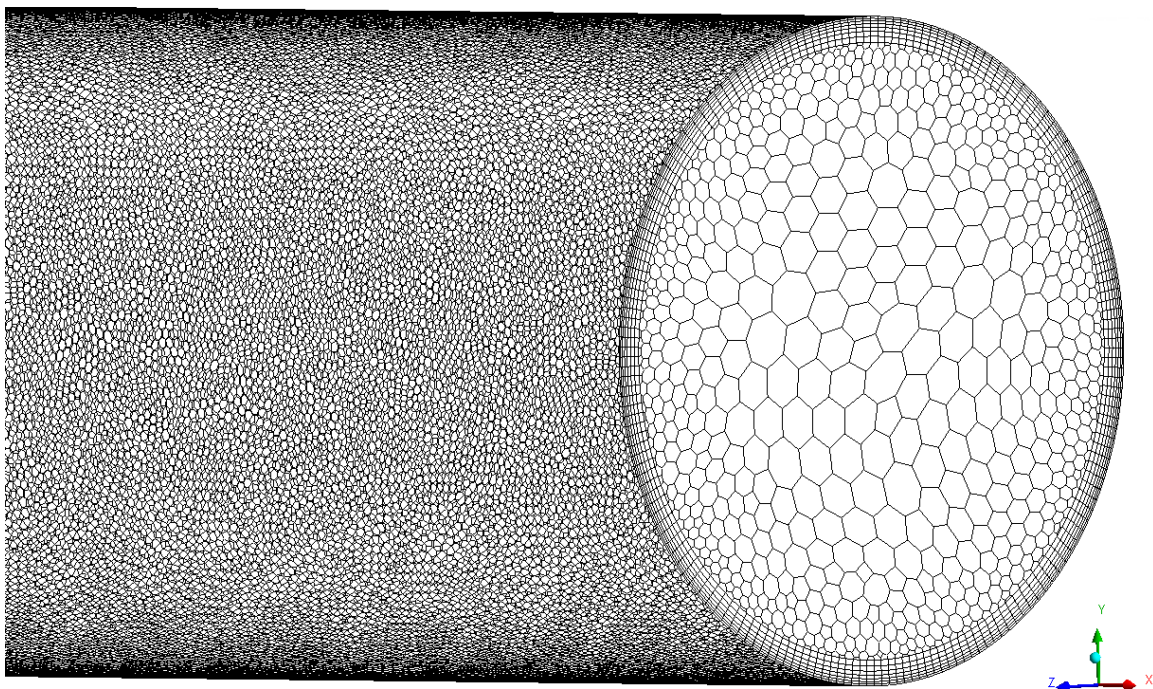


Figure 5.7 Detail view of polyhedral mesh quality.

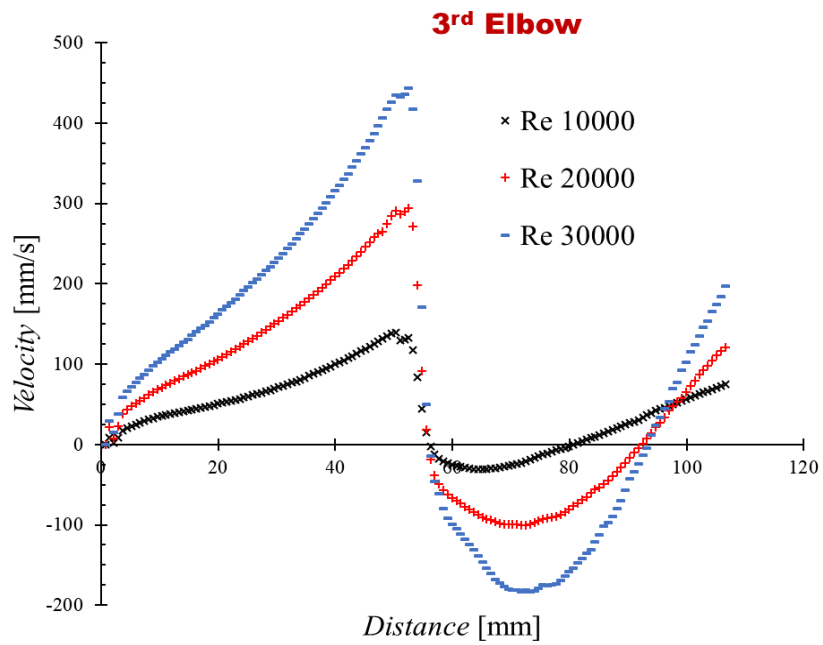


Figure 5.8 1D velocity profile in third elbow for different Reynolds number.

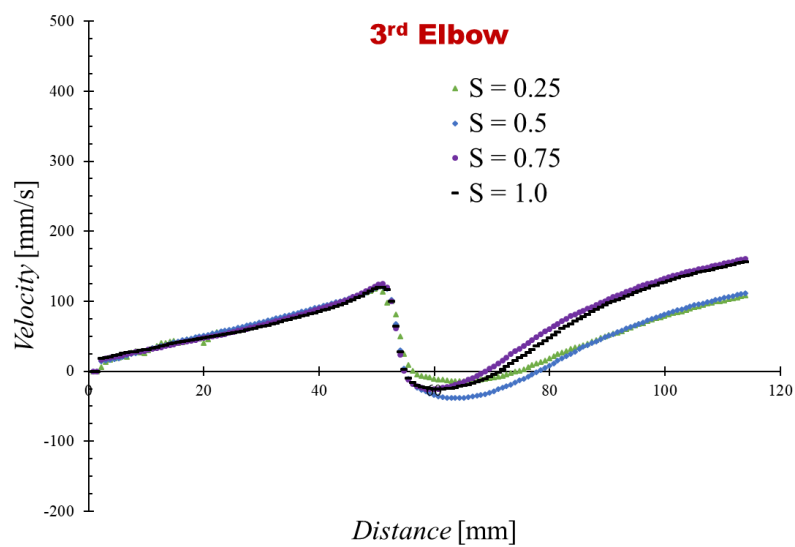


Figure 5.9 1D velocity profile in third elbow for different swirl number.

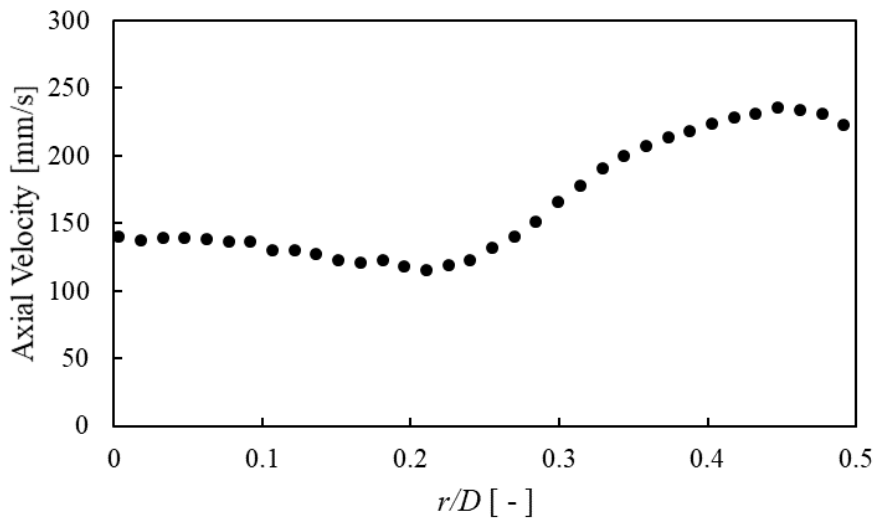


Figure 5.10 Inlet swirling flow condition with axial velocity.

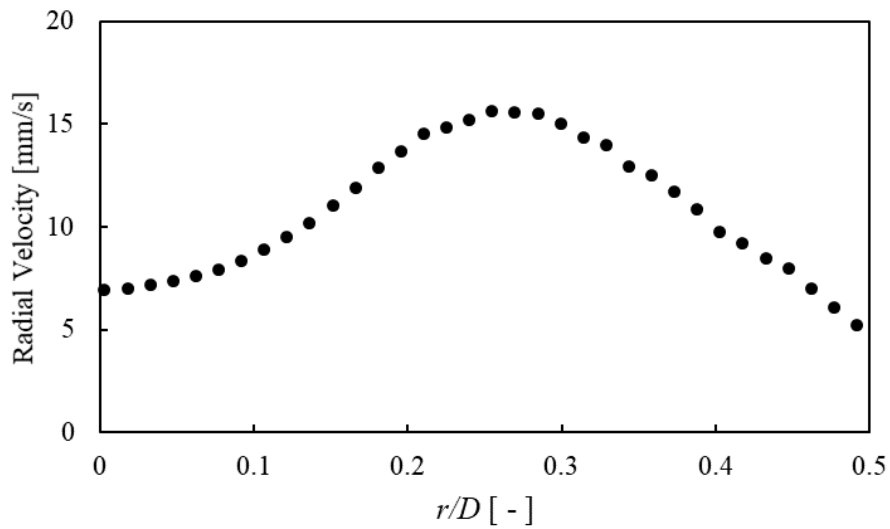


Figure 5.11 Inlet swirling flow condition with radial velocity.

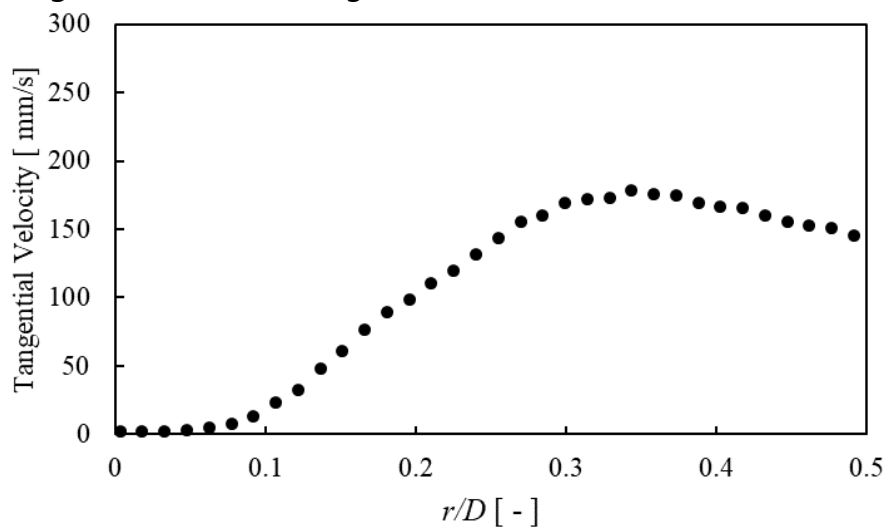


Figure 5.12 Inlet swirling flow condition with tangential velocity.

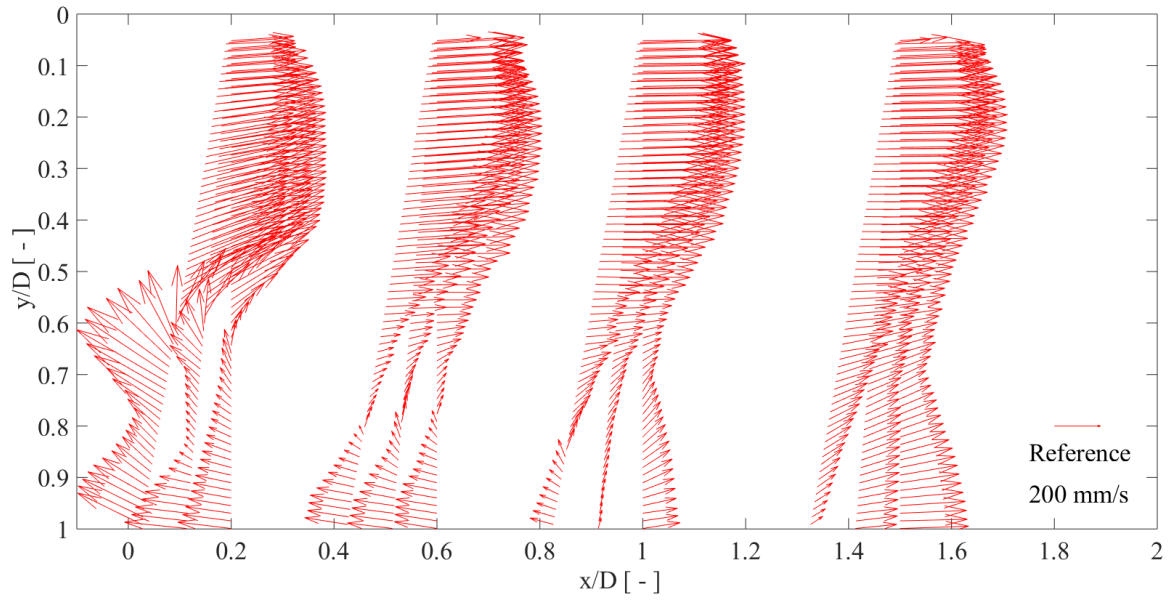


Figure 5.13 Two-dimensional time average axial velocity from experiment.

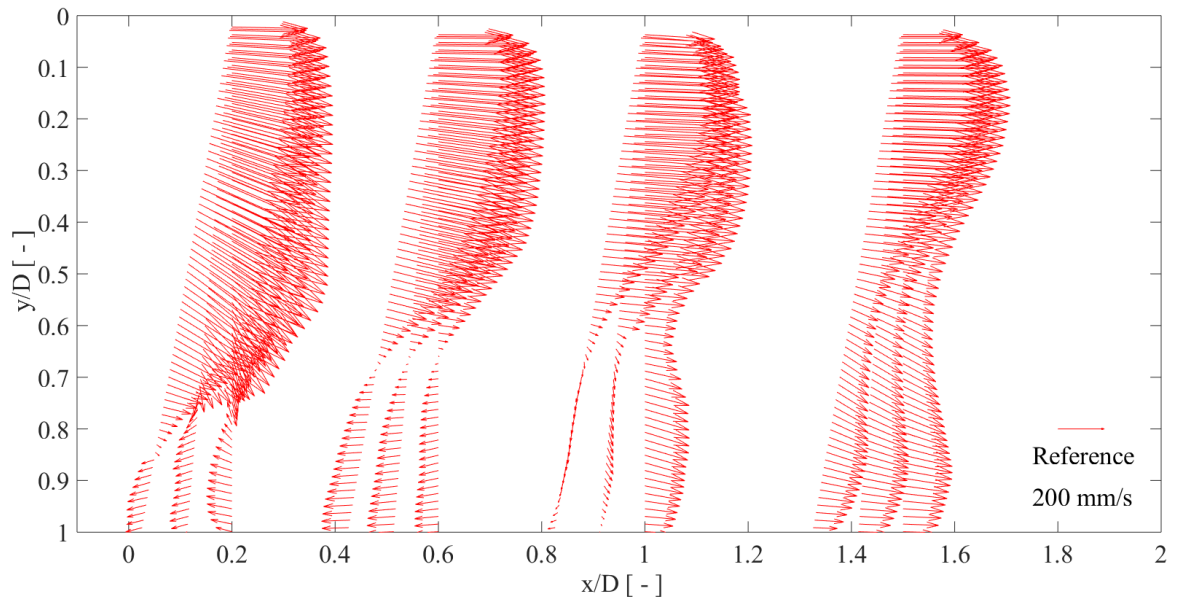


Figure 5.14 Two-dimensional time average axial velocity from simulation.

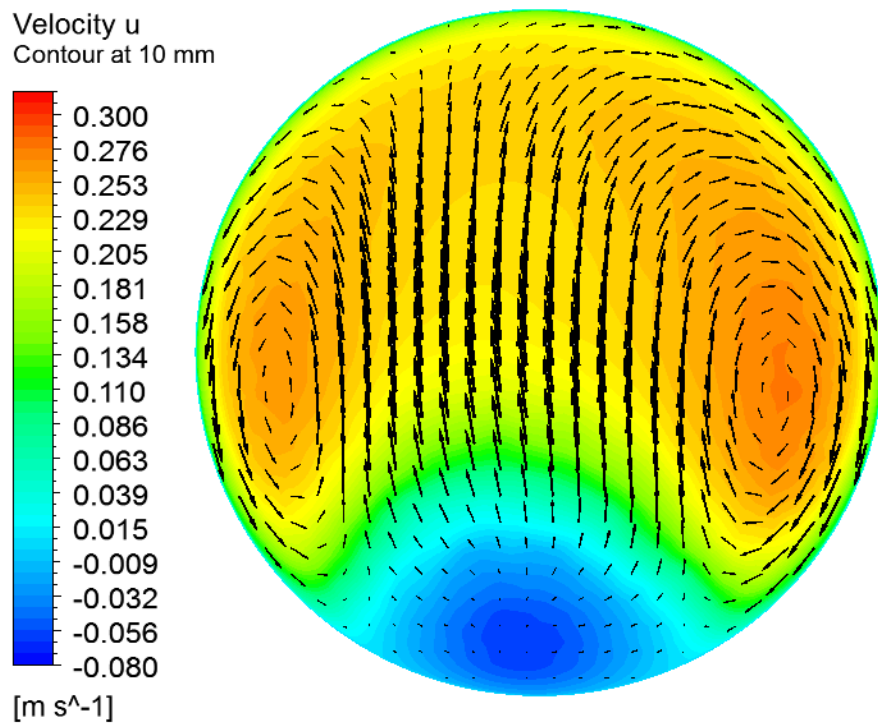


Figure 5.15 Cross sectional velocity distribution for 10 mm position.

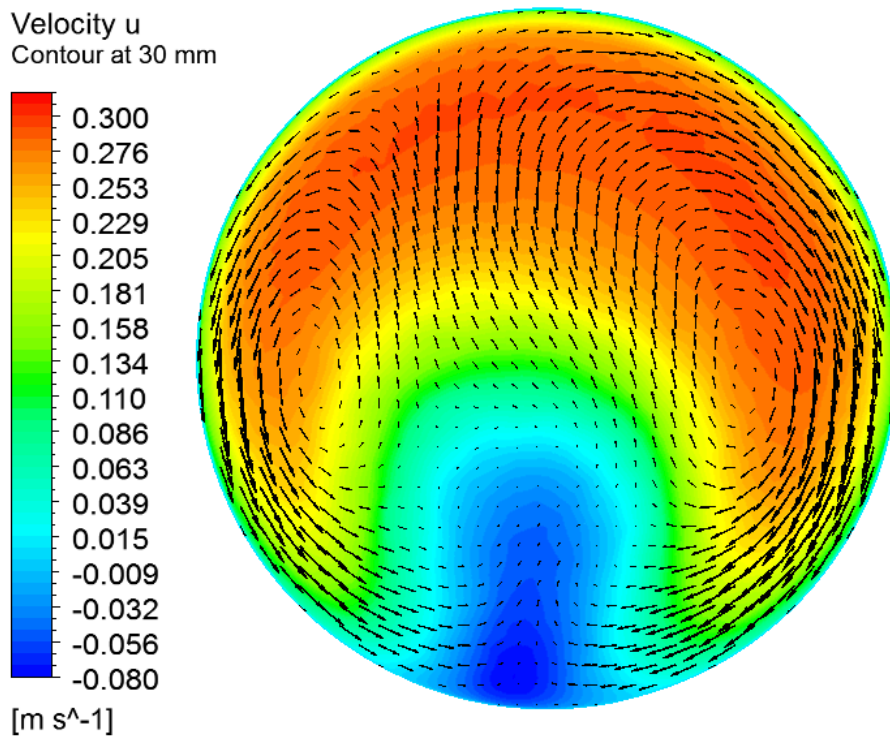


Figure 5.16 Cross sectional velocity distribution for 30mm position.

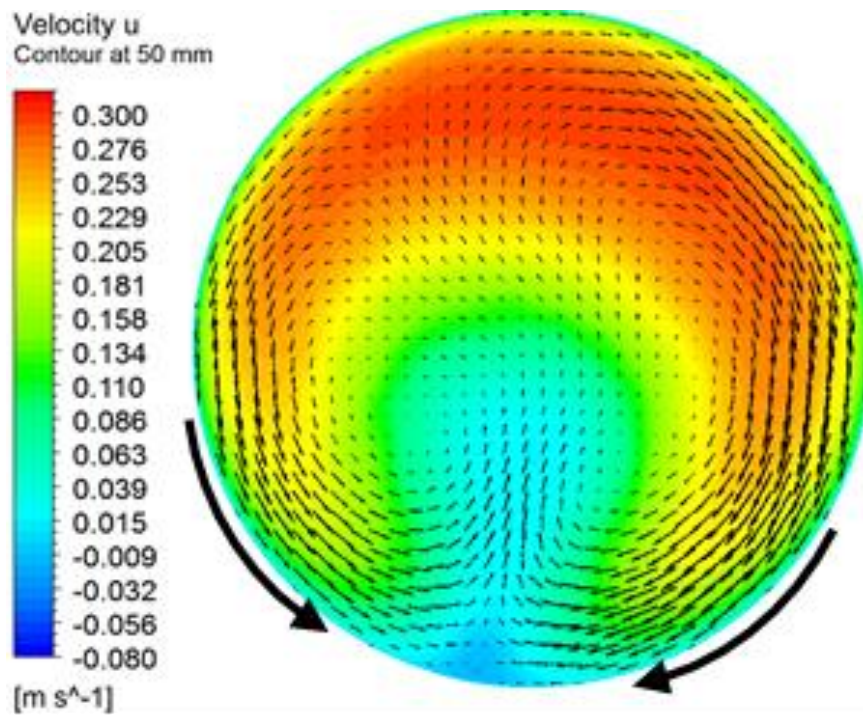


Figure 5.17 Cross sectional velocity distribution for 50mm position.

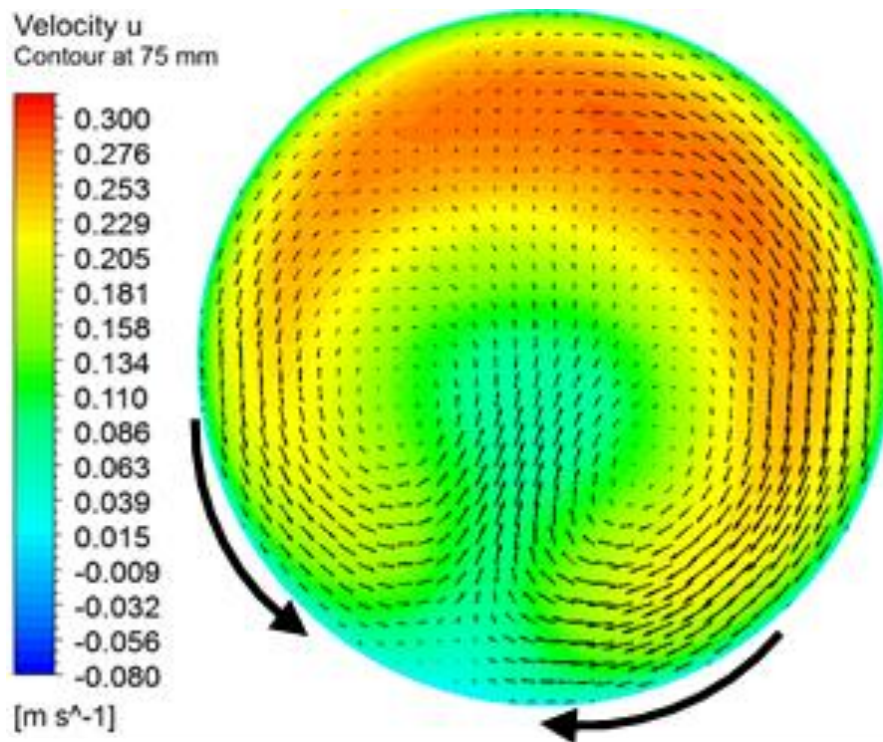


Figure 5.18 Cross sectional velocity distribution for 75 mm position.

Chapter 6

Conclusions

In this study, Velocity Profiler (UVP), Phased Array UVP and PIV systems are used to measure the velocity profiles and to visualize flow structure downstream of a compact pipe layout, which make with a single elbow, the double elbows and the triple elbows. In addition, The velocity profiles from the measurement at upstream of the compact pipe layout were imposed in CFD numerical simulation to visualize the complete flow structure through that compact pipe. The observations from the experiment and numerical simulation are concluded as follow;

In Chapter 2 – The fluid flow structure and turbulent kinematic energy are analyzed base on the different Reynolds number downstream of a single elbow. From this investigation, the axial and tangential flow structure downstream of a single elbow does not change even we used different Reynolds number. The fluid velocity field and turbulent kinetic energy were shown as contour plots. The turbulent kinetic energy is increasing in the low velocity region just downstream of the inner elbow wall (intrados). The high velocity occurs at the outer wall of the elbow end (extrados). From this investigation, the appropriate Reynolds number ($Re = 10,000$) is appropriate to use the turbulent flow measurement and inlet swirling flow measurement.

In Chapter 3 - The measurement of the two-dimensional velocity vector is carried out by Phased Array UVP system and PIV. The flow distortion and secondary reverse flow occur in the measurement region downstream of the double bend pipe. From both measurement results, the secondary flow starts from the edge of inner elbow and ends at the reattachment point around $x/D = 1$. In the velocity fluctuation analysis, the axial velocity fluctuation apparently occurs at the boundary of the main flow and the secondary flow. The radial velocity fluctuation occurs at the center of the pipe.

In Chapter 4 – Phased Array UVP system was applied for two-dimensional velocity measurements in the condition of without inlet swirling flow and with inlet swirling flow on the double bend pipe flow. According to one-dimensional velocity profiles, the velocity magnitude of inlet swirling flow is much stronger than without inlet swirling flow in the secondary flow region. These differences are due to the

influence of the inlet swirling flow. In two-dimensional velocity of without inlet swirling flow, the flow separation occurs around $x/D = 0.1$, and the reattachment point is located at $x/D = 1.5$. In case of inlet swirling flow, the flow separation phenomenon is same as the condition of without inlet swirling flow, but the reattachment point is located at $x/D = 1$. Therefore, the reverse flow region is narrow. In one-dimensional velocity measurement, we can confirm that the influence of swirl number on the movement of reattachment point. However, the effect of Reynolds number is very weak on the movement of reattachment point. At $x/D = 1.5$, the fluid becomes the accelerated swirling flow. In the condition of without inlet swirling flow, the axial velocity fluctuation is higher than with inlet swirling flow, but tangential velocity fluctuation is lower than inlet swirling flow.

In Chapter 5 – The combination of experimental investigation and numerical simulation were done to observe the flow structure and velocity distribution at the inlet swirling flow condition. Phased Array UVP system can visualize two-dimensional velocity field and can confirm the flow separation and reattachment point. The flow separation occurs around the edge the sharp elbow and the reattachment point is located near $x/D = 1$. In third elbow, reverse flow region is narrow on Re 10,000 because pipe layout is vertical and the length between second and third are longer than between first and second elbow. Reattachment point for Re 20,000 and 30,000 occurs almost at the same position. Swirl number effect is still obviously influence on the changes of reattachment point. The numerical simulation result show that the swirling flow structure is quite similar with the experimental result. Therefore, the validation of the CFD simulation is acceptable. In case of cross-sectional plane visualization, two counter rotation vortex cells were observed at $x/D = 0.2$ and $x/D = 0.6$ positions. Then, the flow pattern is slightly changes as circumferential flow at $x/D = 1$ and $x/D = 1.5$. When the high velocity axial flow reached the outside wall, this flow was changed from outside to lateral side of pipe wall in clockwise and counterclockwise directions. In addition, the axial velocity distribution is too different between the intrados and extrados of pipe.

Finally, I would like to make general conclusion for this study. Phased Array UVP system was successfully applied to visualize two-dimensional flow structure at the downstream of the compact pipe layout in the condition of turbulent flow at Reynolds number 10,000 and inlet swirling flow condition. The aim is to improve the performance of the measurement system and to apply in the flow measurement and flow visualization system in the power plant. The characteristic of complex flow structure and velocity fluctuation were analyzed from the experimental results. The combination of experimental results and numerical simulation visualized the fully flow structure in the cross-sectional plane and the axial plane. This study supports to understand clearly the flow characteristics of water flow for the compact pipe layout in the turbulent flow condition.

List of Publications

I. Journal Articles

- (1) San Shwin, Ari Hamdani, Hideharu Takahashi, and Hiroshige Kikura, Experimental Investigation of Two-Dimensional Velocity on the 90° Double Bend Pipe Flow Using Ultrasound Technique. *World Journal of Mechanics*, 7(12), (2017), 340 – 359.
- (2) San Shwin, Ari Hamdani, Hideharu Takahashi, and Hiroshige Kikura, Two-dimensional Velocity Measurement Downstream of the Double Bend Pipe Using Phased Array Ultrasonic Velocity Profiler. *Advanced Experimental Mechanics*, Vol.3, (2018), 111 – 117.
- (3) San Shwin, Ari Hamdani, Hideharu Takahashi, Nobuyuki Fujisawa and Hiroshige Kikura, Experimental and Numerical Investigation of Swirling Flow on Triple Elbows Pipe Layout. *Journal of Flow Control, Measurement & Visualization*, (Submitted).

II. International Conferences

- (1) San Shwin, Ari Hamdani, Hideharu Takahashi, and Hiroshige Kikura, Velocity Profile Measurement of Swirling Turbulent Flow Downstream of the Double Bend Pipe. *12th International Symposium on Advanced Science and Technology in Experimental Mechanics (ISEM 12th)*, 1-4 November, 2017, Kanazawa, Japan. A087 30.
- (2) Hideharu Takahashi, San Shwin, Ari Hamdani, and Hiroshige Kikura, Velocity Profile Measurement of Swirling Turbulent Flow Downstream of the Double Bend Pipe. *The 28th International Symposium on Transport Phenomena, (ISTP 28th)*, 22-24 September 2017, Peradeniya, Sri Lanka. ISTP007 315 - 319

III. Japanese Conferences

- (1) San Shwin, Ari Hamdani, Hideharu Takahashi, and Hiroshige Kikura, Velocity Profile Measurement of Swirling Turbulent Flow Downstream of the Double Bend Pipe, *Visualization Symposium, 18-19 July 2017*, Kogakuin University, Tokyo Japan. VS405 115-119.
- (2) San Shwin, Ari Hamdani, Hideharu Takahashi, and Hiroshige Kikura, Flow Visualization on Downstream of the Double Bent Pipe by Phased Array Ultrasonic Velocity Profile Method, *AESJ Young Researcher Forum, 2 Nov 2016*, Tokyo Institute of Technology, Tokyo. A-13.
- (3) San Shwin, Ari Hamdani, Hideharu Takahashi, and Hiroshige Kikura, Study on Turbulent Flow Downstream of the Double Bent Pipe with Twisted Tape Insert, *AESJ Student Poster Session, 28 March 2017*, Tokai University, Tokyo.

Acknowledgements

First of all, I would like to thank **Prof. Hiroshige Kikura**, for giving me the opportunity to study in his laboratory and for supervising this dissertation. This is the turning point of my life. He give me the special offer to become smooth in the future life. He teach me not only about science and technology but also about life.

I would like to appreciate my defense committee members, **Prof. Yukitaka Kato**, **Prof. Hiroshi Akatsuka**, **Prof. Hiroaki Tsutsui** and **Prof. Hiroshi Sagara** for their insightful questions and useful comments. I thank **Assistant Prof. Hideharu Takahashi**, for the help in the discussions, preparations. He always take care me not only for research but also in social events.

Also, **Prof. Dr Phoe Kaung** (Rector from University of Yangon), **Dr. Khin Mar Kyu** (Head Prof. in Department of Physics) and **Prof. Dr. Aye Aye Thant** give me a chance to study for Doctoral program. I am glad about their forwardness.

Special thanks to **Dr. Ari Hamdani**, for fruitful discussions and guidance during the study in our laboratory. He is my special teacher in my student life in Tokyo Tech.

I would like to thank to **Prof. Nobuyuki Fujisawa** in Niigata University for his advice on the design of swirling generator.

I would like to thank the present and former students in Kikura Laboratory for providing helps and assistances during my 3 years study, especially Antonin Povolny, Ryan Nado Paratama, Rendy Silva Renata, Tran Tri Vien, Wongsakorn Wongsaroj, Jevin Tanius Owen, Rendy Silva Renata. I would like to thank to my special friend Batsaikhan Monkbat.

The financial support by **Japan International Co-operative Agency (JICA)** is gratefully acknowledged.

Finally, I would like to thank **Mr.Tsuruoka-san** because he save my life by making some experimental setup. I never forget his supports.